HIGHWAY RESEARCH RECORD

Number 354

Bridges and Bridge Foundations

9 Reports

Subject Areas

27 Bridge Design
33 Construction
63 Mechanics (Earth Mass)

HIGHWAY RESEARCH BOARD
DIVISION OF ENGINEERING NATIONAL RESEARCH COUNCIL
NATIONAL ACADEMY OF SCIENCES—NATIONAL ACADEMY OF ENGINEERING
Washington, D.C. 1971

ISBN 0-309-01967-2

Price: $3.00

Available from

Highway Research Board
National Academy of Sciences
2101 Constitution Avenue
Washington, D.C. 20418

SPONSORSHIP OF THIS RECORD

GROUP 2—DESIGN AND CONSTRUCTION OF TRANSPORTATION FACILITIES
John L. Beaton, California Division of Highways, chairman

Committee on Steel Superstructures
Gerard F. Fox, Howard, Needles, Tammen and Bergendoff, chairman
B. R. Davis, Henry W. Derthick, Arthur L. Elliott, John W. Fisher (secretary), Richard S. Fountain, Carl H. Gronquist, Theodore R. Higgins, William H. Munse, Frank Sears, A. A. Toprac, Ivan M. Viest

Committee on Concrete Superstructures
Henry W. Derthick, Tennessee Department of Highways, chairman
W. E. Baumann, Russell L. Chapman, Jr., Hotten A. Elleby, Norris L. Hickerson, C. L. Hulsbos, Daniel P. Jenny, Alan H. Mattock, James L. Norris, Robert A. Norton, Paul F. Rice, Dominick L. Somma, David A. Van Horn, Harry N. Wenke (secretary), Earle E. Wilkinson

Committee on Dynamics and Field Testing of Bridges
Robert F. Varney, Federal Highway Administration, chairman
James W. Baldwin, Jr., Edwin G. Burdette, Michael E. Fiore, Charles F. Galambos (secretary), Egbert R. Hardesty, Conrad P. Heins, Jr., C. L. Hulsbos, Henry L. Kinnier, K. H. Lenzen, William H. Munse, LeRoy T. Oehler, W. W. Sanders, Jr., C. P. Siess, W. H. Walker, Robert K. L. Wen, George W. Zuurbier

Committee on Construction of Bridges and Structures
Carl E. Klamm, Missouri State Highway Commission, chairman
Randle B. Alexander, W. E. Crum, Richard M. Dowalter, Dale F. Downing, Albert L. Grubb, George A. Harper, Wayne Henneberger, Marvin H. Hilton, John F. McGovern, James Calvin McGrew, G. I. Sawyer, Philo H. Schultz, Kenneth R. Scurr, Samuel B. Usry, H. R. J. Walsh, Harry N. Wenke

Committee on Foundation of Bridges and Other Structures
Melvin T. Davisson, University of Illinois, Urbana, chairman
David R. Antes, Edwin C. Beethoven, Bernard E. Butler, Harry M. Coyle, Jacob Feld, David S. Gedney, Robert J. Hallawell, Horace E. Hoy, Martin S. Kapp, Philip Keene, Richard E. Landau, Clyde N. Laughter, G. A. Leonards, Thomas D. Moreland, Alex Rutka

L. F. Spaine and J. W. Guinnee, Highway Research Board staff

The sponsoring committee is identified by a footnote on the first page of each report.

FOREWORD

Of the 9 papers contained in this RECORD, 5 papers are concerned with the dynamic reaction or performance of structures or portions of structures under actual service conditions. Those interested in instrumentation of existing structures may find these helpful. Three papers deal with pile capacities, and one paper discusses curved plate girders.

Galambos and Heins instrumented a rural highway bridge in Maryland. They recorded the vehicle passages, loading characteristics, and stress experience the structure endures. Techniques of interpreting the data are discussed as well as efforts to estimate the fatigue life of the structure from the data obtained. They concluded that the main stress-carrying members of a structure are not likely to be susceptible to fatigue distress.

McKeel and Kinnier confined their interest to a dynamic stress study of steel rockers as contrasted to elastomeric pads. Contrary to some expectations, the elastomeric pads did not noticeably reduce the vibration of the spans, neither did they reduce the flexural stresses. In fact, there seemed to be a trend toward somewhat increased deflections with the elastomeric pads at all speeds of the test vehicle.

The control of bridge vibrations also was the concern of Derby and Calcaterra as they measured the dynamic response of bridges to the passage of heavy loads. They considered 4 different bridge designs and then directed their study toward methods of controlling the vibration. They compared the cost effectiveness as well as the dynamic response of each of the control methods.

The dynamic properties of suspension bridges were studied by McLamore, Stubbs, and Hart. The experimental determination of the vibrational characteristics of 2 different suspension bridges was recorded. The similarities in occurrence of higher order modal frequencies were compared to the lowest modal frequencies. The authors hoped to develop some rules of thumb that will be helpful during the design of suspension bridges.

A study of the static and fatigue behavior of composite beams containing a 2-in. square precast, prestressed tension element was made by Mirza, Zia, and Bhargava. This was a novel use of prestressing in that the tendon was encased in these square rods of concrete and then set into the forms more or less like conventional reinforcing steel. Results revealed that the use of these tension elements for continuity connections creates a superior section materially increasing the cracking load and providing better protection of the reinforcement against corrosion.

Culver studied the different effects of various flange width-thickness ratios for both A-36 and A-441 steel girders. The results indicate that the factor of safety against local buckling using the developed criteria for curved girders, fabricated by welding or by heat-curving with web-thickness ratios equal to or less than current AASHO requirements, is about the same as that for straight girders. It was also found that the factor of safety decreases as the ratio of warping to bending normal stress increases.

The perennial subject of accurate pile load capability has a dynamic approach in the paper by Gnirk, Krause, Bump, and Anderson. Dynamic response of the pile is recorded during the driving process and then correlated with static load tests. In 8 cases the quantitative agreement was quite good. Consideration is also given to simulating the hammer-pile-soil system on an analog computer.

Clisby and Mattox compared laboratory and field tests of load carrying capacity tests on single- and multiple-underreamed bored piles. Bell spacing and failure planes in the soil were studied. It was determined that multiple belling of cast-in-place piles can result in economical designs for many soil conditions.

The effect of subsurface lateral loads on piles was measured and described by Nicu, Antes, and Kessler. The instrumentation of a pile-supported abutment over soft compressible soil is described. The findings permit the tentative establishment of limiting values for stresses imposed on compressible layers under conventionally designed abutments and suggest remedial measures against backward tilting.

—Arthur L. Elliott

CONTENTS

LOADING HISTORY OF HIGHWAY BRIDGES: COMPARISON OF STRESS-RANGE HISTOGRAMS

C. F. Galambos, Federal Highway Administration; and
C. P. Heins, Jr., University of Maryland

This report presents the results of a loading history field test on a rural highway bridge in Maryland. Two ways of data reduction are compared: One technique notes only one stress event per truck passage, while the other technique produces several events for each vehicle. The composition and weight of the truck traffic are presented, along with a number of occurrences of multiple crossings. Several methods of estimating the fatigue life of the bridge are also attempted. Some conclusions from the study are that significant differences in the shape of stress-range histograms can result, depending on the inclusion or exclusion of the several secondary stress ranges, but that for stress ranges above 3.0 ksi no significant differences in the histograms are found. Higher average stress ranges were produced by multiple crossings than by single crossings. It was also concluded that the main load-carrying members of this bridge are not likely to suffer from traffic-induced fatigue distress.

•DURING the past several years, there has been under way an extensive program of field tests on highway bridges to determine the loading history of the main load-carrying members. The program is promoted on a national scale by the Federal Highway Administration and is guided by committees of the American Society of Civil Engineers and the Highway Research Board.

The actual field testing and data gathering are being done by various agencies and, therefore, some differences naturally result in the final data presentation. The main end product of each study is usually a series of stress-range histograms, where the magnitude of the stress range is plotted as the abscissa and the percentile of the total number of stress ranges is plotted as the ordinate. There can be a sizable variation in percentages based on the same number of truck passages, depending on how many vibrations caused by a single truck are recorded.

Because it is desirable to draw some common conclusions from all these tests and because the field test results are being adapted to laboratory fatigue tests, it is important that there be some standardization of recording, data reduction, and presentation.

It is the purpose of this report to describe the differences that may occur in the shape of a stress-range histogram and the importance of these differences. A suggestion for a common approach to the presentation of the data is then given. It is also intended to explore several methods for relating the field test results to an estimation of the fatigue life of the structure.

The comparison of results is based on a cooperative field test made in Maryland in July 1969. A crew from the Civil Engineering Department of the University of Maryland prepared the bridge site for testing and attached the strain gages. Separate, but simultaneous, data recording was made from 8 sets of 2 gages placed adjacent to each other by the University of Maryland crew and by a crew from the Structures and Applied Mechanics Division of the Federal Highway Administration.

Sponsored by Committee on Dynamics and Field Testing of Bridges and presented at the 50th Annual Meeting.

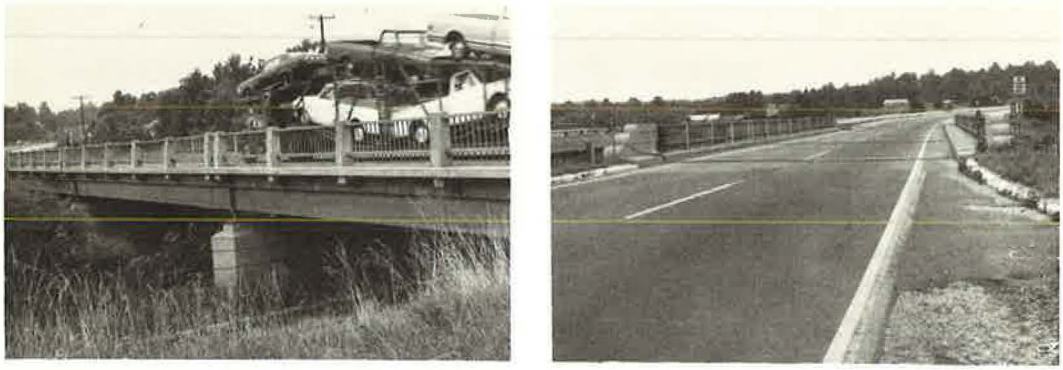

Figure 1. Bridge on US-301 southbound.

THE BRIDGE

The bridge is a 3-span continuous structure, built in 1949, and is located on US-301 near Md-4. The structure is built of steel WF sections with a 7-in. thick concrete deck and carries the southbound traffic across a small stream. Figures 1 and 2 show several views and details of the bridge.

Eight sets of strain gages were placed on 3 of the 7 girders at 3 cross sections, as shown in Figure 3. Most of the comparisons in this report will be based on readings obtained from gage position B1, which is on the second interior girder on the right side looking south and is at the middle of the first span. A more exact description of gage locations is given in another report (1).

The 2 gages at each location were oriented in the longitudinal direction on the bottom flange and were placed side by side as close to each other as physically possible. One gage served the Maryland recording equipment, and the other served the FHWA equipment. There should be no difference in strain readings of gages at each gage site.

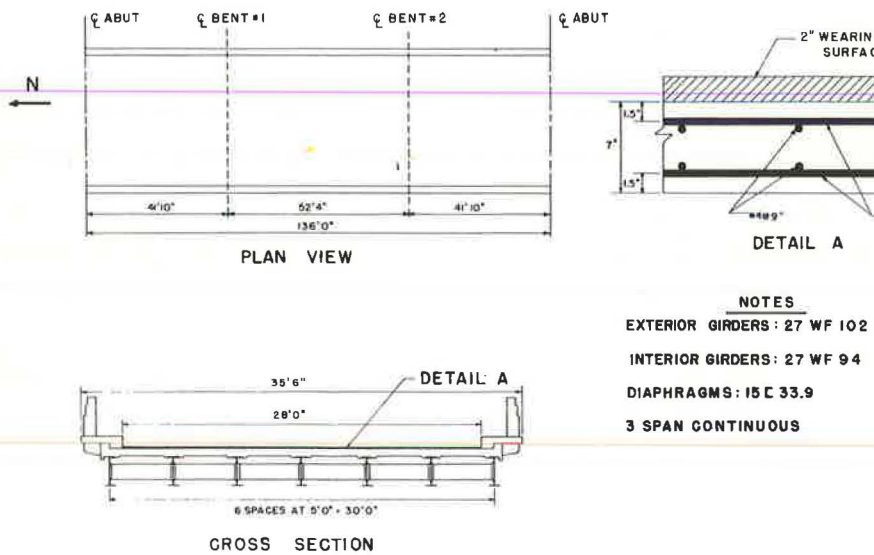

Figure 2. Structural details of bridge.

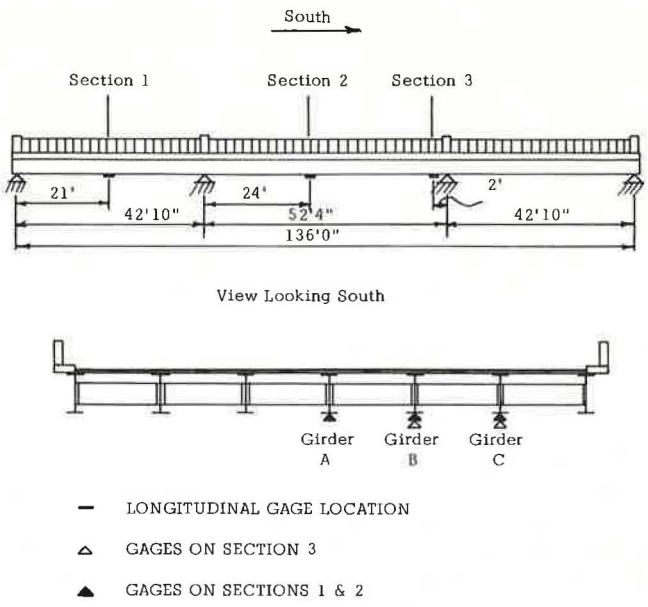

Figure 3. Strain gage locations.

The design stresses for a point corresponding to gage position B1 were as follows:

Load	ksi
Dead	5.9
Live, with impact	12.1

These calculated stresses were based on the 1944 AASHO Bridge Specifications.

DATA ACQUISITION AND REDUCTION

University of Maryland

When a truck crossed the structure, a strain trace from gage B1 resulted in a typical response curve as shown in Figure 4. A trace produced by a 3-axle dump truck is shown somewhat idealized on this figure. Other axle configurations produced slightly different response records.

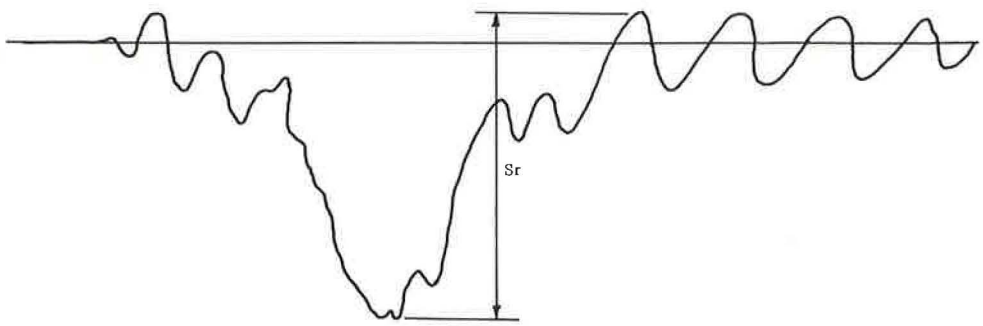

Figure 4. Typical strain trace caused by a 3-axle dump truck.

The instrumentation used by the university recorded such traces from each gage on oscillograph paper for the passage of 1,275 trucks. The principal data reduction for this test consisted of obtaining the maximum stress range only for each record. The maximum stress range, Sr, is shown in Figure 4. Notes were made during testing so that each record could be related to a specific truck. Occasionally it happened that 2 or more trucks were on the bridge simultaneously, producing, however, only 1 record.

The dynamic field data were obtained with a Brush light-beam oscillograph and two 4-channel carrier amplifiers. A time line generator and event marker system permitted evaluation of the axle spacings and vehicle speeds.

The dynamic records were edited and read on a Gerber digital-data reduction system. The system translated selected points on the record to digital output that was punched on cards.

The data from the vehicle classification notes were also punched on cards. Several computer programs were subsequently used to further process the data and produce the desired output of strains and vehicle types.

Federal Highway Administration

The data-acquisition system used by FHWA is an automated computer controlled system, which takes the output from strain gages in the form of analog voltages, digitizes these voltages, and stores and tabulates strain ranges for specified periods of time. This equipment is described further in another report (2). There is no record of a visual strain trace; neither is it possible to relate individual strain ranges to specified trucks.

The usual period of recording was 1 hour. Four minutes of each hour were used for typing the results. No strains were recorded during the typing period. Exact correlation of data between the 2 recording systems for selected hours was possible by marking on the Maryland notes the exact time that sampling began and ended on the FHWA system. Strains were sampled for 63 hours by the FHWA system, during all hours of some days.

The definition of what is recorded as a stress range in the FHWA system is shown in Figure 5. The dashed line represents a level of strain below which no recordings are made. This is done to eliminate the counting of the many small vibrations caused by cars. This level was set at 5 microinches per inch of strain in the subject test.

Figure 5 shows that, in addition to the major stress range, several other stress ranges are recorded, as long as the trace goes beyond the dashed line and returns to the zero level. Thus, it is possible for 1 truck to produce a number of stress ranges at a point in a bridge. In fact, some of the secondary stress ranges due to 1 truck may be larger than the maximum stress range caused by another truck.

Traffic Description

The traffic across the bridge is rural high-speed traffic in a nearly flat or gently rolling terrain. The speed limit is 55 mph. No vehicle speed measurements were made in this study.

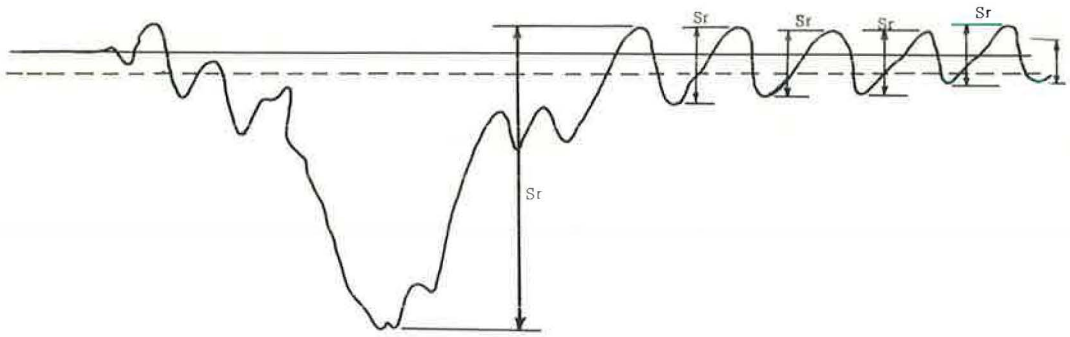

Figure 5. Definition of stress ranges recorded by the FHWA equipment.

The average daily traffic was 10,500 vehicles, with 17 percent trucks, based on the 1968 traffic count. The makeup of the truck traffic is described elsewhere in this report.

COMPARISON OF FIELD DATA

Stress-Range Histograms

The following comparisons are based on the data obtained from 7 selected hours of sampling. Both the Maryland data and the FHWA data were caused by the same 350 trucks. Those trucks missed by the FHWA system during typing periods were excluded from the Maryland data. Therefore, any apparent differences are due to the difference in the number of stress ranges only.

The 2 stress histograms resulting from the 350 trucks are shown in Figure 6. There is a marked difference in the 2 sets of data; the FHWA data show a very large percentage of small values (600 psi). The stress ranges always originate from zero. For example, the bars from 2.4 to 3.0 ksi represent a stress range from zero to somewhere between 2.4 and 3.0 ksi.

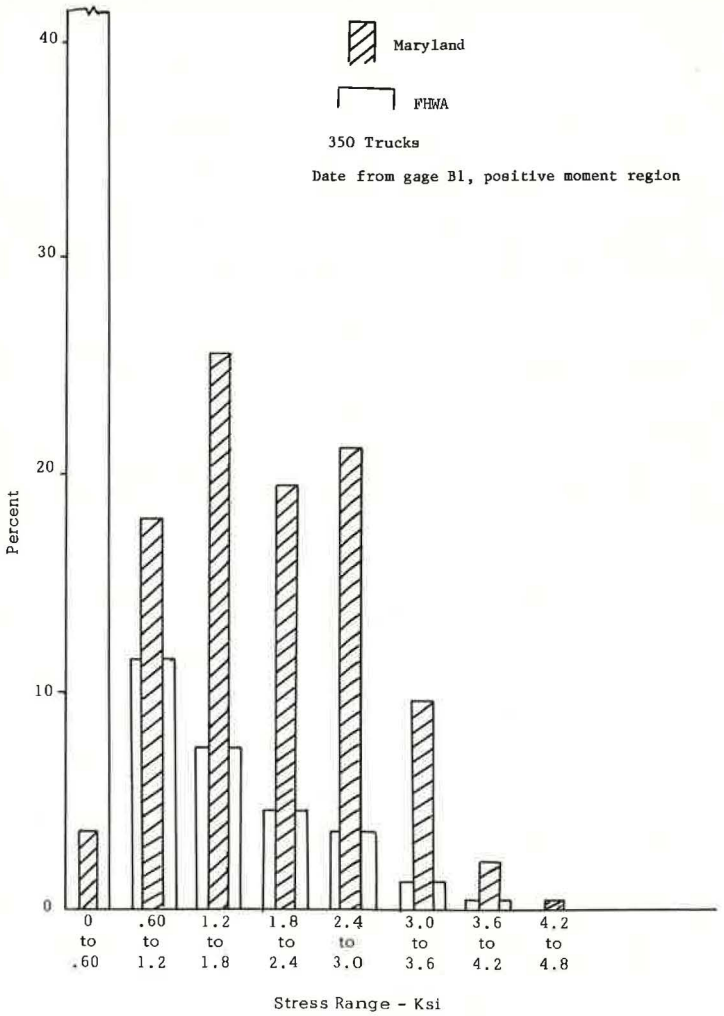

Figure 6. Comparison of stress-range histograms.

The actual numbers of stress ranges for the 2 sets of data are given in Table 1. It is seen in this table that, but for one exception, the FHWA column shows a greater number of stress ranges in each level. Only 334 stress ranges in the Maryland data result from the 350 trucks because there were several multiple crossings that produced only one record.

TABLE 1

COMPARISON OF STRESS RANGES RECORDED DURING 7 SELECTED HOURS

Stress Range (ksi)	Number of Occurrences	
	Maryland	FHWA
4.8		
4.2	1	
3.6	7	8
3.0	32	28
2.4	71	80
1.8	65	100
1.2	86	163
0.6	60	251
0	12	1,605
Total	334	2,235

Truck Traffic Composition

The composition of the truck traffic during the 7 selected hours is shown in Figure 7 for each of the hours, as well as for the total 7 hours.

No trucks were weighed during this test, but, during the previous year in July 1968, all trucks in the adjacent northbound lane were weighed during a 7-day period (3). There is no reason to believe that northbound traffic is different from southbound traffic, nor is it probable that the mean gross weight of the trucks has changed in one year. There-

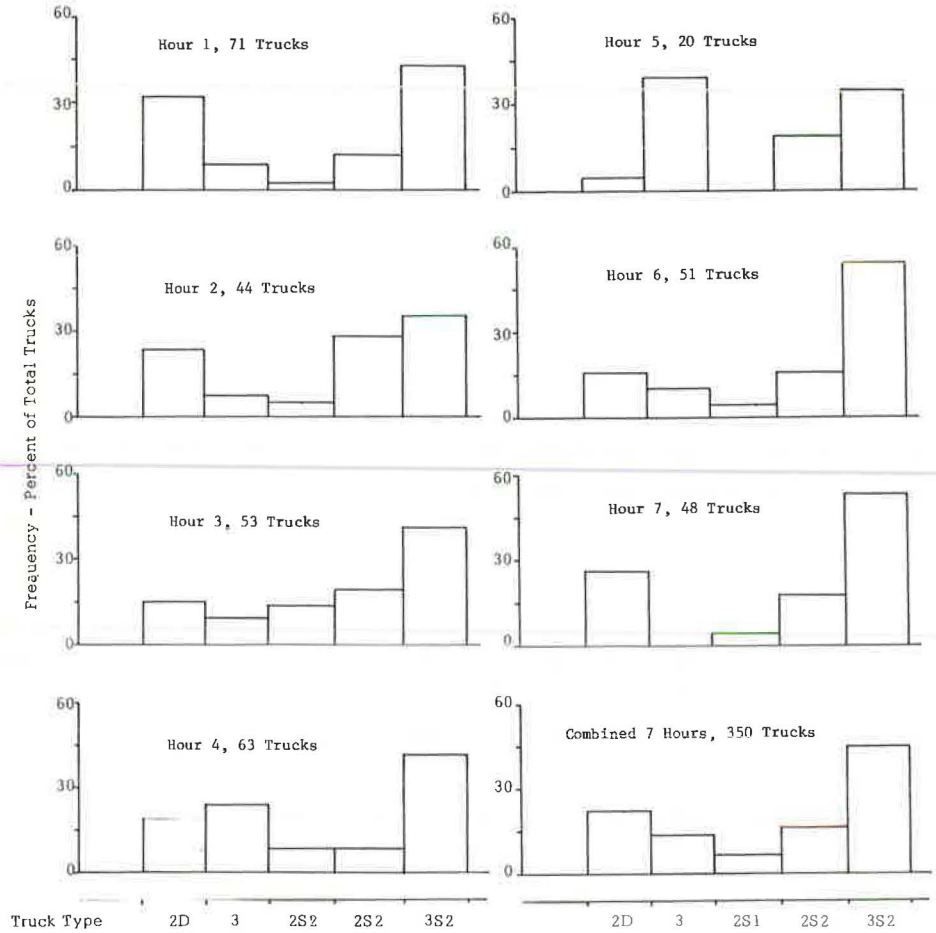

Figure 7. Distribution of truck types for each of the 7 selected hours.

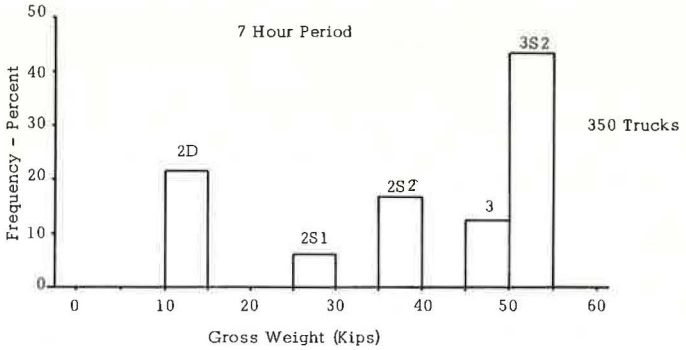

Figure 8. Frequency of mean gross weight of trucks for 7 selected hours.

fore, it will be assumed in this report that the mean gross weights of the 5 truck types are as follows:

Truck Type	Gross Weight (kips)
2D	10 to 15
3	45 to 50
2S1	25 to 30
2S2	35 to 40
3S2	50 to 55

For the 7-hour comparison, the frequency of assumed mean gross weight per truck type is as shown in Figure 8.

Stresses Above 3 ksi

It can be argued, based on past laboratory fatigue tests, that stress ranges below the fatigue limit of the material have no effect on the life expectancy of the structure and can, therefore, be ignored. However, recent tests at Lehigh University (4) on the fatigue of weldments tend to show that there may not be a material fatigue limit. There is, however, a practical fatigue limit in that it would take almost forever for small stresses to cause detectable damage.

What are "small" stresses? If all the stress ranges below 3.0 ksi are dropped from both columns in Table 1, very few numbers remain, and it becomes difficult to make statistically meaningful comparisons of the data. Even so, by using the t-test, it was shown that at the 95 percent confidence level there is no significant difference in the means of the 2 sets of data above 3.0 ksi.

A more meaningful comparison of the 2 sets of data can be made if all values above 3.0 ksi are compared for the entire test period as given in Table 2. The Maryland data were recorded during the daytime hours, while the FHWA data include some nighttime traffic. The previously selected 7-hour data (Table 1) are included with data given in Table 2. The Maryland data were collected during passage of 1,275 trucks, for 27 random hours during 4 consecutive days, and the FHWA data were collected in 61 hours and involve an estimated 2,500 trucks.

TABLE 2
STRESS RANGES ABOVE 3.0 ksi

Stress Range (ksi)	Number of Occurrences	
	Maryland	FHWA
6.0		
5.4	1	2
4.8	1	3
4.2	7	10
3.6	36	51
3.0	107	230
Total	152	296

No significant difference between the means of the 2 sets of numbers given in Table 2 was found at the 95 percent confidence level. The stress-range histograms, shown in Figure 9, will result when these numbers are converted to percentages. This figure represents the best estimate of the stress ranges above 3.0 ksi to which this bridge is subjected at the maximum positive moment section in the end spans during present-day traffic. The corresponding truck traffic distribution with the assumed mean gross weights are as shown in Figure 10.

Multiple Crossings

The bridge under investigation is a 2-lane structure and, therefore, occasionally 2 or more trucks may cross the bridge at the same time. It is also possible to have more than 1 truck in the same lane at the same time because the 3 spans add up to a total length of 136 ft.

Multiple crossings were noted and recorded during some of the sampling periods. Table 3 gives a comparison of the stress ranges produced by 53 multiple crossings and by 1,170 single crossings. The mean value of the stress ranges for multiple crossings is approximately 2.3 ksi, while the mean value for the single crossings is approximately 1.9 ksi. This results in a significant difference at the 95 percent confidence

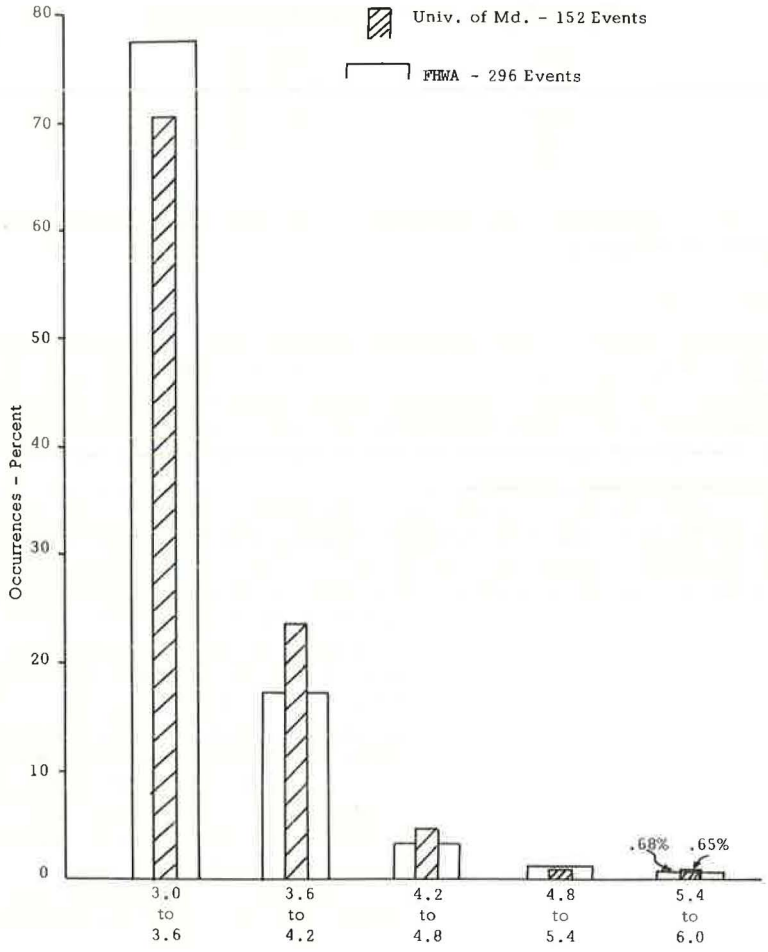

Figure 9. Stress ranges above 3 ksi.

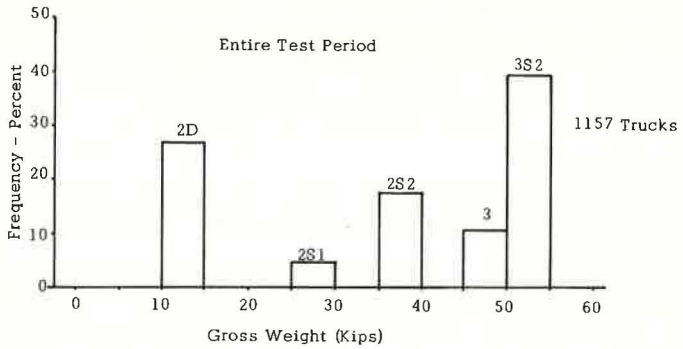

Figure 10. Frequency of mean gross weight of trucks for entire test period.

level, although it is seen in the table that none of the 53 multiple crossings produced a stress range greater than 4.2 ksi.

The 53 multiple crossings compared with the 1,170 single crossings should not be taken as a true indication of the frequency of occurrence of multiple crossings. The definition of "multiple" crossing in this test is very loose, in that what it means is that there was not time to make 2 clearly separate strain records when 2 or more trucks approached the bridge close to each other. The trucks could have been separated by as many as 150 ft as they crossed the bridge. Also, the 53 and the 1,170 crossings occurred in about 32 daylight hours in a total time of 4 days.

PROBABLE FATIGUE LIFE

Given certain material behavior characteristics under cyclic loading, and with certain other assumptions, an attempt can be made to determine the probable fatigue life of this structure.

Because there are no stress raisers, as in partial-length cover plates, it will be assumed that the governing material behavior will be that pertaining to plain rolled beams. The most critical section is the positive moment section in the side spans. Gage B1 was located in this section. The bridge is made continuous by riveted splices, which, of course, are not in places of high moment. The negative stresses, both calculated and measured, were not as high as the positive moment stresses.

Several different approaches to estimate the fatigue life of this structure will now be explored. The several methods are each somewhat related, and the assumptions associated with them will be presented for each use.

TABLE 3

STRESS RANGES CAUSED BY MULTIPLE AND SINGLE CROSSINGS

Stress Range (ksi)	Number of Occurrences	
	Multiple Crossings	Single Crossings
6.0		
5.4		1
4.8		1
4.2		7
3.6	4	32
3.0	7	100
2.4	12	201
1.8	15	246
1.2	10	297
0.6	5	251
0	—	34
Total	53	1,170

Root Mean Square Method

There are some limited laboratory fatigue data (4) that tend to indicate that one can relate random, variable load stress ranges to constant stress ranges by calculating the root mean square of the variable ranges, which is then assumed to produce the same damage as the constant stress range of the same value. Using the measured stress ranges and their frequencies above 3.0 ksi, one obtains a root mean square stress of 3.6 ksi.

In the recently completed and extensive tests of constant cycle fatigue made at Lehigh and Drexel Universities, the following relationship between constant cycle life and stress range for A-36 plain rolled sections was developed:

$$\text{Log } N = 10.637 - 2.943 \log Sr \qquad (1)$$

where Sr = stress range.

The laboratory investigation did not go beyond 10 million cycles, and it is, therefore, assumed that Eq. 1 holds true beyond this value. Substituting 3.6 ksi for Sr, one obtains a life of 1×10^9 cycles.

The present ADT across the bridge is about 10,000 vehicles. Assuming that 20 percent of this is trucks, one gets about 730,000 trips per year. If a further assumption is made that 12.5 percent of the trucks produce the 25 percent stress ranges above 3.0 ksi, there remain about 182,500 damage-producing stress ranges per year. The bridge was constructed in 1949 and, if whatever the traffic lacked in weight and frequency in the last 20 years will be made up in the next 20 years, one can assume that in 40 years there will be $40 \times 182{,}500 = 7{,}300{,}000$ cycles of damage-producing stress. This is still far below the 1×10^9 cycles to failure found earlier.

Another way of looking at this matter is to calculate backward in Eq. 1, substituting 7.3 million cycles for N. One gets a stress range of 18.7 ksi, which is above the combined dead and live load allowable stress.

Miner's Method

A more common procedure for estimating cumulative fatigue damage is to use Miner's hypothesis (5), which says that damage is proportional to the number of applied cycles divided by the total number necessary to produce failure at a certain stress range. The summation of all the fractions at the various stress ranges is equal to unity at failure.

To use this method, one must have an appropriate S-N curve, and one must know or properly estimate the number of cycles at the various stress ranges. Instead of an S-N curve, Eq. 1 will be used, again with the assumption that it holds true beyond 10 million cycles.

Based on the field test, it is estimated that the 182,500 yearly stress ranges above 3.0 ksi are distributed as follows:

ksi	Stress
3.3	127,750
3.9	36,500
4.5	9,125
5.1	5,475
5.7	1,825
6.3	1,825

It is also assumed that both the number and the distribution of stress ranges can be held constant for 40 years.

The summation of the fractions is less than 0.0005, and it is evident that this bridge does not have a fatigue problem.

Extreme Load Method

It is often argued that, although no danger of fatigue distress in highway bridges appear to exist at present, the weight and number of trucks are ever increasing and we must look to the future. Such an argument is not entirely valid because neither the weight nor the number of trucks on any road can increase upward without limits.

It is very rare to have truck volumes greater than 200 per hour on a highway. As the percentage of trucks increases, the total traffic volume decreases; thus, the average speed will also decrease, and the level of service generally deteriorates. How-

ever, to illustrate the effect of an "extreme" load condition, an attempt will be made here to produce an upper limit of truck traffic capacity across this bridge.

From the Highway Capacity Manual (6), it appears to be possible to have 420 trucks per hour on a 2-lane, 1-way, level highway, along with about 1,200 cars all traveling at 35 mph under ideal conditions. This adds up to 10,080 trucks per day and 3,679,200 trucks per year. If the bridge is in service for 30 years more, it will supposedly receive about 100 million truck crossings.

It is not too unreasonable to assume that the gross weight limit is 100 kips. It will be assumed for this calculation that at least half of the trucks are fully loaded to 100 kips. This is, of course, not substantiated by the present field tests.

An approximate relationship between gross weight and live load stress range was developed in an earlier investigation (7) for simple spans. This relationship adapted to the present case leads to the following expression:

$$Sr = 1.3 + 0.053\ G_W \qquad (2)$$

where G_W is the gross weight in kips. For 100 kips, this results in a stress range of 6.6 ksi. Assuming that this is the root mean square stress range introduced earlier and substituting Sr = 6.6 ksi into Eq. 1, we obtain a total of 210 million cycles necessary to produce failure.

Again, it is evident that, even under such abnormal traffic conditions, no fatigue distress will result in the plain rolled section under study. If the bridge had been constructed with beams that had partial length, end-welded cover plates, it could only withstand about 4 million cycles of a 6.6 ksi stress range. However, it could withstand the more realistic root mean square stress range of 3.6 ksi about 24 million times. This again assumes that the appropriate log N versus log Sr relationship is valid beyond 10 million cycles.

SUMMARY

The results of a loading-history field test on a rural highway bridge in Maryland were presented. Two ways of data reduction were compared: One technique noted only one stress event per truck passage, while the other technique produced several events for each vehicle. It was shown that the 2 methods could lead to widely different fatigue life assumptions, but that, for stress ranges above 3.0 ksi, practically identical stress-range distributions and frequencies resulted.

The composition of the present-day truck traffic was presented, with the weight data being adapted from the adjacent northbound lanes.

Several methods of estimating the remaining life of the bridge were presented. Some used conventional theories and constant cycle laboratory test data, while others relied on more recent test results and theories. One extreme case of traffic condition was also presented.

It is believed that the stress-range histogram as presented for the stresses above 3.0 ksi (Fig. 9) is meaningful and is representative of the present conditions on this structure.

The truck traffic classification is also believed to be representative of true conditions. A somewhat lower reliability should be placed on the truck weight data because it was obtained in the previous summer and borrowed from the adjacent roadway.

The dual truck crossing data should be regarded with the caution as previously described. It is believed that much fewer meaningful dual crossings occur than the data indicate.

Of the several methods of estimating the fatigue life of the structure, the root mean square method appears most promising, although whether this approximation of a constant stress cycle is always valid must be further tested in the laboratory.

The extreme loading method is somewhat extreme, however, it does serve the purpose of pointing out that structures with plain rolled beams are not likely to suffer from fatigue damage.

The assumption that the several log N versus log Sr relationships remain linear beyond 10 million cycles is probably not correct, but this assumption yields conservative results.

CONCLUSIONS

Several conclusions and recommendations can be made, based on the field test results and the accompanying fatigue analysis.

1. Significant differences in the shape of stress-range histograms can result, depending on the inclusion or exclusion of the several secondary stress ranges produced by a single vehicle.
2. No significant difference in the shape of the stress-range histograms resulted when only stress ranges above 3.0 ksi were considered. This conclusion may not be universally applicable to other bridges, and it is recommended that in other field tests, in addition to recording the major stress range produced by each vehicle, any secondary stress ranges above 3.0 ksi be recorded as well.
3. There was a significant difference between the means of stress ranges caused by dual crossings and those caused by single crossings. More experimental evidence on the nature and frequency of dual or multiple crossings needs to be gathered, including a variety of traffic situations.
4. It appears that the main load-carrying members of this bridge do not now, did not in the past, and likely will not ever in the future suffer fatigue distress caused by traffic-induced stresses. However, this conclusion has not been verified in this bridge for the deck reinforcing steel and secondary members, such as the diaphragms.
5. It also appears that some adjustments are needed in the main load member fatigue provisions of the 1969 AASHO Bridge Specifications. Both the allowable stress range and the number of design cycles should be modified. Field test results from this study showed that there was never a recorded live load stress range that exceeded one-half of the design live load with impact stress range.
6. Further laboratory fatigue work is recommended, both to extend S-N curves to as many as 200 million cycles, and especially to determine the effects of variable loadings.

ACKNOWLEDGMENTS

This work was a cooperative venture involving several administrative divisions of the Maryland State Roads Commission, the Federal Highway Administration, and the University of Maryland. Their cooperation is gratefully acknowledged. The help and counsel of A. D. Sartwell, W. L. Armstrong, and H. R. Laatz are especially appreciated.

REFERENCES

1. Sartwell, A. D., and Heins, C. P., Jr. Tabulation of Dynamic Strain Data on a Three-Span Continuous Bridge Structure. Univ. of Maryland, Civil Eng. Rept. 33, Nov. 1969.
2. Galambos, C. F., and Armstrong, W. L. Acquisition of Loading History Data on Highway Bridges. Public Roads, Vol. 35, No. 8, June 1969.
3. Sartwell, A. D., and Heins, C. P., Jr. Tabulation of Dynamic Strain Data on a Girder-Slab Bridge Structure During Seven Continuous Days. Univ. of Maryland, Civil Eng. Rept. 31, Sept. 1969.
4. Fisher, J. W., Frank, K. H., Hirt, M. A., and McNamee, B. M. Effect of Weldments on the Fatigue Strength of Steel Beams. Fritz Engineering Laboratory, Lehigh Univ., Rept. 334.2, Sept. 1969.
5. Miner, M. A. Cumulative Damage in Fatigue. Jour. of Applied Mechanics, June 1945.
6. Highway Capacity Manual. HRB Spec. Rept. 87, 1965.

DYNAMIC STRESS STUDY OF COMPOSITE-SPAN BRIDGE WITH CONVENTIONAL AND ELASTOMERIC BEARINGS

W. T. McKeel, Jr., and H. L. Kinnier, Virginia Highway Research Council

This paper describes an experimental study of the effects of dynamic loading on the vertical compressive deflections of elastomeric bearings and the influence of the flexible bearings on the response of the supported span. The primary test structure was a steel-beam, composite-span, highway bridge dynamically loaded by a test vehicle closely simulating an AASHO HS20-44 standard truck. The bearings investigated included 1 set of conventional steel rocker plate assemblies and 5 sets of elastomeric pads representing a wide range of practical design parameters.

Although the accepted compression-deflection relationship for elastomeric pads was verified experimentally in the subject study for both static and dynamic loading, it was concluded that deflections of full-sized bearings under either type of loading would be less than those predicted by the standard design curves. Analytical and model studies indicated that elastomeric bearings would reduce both the frequency of vibration of the supported span and the flexural stress in the structural members at resonance. The effect of the bearings in reducing the frequency of vibration of the span, however, was found to be slight; and under the realistic loading condition utilized, no practical advantage was indicated in reduced flexural stresses or increased damping of vibrations. However, a trend toward increased deflections of the span on elastomeric bearings was noted at all speeds of the test vehicle.

•ELASTOMERIC bridge bearings—pads of natural or synthetic rubber on which a beam rests and which deform to allow rotation, expansion, or contraction at the ends of the beam—are widely used in conjunction with both concrete and steel girders. The main advantage of elastomeric bearings lies in the economy resulting from low materials cost, ease of fabrication and installation, and little or no requirement for maintenance. The use of properly designed elastomeric bearings in lieu of more complex steel assemblies has resulted in cost savings in highway bridge construction, and field experience has generally confirmed their effectiveness.

There is a considerable body of research literature concerning elastomeric bearings, most of it concerned with laboratory tests to evaluate the performance of bearings fabricated of various compounds under conditions of static and cyclic loading at a practical range of temperatures. Little information is available on the response of bearings on an actual structure to dynamic loading or on the effect of the flexible bearings on the behavior of the supported span.

This paper reports the results of field tests of an actual highway bridge span supported on steel bearings and on 5 sets of elastomeric pads having a wide range of practical design parameters. The span was loaded during the tests by a 3-axle test vehicle that closely approximated an AASHO HS20-44 standard truck. The 2 primary purposes of this experimental investigation were as follows:

1. To determine the effects of a realistic dynamic loading on the vertical compressive deflections of the elastomeric pads included in the study and to compare the ex-

Sponsored by Committee on Dynamics and Field Testing of Bridges and presented at the 50th Annual Meeting.

perimental results with the empirical compression-deflection relationship on which the design of elastomeric bearings is largely based; and

2. To investigate the effects of the flexible bearings on the response of the supported span to dynamic loading and to compare the results, where applicable, with those of an analytical study reported by Zuk (1) and a model study performed by Emanuel and Ekberg (2).

The full-scale field tests can best be introduced by a brief discussion of the conventional compression-deflection relationship for elastomeric bearings and a review of the findings of the analytical and model studies.

COMPRESSION-DEFLECTION RELATIONSHIP FOR ELASTOMERIC BEARINGS

Perhaps the key factor in the design of elastomeric bearings is the vertical compressive deflection, which is generally held below a specified maximum value. The vertical compressive deflection is generally predicted on the basis of empirically derived standard curves that relate percentage deflection at a given load to the shape factor of the bearing and the hardness of the elastomer (3, 4).

The shape factor of an elastomeric bearing is defined as the ratio of the loaded area, which conventionally is the entire top face, to the area of the sides, which are free to bulge, as shown in the following for a rectangular pad:

$$\text{Shape factor} = \frac{l_p w_p}{2t_p(l_p + w_p)}$$

where

l_p = length of the pad;
w_p = width of the pad; and
t_p = thickness of the unloaded pad.

Hardness refers specifically to the relative resistance of an elastomer to surface indentation as measured by a durometer, a device with a spring-loaded probe that is pressed into the elastomer. The durometer indicates the hardness of the elastomer on an arbitrary scale from 0 to 100 for soft to hard materials. There is general agreement that durometer hardness does not provide an accurate measure of the stiffness of the compound, which is the property of interest (3, 4, 5). A general relationship does exist, but wide scatter is to be expected in a correlation of compressive stiffness and durometer values (3).

Most of the research on elastomeric bearings has been concerned, at least in part, with the compression-deflection relationship, and the standard curves have generally been verified within acceptable limits under laboratory conditions (2, 5, 6, 7). Thus, as indicated by the standard curves, the compressive stiffness of a bearing increases with higher shape factors and hardnesses, but tests of full-sized bearings have generally shown the pads to be stiffer than they were indicated to be by the standard curves.

ANALYTICAL AND MODEL STUDIES OF EFFECTS OF ELASTOMERIC BEARINGS

A theoretical study of the effect of flexible bearings on the vibration characteristics of a simply supported span has been reported by Zuk (1). Assuming that the vertical oscillations of a crossing truck would be equal to and in phase with those of the span at resonance, he developed an expression for the fundamental frequency of a beam on elastic supports with the vehicle at midspan. Equations for the ratios of amplitudes and stresses of the span on flexible bearings to those of the span on rigid bearings were also presented, as were sample computations based on sectional properties of typical bridges. Zuk's rather involved expressions will not be restated here; instead the results of the sample computations will be compared with the results of the model study by Emanuel and Ekberg (2).

Emanuel and Ekberg utilized a 25-ft steel-beam span that approximated a one-third scale model of a highway bridge span. The span, supported in various tests on curved steel sole plates and neoprene pads of 64 and 49 durometer hardness, was loaded by means of a counter-rotating eccentric weight oscillator at its center.

In general agreement with the theory developed by Zuk, Emanuel and Ekberg found the natural frequency of the model span to be lower when it was supported on elastomeric bearings, the softer bearings yielding the lower natural frequency. However, the difference between the experimental frequencies of the beam on the various bearings was always considerably less than that predicted by theory.

In both the analytical and model studies, maximum lower flange strain, that occurring at the respective natural frequencies, was less for the span on elastomeric bearings than on rigid bearings. This effect is shown graphically in Figure 1 (2, Fig. 1, p. 162), a plot of strain versus frequency for the 3 sets of bearings employed in the model study. The strain-frequency curves are similar in shape, but the curves for the elastomeric bearings are shifted to the left, which indicates the lower natural frequencies. The difference in maximum strain between the beam on steel bearings at its natural frequency and the beam on the 2 sets of elastomeric bearings at their natural frequencies is indicated by the relative ordinates of the peaks of the curves.

One point of contention existed between the analytical and model studies. Zuk's sample calculations indicated that deflections at the respective natural frequencies would be greater for the span supported on elastomeric bearings; however, the model study generally found the reverse to be true.

FULL-SCALE FIELD TESTS

Test Structures

The test structure, a typical highway bridge shown in Figure 2, was composed of a series of simply supported, rolled-beam composite spans, including 4 identical interior spans, two of which (spans 3 and 5) were chosen for instrumentation. The steel and

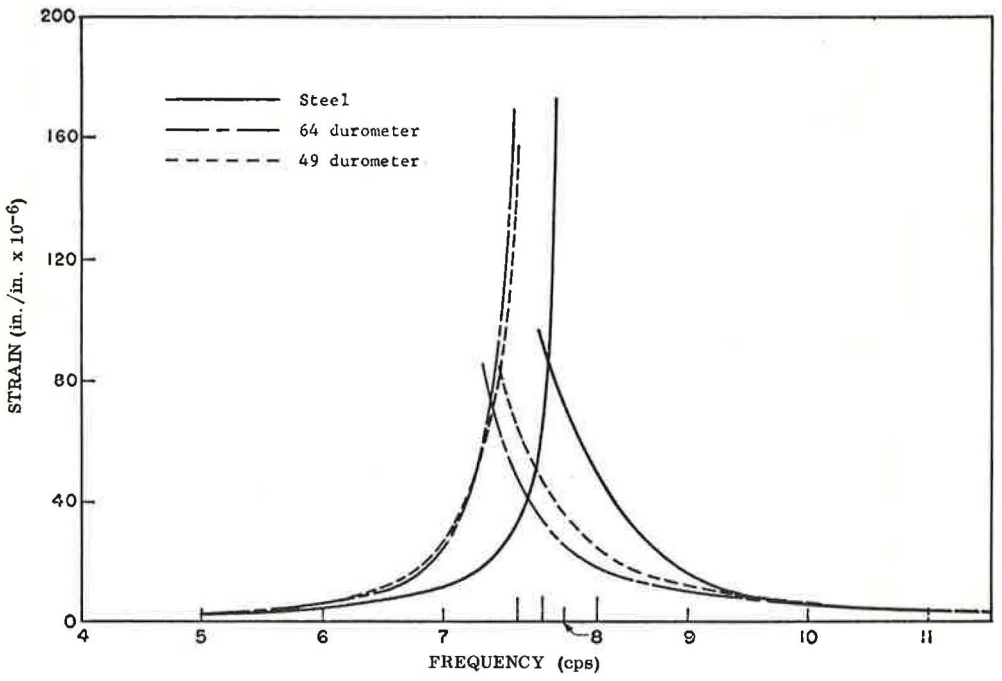

Figure 1. Typical strain-frequency curves for rigid and flexible bearings.

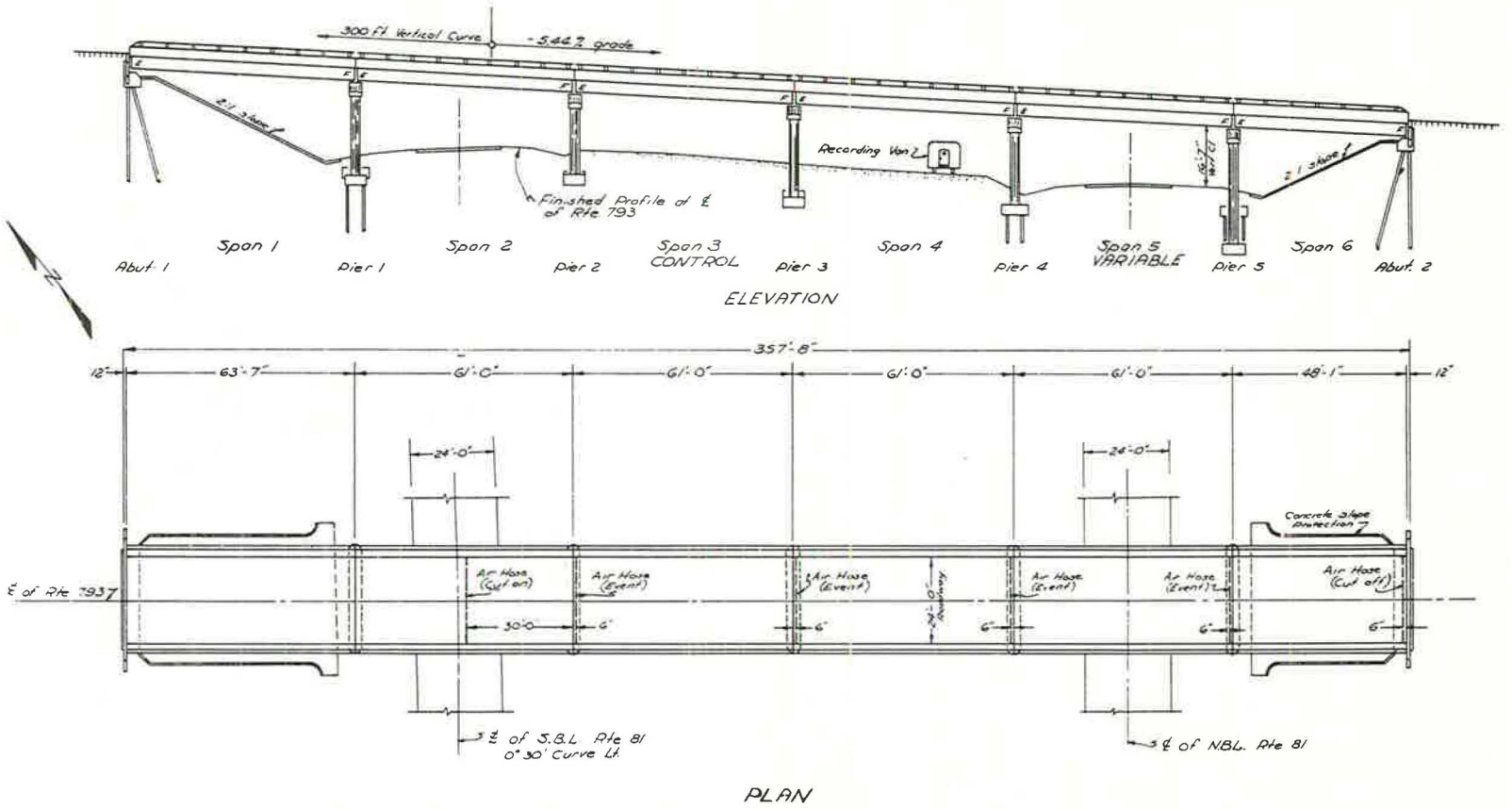

Figure 2. Plan and elevation of test structure indicating control and variable spans.

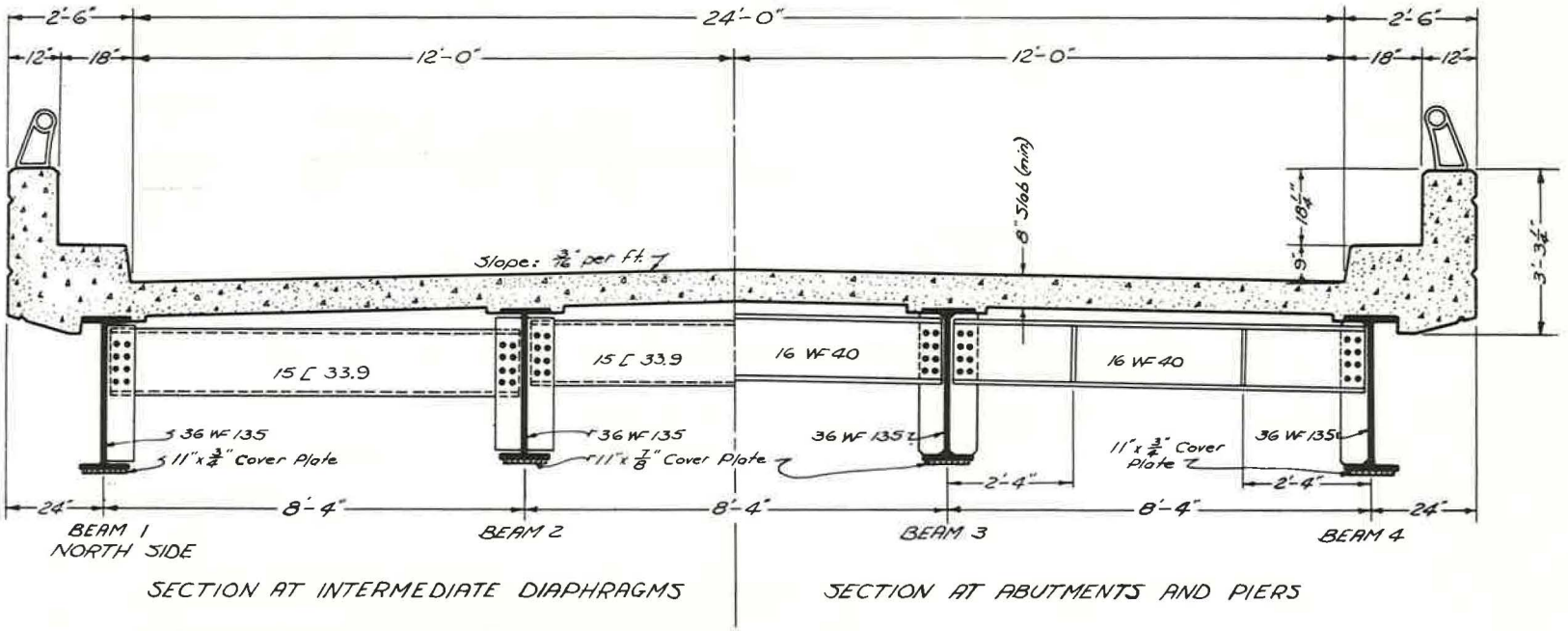

Figure 3. Typical transverse sections of test structure.

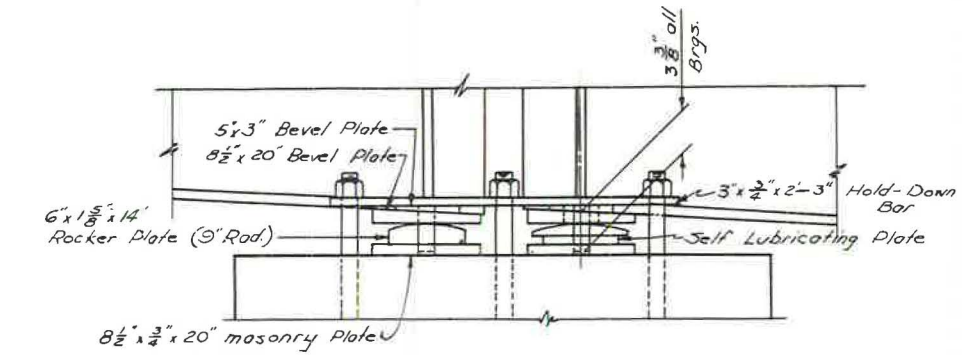

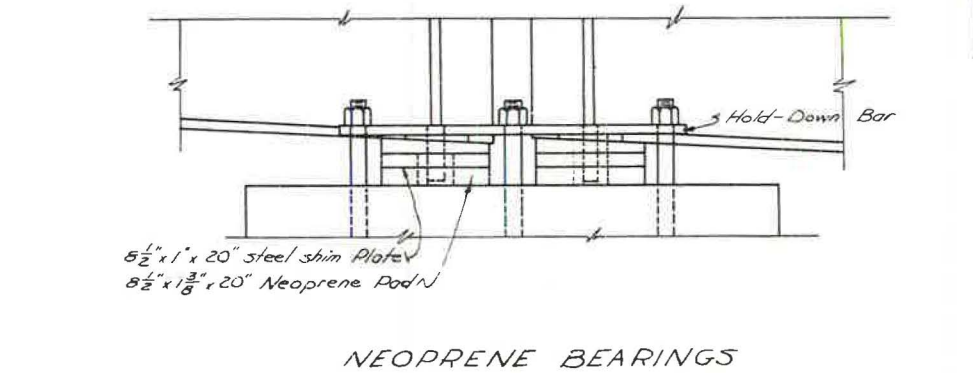

PROCEDURE FOR CHANGING BEARINGS

1. Remove anchor bolt nuts.
2. Jack span off bearings ($\frac{1}{4}$" max.)
3. Remove hold-down bars.
4. Remove masonry plates and rocker plates.
5. Insert neoprene pads and steel shims.
6. Align bearings and replace hold-down bars.
7. Release jacks and replace anchor bolt nuts.

Figure 4. Details of bearing assemblies with conventional steel bearings and original neoprene bearings and procedure for changing bearings.

elastomeric test bearings were interchanged on span 5, designated in Figure 2 as the variable span, while span 3, the control span, was supported on steel bearings throughout the study. The test spans had an identical cross section shown in Figure 3; stud shear connectors ensured composite action between the deck and the four W36 by 135 beams, which spanned 60 ft, center to center of bearings. The structure was designed for the HS20-44 standard loading in accordance with the AASHO 1961 Standard Specifications for Highway Bridges.

TABLE 1

DESIGN PROPERTIES OF TEST BEARINGS ON VARIABLE SPAN

Test Series	Type of Bearing	Approximate Shape Factor	Nominal Hardness
I	Elastomeric (bridge contractor)	1.7	70
II	Elastomeric	3.5	50
III	Elastomeric	8.4	50
IV	Elastomeric	3.5	70
V	Elastomeric	8.4	70
VI	Steel	–	–

Note: Steel bearings were used on control span for all test series.

A unique feature of the test structure was its specially designed bearing assemblies shown in Figure 4, which allowed the interchanging of steel rocker plates and elastomeric pads with a minimum of effort.

Bearing Details

The conventional steel bearings used on the control span throughout the tests and on the variable span during the final series of runs are also shown in Figure 4. These bearings allow for rotation of the end of the beam by means of the rockers and for expansion or contraction through sliding of the rocker plate on the self-lubricating plates in the expansion bearings.

In addition to the conventional bearings, 5 sets of neoprene pads were utilized in the field tests. The elastomeric bearings, of varying shape factors and hardnesses, included pads supplied by the bridge contractor according to the original design by the consulting engineer and 4 additional sets of bearings specially designed and fabricated for inclusion in the test program. The properties of the bearings for each of the 6 test series are given in Table 1.

The original elastomeric bearings supplied by the bridge contractor, series I, were solid neoprene rubber pads slotted to accommodate the studs on hold-down bars of the bearing assembly. Details of the pads are shown in Figure 5, and an average experimental compression-deflection curve based on static load tests of 2 pads is shown in Figure 6, as is the standard curve for a shape factor of 1.7 and a hardness of 70. In accordance with the findings of research cited previously, the experimental curve shown in Figure 6 indicates the full-sized pads to be 16 to 32 percent stiffer than the standard curve indicates them to be.

The bearings prepared specifically for the field tests, shown in Figure 7, are of a laminated construction and are smaller than the original neoprene bearings. Experimental compression-deflection curves based on laboratory static load tests of 1 bearing from each of the 4 groups, series II through V, are shown in Figure 8. In contrast to the theoretical effect of hardness, the 50-durometer pad with a shape factor of 8.4 appears stiffer than the corresponding 70-durometer pad. The cause of the discrepancy is impossible to explain with certainty, but it appears likely that the behavior of the sealing ribs that encompass the top and bottom of the pads might have affected the deflections in the single tests on which the curves are based.

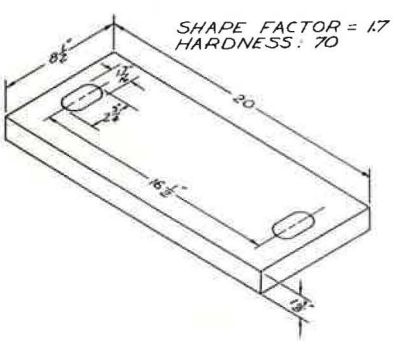

Figure 5. Details of elastomeric bearings for test series I.

Instrumentation and Experimental Procedure

The instrumentation included (a) strain gages on the top and bottom faces of the lower flanges at midspan on all beams in the 2 test spans and (b)

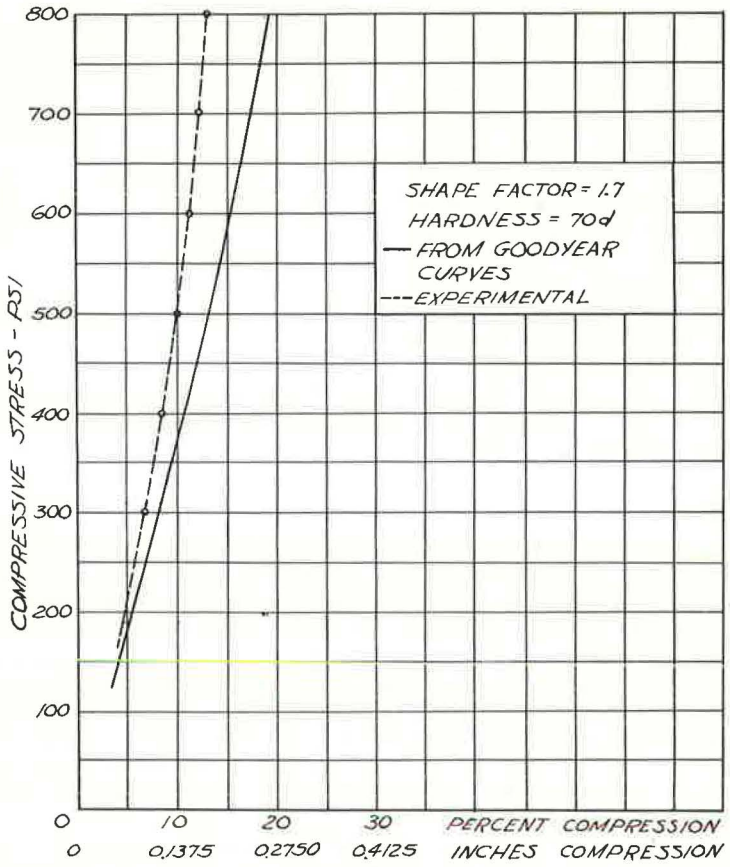

Figure 6. Experimental compression-deflection curve for original bearings and theoretical curve developed by interpolation from standard curves.

cantilever strip deflection gages, as shown in Figure 9, at the midpoint of all beams and over the bearings at both ends of the 2 interior beams on the variable span. The strain and deflection gages were connected to recording oscillographs that made a continuous trace of the gage outputs throughout the passage of the test vehicle.

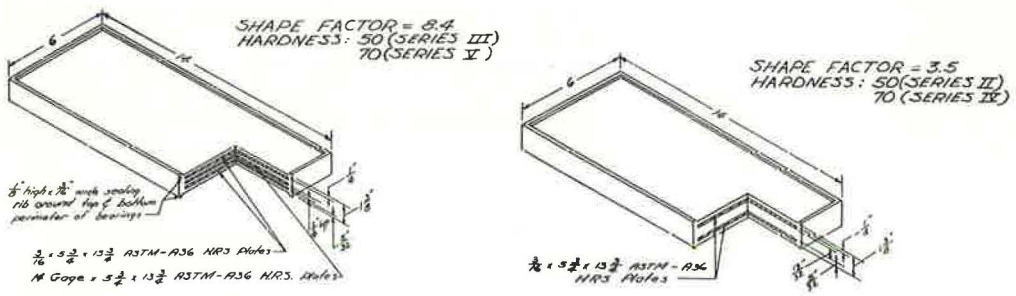

Figure 7. Details of elastomeric bearings designed for field tests.

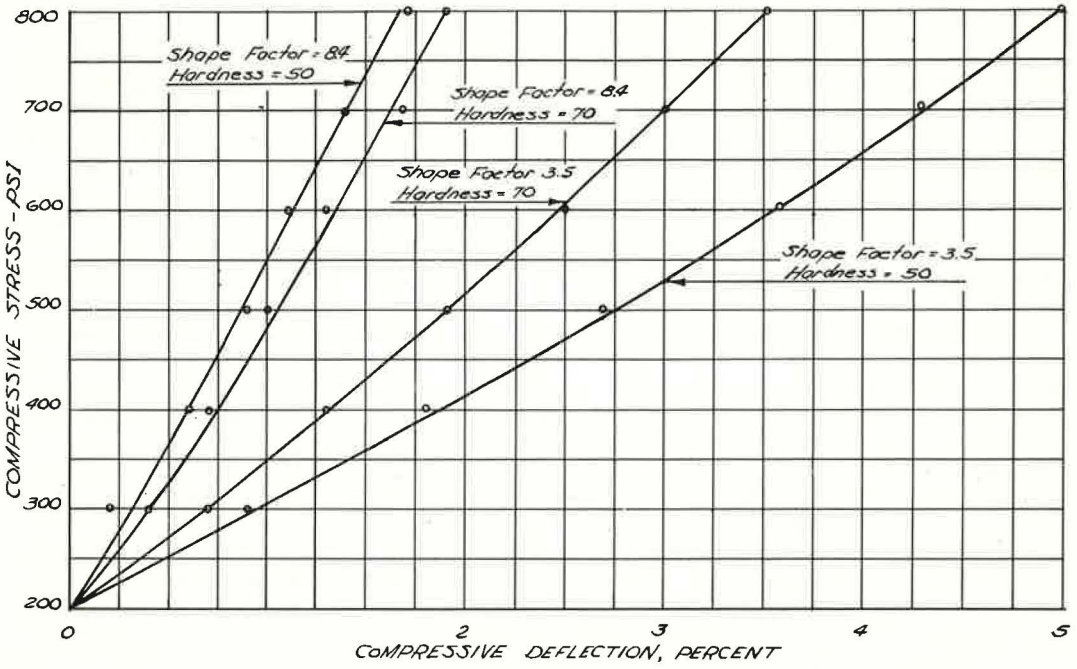

Figure 8. Experimental compression-deflection curves for bearings designed for field tests.

The test vehicle, a 3-axle diesel tractor semi-trailer loaded to closely simulate an AASHO HS20-44 standard truck, made runs in 3 lateral positions across the deck, in each of the 2 traffic lanes and directly on the centerline of the bridge roadway, at creep speed and at 10, 20, and 30 mph. Generally, time permitted only 2 repetitions of runs for each bearing type at each speed and position. The average measured speeds of the test vehicle were within 1 mph of the nominal speed in every case, and the average deviation of the test vehicle was less than 2 in. from the prescribed course in 75 percent of the runs.

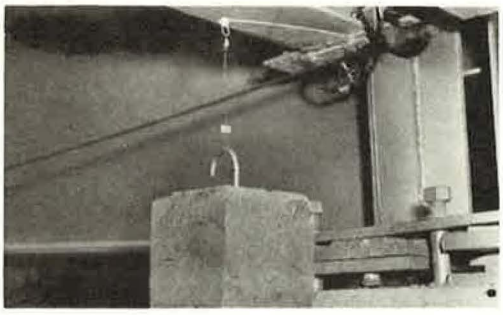

Figure 9. Typical deflection gage positioned on lower flange of diaphragm to measure bearing deflection.

DISCUSSION OF RESULTS

Nature of Results

A review of the results of this study must be made with a realization of the limitations inherent in the experimental procedure. Because of the rather extensive scope of the investigation, generally only 2 repetitions were made for each combination of vehicle speed and position and type of bearing; and the experimental results are sensitive to variations among individual runs. Accordingly, the analysis of the experimental results is generally qualitative in nature, and it is based on the identification of trends rather than on comparisons between individual values.

Deflections of Elastomeric Bearings

A cantilever strip deflection gage was mounted on the W16 by 40 end diaphragm of the bridge over each of the 2 interior bearings at both ends of the variable spans, as shown in Figure 9, with the arm extending toward the center of the structure. Thus, the gage measured deflections on only one side of the bearing from a position several inches above the bearing assembly, and some error due to distortion of the superstructure elements under load was inevitable. It is believed that an estimate of the error was provided by the data for the series VI tests at which time the variable span was supported on conventional bearings, and the average deflection recorded at the steel bearings during the series VI tests, 0.008 in., was subtracted from the recorded deflections of the elastomeric bearings.

The distribution of the live load reaction to the individual bearings was not determined experimentally. However, 2 distinct cases were studied analytically for the vehicle on the centerline of the bridge roadway: case A, which utilized a moment-distribution technique to determine the live load applied to the bearings; and case B, which was based on the portion of the live load carried by each stringer at midspan. The latter case is likely to be in error because of the increased transverse stiffness of the span at the bearings, but it presents a practical lower limit to the bearing reactions. Approximately 53 percent of the total reaction was distributed to each interior bearing in case A, with a corresponding uplift or negative reaction being indicated at the exterior bearings. The midspan lower flange stresses indicated that an average of 33.7 percent of the resisting moment was provided by beam 2 and 33.2 percent by beam 3, and the average of these values, 33.45 percent of the total reaction, was considered to be distributed to each interior beam in case B. The applied live load in either case is in addition to the computed dead load of 30.7 kips per bearing. The dead load and applied live load for both distributions and the corresponding compressive stresses are given for the test bearings in Table 2. The live load differs between the east and west bearings because site conditions allowed the heavy test vehicle to approach the bridge from only one direction.

Table 3 gives a comparison of the ranges and average values of the pad deflections recorded in the field test and the predicted values based on the experimental compression-deflection curves shown in Figures 6 and 8 and the standard curve shown in Figure 6. The data given in Table 3 indicate that, within the range of loading presented, the measured pad deflections are consistently smaller than predicted values based on the compression-deflection curves. The discrepancy between the field test deflections and those predicted by the standard curve is particularly great.

It appears reasonable that the discrepancy between the measured and predicted deflections might be due to the nature of the loading inasmuch as the dynamic modulus of rubber is invariably higher than the static modulus (3). Even at creep speed the load was applied fairly rapidly, and as each axle crossed the bearings and moved away an

TABLE 2

DEAD AND LIVE LOADS AND RESULTING COMPRESSIVE STRESSES IN ELASTOMERIC BEARINGS FOR VEHICLE ON CENTERLINE OF ROADWAY

Case	Nature of Loading	West Bearings (entry)			East Bearings (exit)		
		Load (kips)	Compressive Stress (psi)		Load (kips)	Compressive Stress (psi)	
			Series I	Series II Through V		Series I	Series II Through V
A	Dead load	30.7	190	365	30.7	190	365
	Live load	31.1	190	370	28.9	175	345
	Total	61.8	380	735	59.6	365	710
B	Dead load	30.7	190	365	30.7	190	365
	Live load	19.5	120	320	18.1	110	215
	Total	50.2	310	595	48.8	300	580

TABLE 3

COMPARISON OF ACTUAL AND PREDICTED DEFLECTIONS OF ELASTOMERIC BEARINGS

Test Series	Bearing	Experimental Deflections (in.)			Predicted Deflections (in.)			
					Case A Loading		Case B Loading	
		Measured Deflection Range	Corrected Deflection Range[a]	Corrected Average Deflection[a]	Experimental Curve	Standard Curve	Experimental Curve	Standard Curve
I	West	0.018 to 0.026	0.010 to 0.018	0.013	0.050	0.066	0.033	0.043
	East	0.018 to 0.019	0.010 to 0.011	0.011	0.045	0.060	0.030	0.038
II	West	0.014 to 0.024	0.006 to 0.016	0.013	0.030	0.065	0.020	0.041
	East	0.016 to 0.020	0.008 to 0.012	0.010	0.028	0.061	0.018	0.039
III	West	0.010 to 0.014	0.002 to 0.006	0.005	0.009	—[b]	0.006	—[b]
	East	0.012 to 0.014	0.004 to 0.006	0.005	0.009	—[b]	0.006	—[b]
IV	West	0.014 to 0.019	0.006 to 0.011	0.009	0.021	—[b]	0.013	—[b]
	East	0.015 to 0.018	0.007 to 0.010	0.009	0.019	—[b]	0.012	—[b]
V	West	0.010 to 0.012	0.002 to 0.004	0.003	0.010	—[b]	0.007	—[b]
	East	0.010 to 0.012	0.002 to 0.004	0.003	0.009	—[b]	0.006	—[b]

[a]Corrected deflection is measured value less estimated error of 0.008 in., the average deflection recorded during test series VI.
[b]Standard curves unavailable.

oscillating or cyclic loading resulted. In contrast, the compression-deflection curves were based on static tests in which the load was applied at an even rate. The error is compounded when the standard curves are used, because, as discussed previously, deflection showed by static tests of full-sized bearings at a given compressive stress are generally less than that predicted by the standard curves.

Figure 10 shows the average deflection recorded at the east and west bearings in the series II through V tests plotted against nominal vehicle speed for runs on the bridge centerline. The general relationship expressed by the standard curves, i.e., that compressive deflections decrease with increasing shape factor and hardness, is clearly verified.

Although the general relationship implicit in the standard curves has been verified, predicted live load deflections based on the curves have been consistently too high. However, because the design of elastomeric bearings is generally based on maximum allowable deflections, the error is conservative, and use of the readily available standard curves appears to be an acceptable practice.

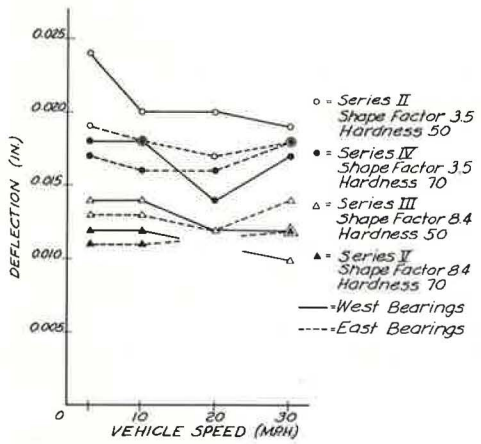

Figure 10. Average deflections for east and west bearings, test series II through V, position 2 runs, versus nominal speeds.

Vibration Characteristics of Supported Span

The fundamental natural frequencies of the 2 instrumented spans were determined experimentally from the gage traces after the test vehicle left the bridge. A comparison is given in Table 4 of the experimental frequencies and calculated values based on Zuk's work in the case of the span on elastomeric bearings and the following widely accepted equation for the span on steel bearings:

$$f = [\pi/(2L^2)]\ [(EI)/m]^{1/2}$$

where

L = length of the span;
EI = flexural rigidity of the span; and
m = mass of the span per unit length.

TABLE 4

SUMMARY OF AVERAGE EXPERIMENTAL AND THEORETICAL FREQUENCIES OF VIBRATION

Span	Test Series	Number of Values	Range of Values (cps)	Average Experimental Frequency (cps)	Theoretical Frequency (cps)
Variable	I	17	6.33 to 6.40	6.37	5.31
	II	48	6.17 to 6.29	6.23	5.36
	III	18	6.23 to 6.33	6.27	5.98
	IV	22	6.17 to 6.27	6.23	5.63
	V	20	6.17 to 6.30	6.21	5.96
	VI	3	6.25 to 6.29	6.28	6.35
Control	All	131	6.37 to 6.49	6.43	6.35

The agreement between the measured and computed frequencies of the variable and control spans supported on steel bearings can be considered good. However, the experimental values for the span on elastomeric bearings are not arranged in accordance with theory, and, except for the unexplainably high values in the series I tests, there is little difference in the frequency values associated with the various bearings. Emanuel and Ekberg, in their more closely controlled experiment, did verify the effect of flexible bearings in decreasing the natural frequency of the span, but their experimental values differed by considerably less than those predicted by theory (2). It, therefore, appears that the degree of the effect of flexible bearings on frequency predicted by the theoretical study might be in error, possibly because of the increased stiffness exhibited by the bearings under dynamic loading. The data given in Table 4 indicate at most a rather slight decrease in the natural frequency of the span due to the use of elastomeric bearings, and, in fact, the frequency could be computed with acceptable accuracy by means of the expression applied to the span on steel bearings.

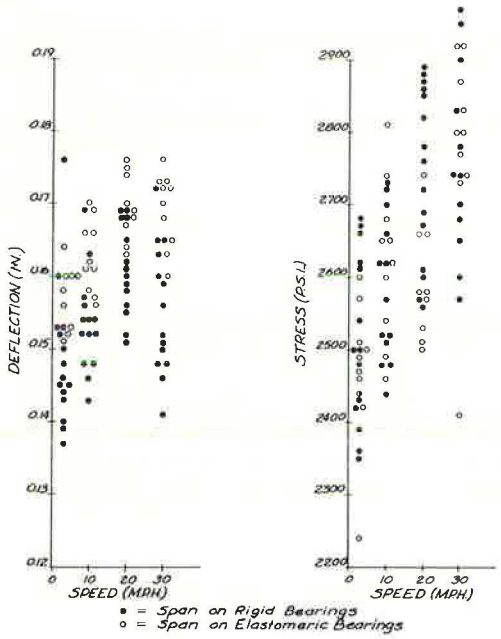

Figure 11. Peak midspan deflections and lower flange stresses in interior beams versus nominal speed for test vehicle on bridge centerline.

Average logarithmic decrements of the oscillations of the instrumented spans, indicators of the rate of damping of the vibrations, were also obtained experimentally from gage traces showing a regular decay pattern. A comparison of the effect of the elastomeric bearings on the damping of vibrations was essentially precluded by a scarcity of data for the variable span supported on steel bearings; however, 2 conclusions were possible on the basis of the limited data. First, the difference in the logarithmic decrements obtained for the variable span on elastomeric bearings having a wide range of shape factors and hardnesses was insignificant in consideration of the wide range of experimental values obtained in each case. Second, the damping ratios for all series and both spans were quite low, less than 1 percent of critical damping in every instance, and the practical advantage in improved damping, if any exists, can probably be considered negligible.

A comparison of the maximum double amplitudes of stringer oscillations for the

2 instrumented spans in each series and of the series VI results against those of the other series disclosed no consistent difference that could be attributed to the type of bearing. The experimental scatter typical of double amplitude data would have obscured minor effects of the bearings, but it is believed that variations of practical significance would have been apparent.

Dynamic Stress and Deflection Response of Supported Span

Figure 11 shows plots of midspan deflections and lower flange stresses in the 2 interior beams versus nominal speeds for the test vehicle crossing the instrumented spans on the centerline of the bridge roadway. The deflection data indicate a tendency toward greater deflections for the variable span on elastomeric bearings, but the effect of individual elastomeric bearings was obscured by experimental scatter. Because the moderate increase in deflections is not accompanied by greater stresses, it is believed to be caused by the action of the flexible bearings.

There was no consistent difference evident in the stresses in the beams of the variable and control spans that could be attributed to the type of bearing employed. Although the stress shows a general tendency to increase with increasing speed of the test vehicle, the difference in maximum flexural stress at resonance, indicated by the work of Zuk and verified by Emanuel and Ekberg, was not apparent under the realistic loading conditions employed in the field tests. The condition of resonance is difficult to define in the case of an initially oscillating mass on 3 axles, but it is believed that the amplification of response associated with resonance would not occur. It is, therefore, doubtful that an advantage in reduced stress would be gained through the use of elastomeric bearings under normal loading conditions.

Average live load impact factors based on the percentage increase in stress and deflection with respect to the values at creep speed exhibited no consistent variation that could be related to the nature of the bearings. Regardless of the nature of the bearings and throughout the range of speeds, the experimental impact percentages of the most heavily loaded beams were lower than the design impact factor of 27 percent (calculated in accordance with the AASHO Specifications for Highway Bridges) in all but one passage of the test vehicle. The experimental impact percentage consistently exceeded the AASHO value only in the case of the lightly loaded beams farthest from the test vehicle, for which the effect was insignificant. Most of the values obtained for the 2 beams directly under the test vehicle were less than 20 percent.

CONCLUSIONS

The experimental results of the subject field tests represent the response of a rather complex structure to loading by an elaborate dynamic system with numerous degrees of freedom. The conclusions are thus qualitative in nature, and they are applicable primarily to the structure and test vehicle utilized in the investigation and to the response at a limited range of speeds. It is believed, however, that the results are indicative of the effects of a realistic loading on an actual highway bridge span.

1. The general relationship indicated by the standard curves, that compressive deflections decrease with increasing shape factor and hardness, is apparent under both static and dynamic loading.
2. Static compression-deflection tests of elastomeric pads having a relatively wide range of shape factors and hardnesses indicated that the stiffness exhibited by full-sized bridge bearings is greater than that indicated by the standard design curves.
3. The dynamic compressive deflections of elastomeric bearings caused by a rapidly applied oscillating live load, not including the effects of dynamic creep, are consistently smaller than the values predicted by either experimental or standard curves based on static tests. The discrepancy in the case of the standard curves is particularly great. However, because the design of elastomeric bearings is based on maximum allowable deflections, the error inherent in the use of the standard curves is conservative.
4. Elastomeric bearings tend to reduce the natural frequency of vibration of the supported span, but the effect of the bearings is slight. The natural frequency can be

predicted with acceptable accuracy by expressions commonly applied to spans on rigid bearings.

5. The damping of vibrations in a span on elastomeric bearings is not affected to a significant degree by pad characteristics including a wide range of practical shape factors and hardnesses.

6. Although a complete comparison of the damping of vibrations in a span on elastomeric and rigid bearings was precluded by a scarcity of data, the damping ratios for both spans on all types of bearings were low, less than 1 percent of critical damping in every case. It appears likely that any increased damping due to the use of elastomeric bearings would be of little practical advantage.

7. The nature of the bearings has no significant effect on the magnitude of the maximum amplitude of oscillation.

8. Beam deflections may be moderately increased by the use of elastomeric bearings under normal loading conditions. Because the increased deflections are not accompanied by higher stresses, the trend is attributed to the effect of the bearings.

9. It is doubtful that an advantage in reduced stresses will be gained through the use of elastomeric bearings under normal loading conditions. It is perhaps also important to note that no disadvantages in increased stress are apparent in the use of elastomeric bearings.

10. The nature of the bearings, either rigid or elastomeric, has no apparent effect on the impact percentage with respect to either stress or deflection.

ACKNOWLEDGMENTS

This paper is based on the findings of a cooperative research project of the Virginia Highway Research Council and the Federal Highway Administration. The research was conducted under the general supervision of the late Tilton E. Shelburne and, more recently, Jack H. Dillard of the Virginia Highway Research Council and Charles F. Scheffey of the Federal Highway Administration. The experimental data were taken under the joint direction of Robert F. Varney of the Federal Highway Administration and the authors of this paper. The General Tire and Rubber Company fabricated most of the test bearings utilized in this study and provided technical assistance.

REFERENCES

1. Zuk, W. Bridge Vibrations as Influenced by Elastomeric Bearings. HRB Bull. 315, 1962, pp. 27-34.
2. Emanuel, J. H., and Ekberg, C. E., Jr. Problems of Bridge Supporting and Expansion Devices and an Experimental Comparison of the Dynamic Behavior of Rigid and Elastomeric Bearings. Iowa Eng. Exp. Station, special rept., 1965.
3. Handbook of Molded and Extruded Rubber. Goodyear Tire and Rubber Co., 1949.
4. Design of Neoprene Bridge Bearing Pads. E. I. duPont de Nemours & Co., 1959.
5. Pare, R. L., and Keiner, E. P. Elastomeric Bridge Bearings. HRB Bull. 242, 1960, pp. 1-19.
6. Clark, E. F., and Moultrop, K. Load-Deformation Characteristics of Elastomeric Bearing Pads. Highway Research Record 34, 1963, pp. 40-116.
7. Aldridge, W. W., and Sestak, J. J., Jr. Tests on Five Elastomeric Bridge Bearing Materials. Highway Research Record 253, 1968, pp. 72-83.

CONTROL OF SINGLE-SPAN HIGHWAY BRIDGE VIBRATIONS

Thomas F. Derby and Peter C. Calcaterra, Barry Controls,
Division of Barry Wright Corporation, Watertown, Massachusetts

The investigation deals with a comparison of the dynamic response of various bridge designs to individual heavy vehicle crossings and with an evaluation of several techniques for reducing the resultant dynamic motions of long-span bridges. Four single-span bridge designs, all 250 ft in length, are considered: concrete and orthotropic composite deck constructions using both low-alloy structural steel and high-strength steel. The vibratory motions of each untreated bridge are calculated as a function of vehicle type and speed and of roadway characteristics (idealized smooth road and roadway roughness), based on simplified model representations for the bridge and vehicle. Four treatments for bridge vibration control are analyzed: rigidization, damping, passive absorbers, and active absorbers. A comparison is made between the response of the untreated and treated bridges, and the effectiveness of each treatment in reducing the dynamic motions of the untreated bridges is evaluated. Designs are evolved for each treatment, and a comparison is made on the basis of cost effectiveness. Conclusions are made regarding the dynamic response of each type of bridge design, the effectiveness of each treatment, and the choice of treatment.

•LONG-TERM trends in highway bridge design favor the construction of longer spans. Longer span bridges may be designed more economically with higher strength steels now available than with low-alloy structural steels. However, in order to realize the full economic advantage of these new materials, bridges designed with higher strength steel would be inherently more flexible.

Vibratory motions are induced in highway bridge structural members because of the passage of vehicles. In longer, more flexible spans, the magnitude of the dynamic motion may be of sufficient magnitude to result in annoying and often frightening sensations to pedestrians. In addition, increases in dynamic stress could give rise to fatigue failures. Current design specifications inhibit bridge vibrations only indirectly by controlling the stiffness of the bridge span through deflection and depth-to-span ratio limitations. These limitations have the unwanted effect of restricting the use of economical high-strength materials whose greater flexibility for a given span would not meet the present deflection requirements.

This paper considers various means, referred to as treatments, of reducing the dynamic motion of the bridge. These include rigidization, damping, and absorbers, both passive and active. The treatments should be considered as additions to the bridge structure in the event that vibration levels due to vehicle crossings are found to be excessive. In each case performance and treatment-selection criteria are developed. In addition, estimates are made of the cost associated with each treatment, and a cost effectiveness of each treatment is calculated.

BRIDGE DYNAMIC RESPONSE

If the dynamic effects due to the interaction between the bridge and the vehicle are not taken into account, the deflection of any point on the bridge due to passage of the

Sponsored by Committee on Dynamics and Field Testing of Bridges and presented at the 50th Annual Meeting.

vehicle would be dependent only on the weight and location of the vehicle. Let the deflection at midspan of a single-span bridge due to a vehicle moving very slowly over the bridge, so as to render dynamic effects to be negligible, be called the crawl deflection. However, because dynamic effects do occur, the dynamic bridge deflection at midspan while the vehicle is on the bridge differs from the crawl deflection. The crawl deflection and dynamic deflection curves are shown in Figure 1 as a function of vehicle location. The difference between the crawl deflection and the dynamic deflection curves is referred to as dynamic increment, DI. Figure 1 also shows the residual vibration of the bridge after the vehicle leaves the span. The effectiveness of the various treatments in reducing residual bridge vibrations is discussed in another report (1).

Two characteristics of the dynamic increment are considered in the response of a bridge for a particular vehicle, speed, and roadway condition:

1. DI_{max}, maximum value of the dynamic increment (the vehicle location along the bridge at which DI_{max} occurs is also of importance); and
2. DI_{rms}, root mean square value of the dynamic increment defined as

$$DI_{rms} = \sqrt{1/T \int_0^T (DI)^2 \, dt} \qquad (1)$$

where T = time for vehicle to cross bridge, bridge length/vehicle speed.

BRIDGE MODEL

The bridge is modeled as a uniform beam, simply supported at both ends, and the Bernoulli-Euler beam vibration theory with damping is used. Only the first 3 modes are considered.

The hypothetical bridges selected for this study are single-span, steel girder bridges, all 250 ft in length. This length is longer than that of the majority of steel girder bridges now in existence. Four types of bridges are considered and are labeled S-C, NS-C, S-O, and NS-O. Two of the bridges, S-C and NS-C, have concrete decks

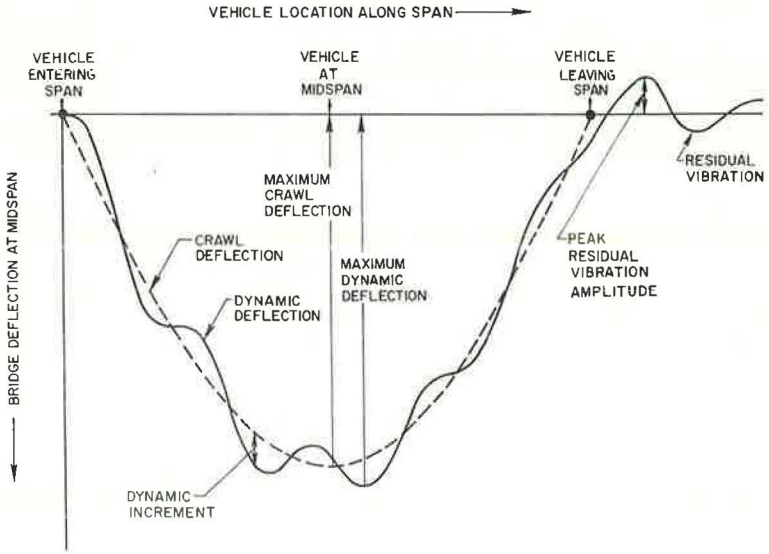

Figure 1. Typical deflection curves of bridge response at midspan as a function of vehicle location along span.

with shear connectors. One of these bridges, S-C, is built of low-alloy structural steel (ASTM A 588, design stress 27,000 psi) and meets AASHO deflection limitations. The second concrete deck bridge, NS-C, utilizes high-strength steel (ASTM A 514, design stress 55,000 psi) and does not meet AASHO deflection limitations. The remaining 2 bridges, S-O and NS-O, have orthotropic steel plate decks. One of them, S-O, is built of low-alloy structural steel and meets AASHO deflection requirements, and the other, NS-O, is built of high-strength steel and does not meet AASHO deflection requirements.

The bridges that did not meet the AASHO deflection requirements, NS-C and NS-O, also did not meet AASHO depth-to-span ratio criteria. However, all other AASHO requirements were met for all 4 bridge designs.

The sections used in all 4 bridges each consist of two 12-ft lanes and one 10-ft shoulder or 34 ft curb-to-curb with parapets on either side. All designs utilize steel girders spaced at 10.75 ft on center. In the orthotropic plate designs, it was assumed that the deck weight was 37 lb/sq ft. For bridges NS-C and NS-O, the design uses hybrid girders, that is, a low-strength, less expensive steel for the web section and a high-strength steel for the flange section. The allowable stress in the flange of the hybrid girders has been reduced in accordance with AASHO.

For the purpose of estimating the cost of the steel section, the unit prices used are as follows: web steel, A 588, 29 cents/lb; flange steel, A 588, 30 cents/lb; and flange steel, A 514, 42 cents/lb. These prices reflect the contractors bid price, complete in place. Because the costs of deck, parapets, abutments, rail, and the like would be comparable under either scheme, they are not reflected here. The properties, characteristics, and costs of all 4 bridges are given in Table 1. Typical cross sections of the concrete deck and orthotropic deck designs are shown in Figure 2.

ROADWAY CHARACTERISTICS

The interaction between the dynamic motion of a bridge and the vehicle is complex and is influenced primarily by the characteristics of their interface, namely, the bridge deck. In addition, the vehicle enters the bridge with initial conditions that are a function of the characteristics of the approach roadway and of vehicle speed. In order to separate the effects of the vehicle weight from those of the bridge deck, 2 roadway conditions are considered in the investigation: idealized smooth road and road roughness.

Idealized Smooth Road Condition

In order to evaluate the effect of just the vehicle weight traveling across the bridge, it is convenient to assume that both the approach roadway and the bridge deck are

TABLE 1

PROPERTIES, CHARACTERISTICS, AND COSTS OF SELECTED 250 FT LONG BRIDGES

Bridge	Construction	Total Moment of Inertia (in^4)	Total Weight (kip)	Live Load Plus Impact Deflection at Midspan[a] (in.)	Natural Frequency[b] (Hz)	Web[c] (in.)	Top Flange (in.)	Bottom Flange (in.)	Steel Cost (dollars)
S-C	ASTM A 588 steel concrete deck	4,129,288	1,733	1.91	1.58	140 × ½	22 × 1⅞	24 × 2½	172,440
NS-C	ASTM A 514 steel concrete deck	1,891,244	1,555	4.16	1.12	110 × 5/16	14 × 1½	18 × 2	142,520
S-O	ASTM A 588 steel orthotropic deck	2,141,416	979	3.68	1.52	157 × 9/16	14 × 2	14 × 2	168,810
NS-O	ASTM A 514 steel orthotropic deck	588,460	695	13.38	0.95	86 × 7/16	16 × 2	16 × 2	102,460

[a]Allowable live load plus impact deflection according to AASHO deflection limitation for a 250-ft bridge = 3.75 in. Live Load, HS20.
[b]First bending mode.
[c]In all cases the depth of web was determined by economy only.

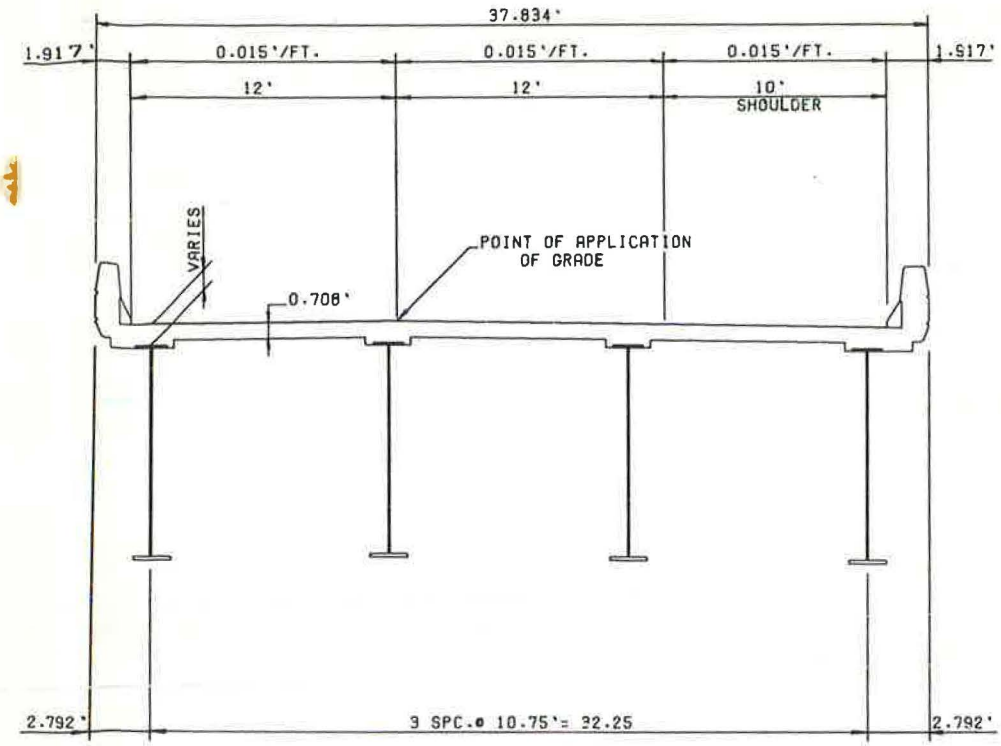

with concrete deck

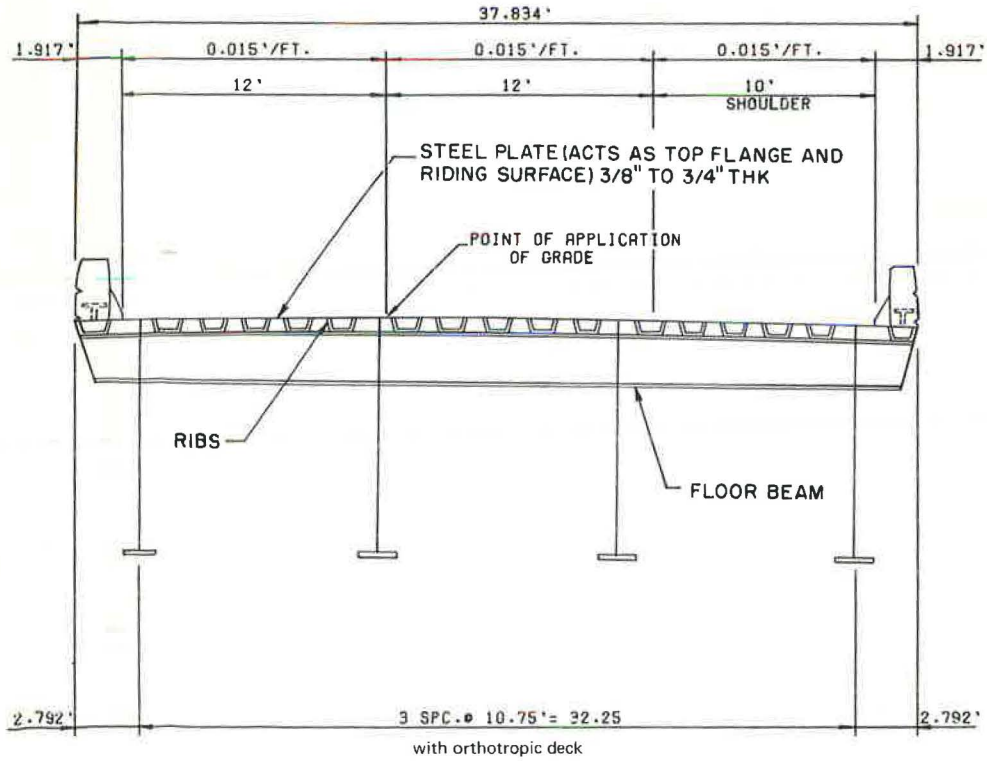

with orthotropic deck

Figure 2. Typical cross sections of steel girder bridge.

"ideally" smooth. It must be emphasized that such a condition is purely a mathematical one and physically unrealizable because irregularities cannot be avoided in roadway construction. The dynamic motions that occur when a vehicle traverses a bridge under this condition (which is similar to the bridge response to a moving force of magnitude equal to the vehicle weight) represent only a portion of the total bridge response. The response under the rough road condition inherently includes the response of the bridge to the idealized smooth road condition.

Road Roughness Condition

The most realistic condition can be considered to be one in which both the bridge approach roadway and the bridge deck have irregular profiles. The vehicle enters the span with certain initial conditions, and forced oscillations are induced on the bridge as the vehicle interacts with the structure as a result of the roughness of the deck. Therefore, for this case, the response of the bridge is the sum of these oscillations and the motions associated with the idealized smooth road response. The total response can be larger or smaller than the motions due to the vehicle weight alone, depending on phase relationships, frequency content of the deck irregularities, and frequency and speed of the vehicle.

This condition requires definition of the road profile for both the approach roadway and the bridge deck. The profile for both the approach roadway and bridge deck selected for the investigation is based on data from a "poor flexible" pavement (2) and can be mathematically represented as the sum of 20 sine functions as follows:

$$r(x) = \sum_{i=1}^{20} A_i \sin(2\pi\nu_i x + \phi_i) \qquad (2)$$

where A_i is the amplitude, ft; ν_i is the spatial frequency, cycles per foot; ϕ_i is the phase angle; and x is the distance along the bridge measured from the beginning of the span, ft. The spatial frequencies were chosen between 0.005 and 0.5 so that they would be equally spaced on log paper. The amplitudes were chosen to be proportional to $\sqrt{S_i \Delta\nu_i}$, where S_i is the power spectral density at frequency ν_i, and $\Delta\nu_i$ is the bandwidth for which ν_i is the center frequency. The phase angles were chosen randomly from a square distribution between 0 and 2π radians. The values of A_i, ν_i, and ϕ_i are given in Table 2. In the analysis, the approach roadway and bridge deck profiles are considered to be continuous. The vehicle is assumed to have traveled over the road profile for a sufficient length of time to have achieved a steady-state motion. The vehicle then enters the bridge roadway with specific initial conditions that are a function of vehicle parameters and speed.

TABLE 2

VALUES OF AMPLITUDES, FREQUENCIES, AND PHASE ANGLES FOR ROAD PROFILE

i	Amplitude, A_i (ft)	Frequency, ν_i (cps)	Phase Angle, ϕ_i (radian)	i	Amplitude, A_i (ft)	Frequency, ν_i (cps)	Phase Angle, ϕ_i (radian)
1	0.0246	0.0056	2.98	11	0.0055	0.0565	0.19
2	0.0211	0.0071	2.78	12	0.0047	0.0712	4.74
3	0.0182	0.0089	3.13	13	0.0041	0.0895	3.13
4	0.0157	0.0113	2.34	14	0.0035	0.1130	1.53
5	0.0135	0.0142	5.79	15	0.0030	0.1420	0.58
6	0.0116	0.0179	0.78	16	0.0026	0.1790	1.76
7	0.0100	0.0225	0.55	17	0.0022	0.2250	1.00
8	0.0086	0.0283	0.25	18	0.0019	0.2830	1.33
9	0.0074	0.0356	2.14	19	0.0017	0.3560	0.27
10	0.0064	0.0449	2.95	20	0.0014	0.4490	2.41

VEHICLE MODEL

For this investigation, the model chosen for the vehicle is shown in Figure 3. The suspension system is represented by a spring and viscous damper in parallel. The effect of the axle and tire mass is ignored, and the tire stiffness is represented by a spring. To completely specify the vehicle parameters, it is necessary to define the mass, the 2 spring stiffnesses, and the damping coefficient. For convenience, the vehicle parameters are expressed in terms of vehicle weight, W_V; damped natural frequency, f_r; undamped resonant frequency, f_o; ratio of tire stiffness to suspension system stiffness, N; and critical damping ratio, ζ. For the model, the relationship between these parameters is given by

$$4\zeta^2 (8\zeta^2 - N - 2)(f_r/f_o)^6 + 16\zeta^2 (N + 1 - 2N\zeta^2)(f_r/f_o)^4 + 2 (4N\zeta^2 + N + 1)(f_r/f_o)^2 - 2N = 0 \quad (3)$$

where

$\zeta = C_V/2\sqrt{M_V K_V}$;

$f_o = \frac{1}{2\pi}\sqrt{K_V/M_V}$; and

$W_V = M_V/g$.

Justification for the model chosen and selection of vehicle parameters are based on a comparison between the road profile spectral density measured with a test vehicle over the selected poor flexible pavement and that calculated by using the vehicle model. From a report by Whittemore et al. (2), a test run was chosen for a vehicle weighing 9,400 lb, having a natural frequency of 3 Hz, and traveling at 34 mph. The profile defined by Eq. 2 and the model shown in Figure 3 with the same value of weight, natural frequency, and speed as the test vehicle were used to calculate theoretical pavement load power spectral density curves for various selected values of N and ζ. Values of N = 8.37 and ζ = 2.5 resulted in the theoretical curve that best matched the experimental one. It was assumed that all vehicles considered in this study would have these same values of N and ζ. On this basis, 3 vehicles were selected with different values of weight and natural frequency as shown in Figure 3. Each of the vehicles is considered to travel at three speeds: 20, 40, and 60 mph.

DESCRIPTION OF TREATMENTS

Rigidization

The treatment termed rigidization involves the addition of steel to the bridge to increase its stiffness. This is a rather standard procedure currently used for reducing bridge dynamic motion.

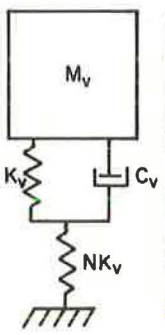

VEHICLE CHARACTERISTICS	
FREQUENCY, f_r (Hz)	WEIGHT, W_V (lb)
1.7	50,000
2.0	33,000
2.5	20,000

Figure 3. Vehicle model and characteristics used in this study.

The rigidization treatments have the effect of decreasing the live load deflections by a certain percentage. Two levels of live load deflection reduction were selected for each bridge: low (approximately 25 percent reduction) and high (approximately 50 percent reduction).

The added steel is welded to the bridge in the most effective places so that a minimum amount of steel is needed for a maximum increase in stiffness; this implies that the steel is to be added to the bottom and top of existing flanges. The increase in area of these flanges is given in Table 3. Each bridge that has been rigidized will then have a new value of stiffness and a new total weight that

TABLE 3

PROPERTIES OF RIGIDIZED BRIDGES

Item	Low Values of Rigidization				High Values of Rigidization			
	Bridge S-C	Bridge NS-C	Bridge S-O	Bridge NS-O	Bridge S-C	Bridge NS-C	Bridge S-O	Bridge NS-O
Design live load deflection[a], in.	1.91	4.16	3.68	13.38	1.91	4.16	3.68	13.38
New live load deflection, in.	1.44	3.10	2.70	9.93	1.22	2.08	1.88	6.73
Reduction in live load deflection, percent	25	25	26	26	36	50	49	50
Increase in area of girder flanges, in^2								
Top	0	0	0	0	63.75	53.75	17	16
Bottom	45	30	38	34	45	69	77	73
Total weight increase for all 4 girders, kip								
Top	0	0	0	0	217	183	58	55
Bottom	153	102	129	116	153	234	262	248
Total	153	102	129	116	370	417	320	303
Midspan lower flange stress increase due to total weight of added steel, psi	1,290	1,600	1,820	3,320	3,140	6,550	4,500	8,690
Increase in midspan lower flange stress due to weight of added steel[b], percent	4.8	2.9	6.7	6.0	11.4	11.9	16.7	15.8
Total design weight of bridge[a], kip	1,733	1,555	979	695	1,733	1,555	979	695
New total weight of rigidized bridges, kip	1,886	1,657	1,108	811	2,103	1,972	1,299	998
Design total moment of inertia[a], in^4	4,129,288	1,891,244	2,141,416	588,460	4,129,288	1,891,244	2,141,416	588,460
New total moment of inertia of rigidized bridges, in^4	5,466,488	2,540,837	2,914,468	792,420	6,452,508	3,776,668	4,178,052	1,168,972
Design first mode natural frequency of bridges[a], Hz	1.58	1.12	1.52	0.95	1.58	1.12	1.52	0.95
New first mode natural frequency of rigidized bridges, Hz	1.74	1.27	1.66	1.01	1.79	1.41	1.83	1.11

[a]Values from Table 1.

[b]Based on bridges S-C and S-O having a design stress of 27,000 psi and bridges NS-C and NS-O having a design stress of 55,000 psi.

equals the previous weight of the bridge plus the weight of the added steel. These new weights and stiffnesses are also given in Table 3. The stress increase in the existing flanges due to the added weight is calculated on the basis that the added weight of steel is a uniformly distributed dead load added to the bridge. The assumption was also made that all the steel is first clamped in place and then welded. The stress increases are given in Table 3.

Of the 2 rigidization treatments chosen for each bridge, the lower values (25 percent reduction for the concrete deck bridges and 26 percent for the orthotropic deck bridges) are considered to be feasible. The other 4 rigidization treatments are considered to be somewhat impractical because of the large amount of steel required and the high stress levels brought about in the existing flanges by the added weight. Rigidization treatments based on higher values of percentage of live load reduction also require that steel be welded to the top flanges, which is considered more difficult to perform in the field. They are included, however, to show an extreme of what could be achieved with rigidization.

Damping

One of the methods selected as a treatment to reduce dynamic bridge motion is the addition of damping to the bridge. The amount of damping present in the untreated bridges is designated in terms of the loss factor, defined as the log decrement divided

TABLE 4
WEIGHT LIMITATIONS ESTABLISHED FOR DAMPING TREATMENTS

Bridge	3.7 Percent Stress Increase at Midspan			7.4 Percent Stress Increase at Midspan		
	Design Stress (psi)	Stress Increase Due to Weight of Damping (psi)	Uniformly Distributed Load (lb/ft)	Design Stress (psi)	Stress Increase Due to Weight of Damping (psi)	Uniformly Distributed Load (lb/ft)
S-C	27,000	1,000	473	27,000	2,000	946
NS-C	55,000	2,000	511	55,000	4,000	1,022
S-O	27,000	1,000	284	27,000	2,000	568
NS-O	55,000	2,000	279	55,000	4,000	558

by π. All bridges are considered to have an inherent loss factor of 0.02. When a damping treatment is added to a bridge, the total loss factor is then the loss factor associated with the treatment plus 0.02.

The addition of a damping treatment to a bridge structure increases the midspan dead load stress. Therefore, the total loss factor that can be achieved for a given bridge is dependent on the weight of treatment that can be added without exceeding allowable stresses.

Two limits were established for the midspan dead load stress increase. The first limit involved a stress increase of 3.7 percent of the design stress; the second limit involved a stress increase of 7.4 percent of the design stress. The 3.7 percent limit implies a midspan stress increase of 1,000 psi in bridges S-C and S-O, which have a design stress of 27,000 psi, and a 2,000 psi stress increase in bridges NS-C and NS-O, which have a design stress of 55,000 psi. The 7.4 percent limit implies a midspan stress increase of 2,000 psi in bridges S-C and S-O and a 4,000 psi increase in bridges NS-C and NS-O. The corresponding maximum uniformly distributed loads for all these conditions are given in Table 4. The 2 stress limits for each bridge imply that 2 values of loss factor will be obtained for each bridge.

Several damping mechanisms were evaluated and "multiple-band" damping was selected for all cases in order to provide a maximum value of total bridge loss factor consistent with the limits in stress due to weight of the added material. The treatment, shown in Figure 4, consists of an alternate series of metal bands and viscoelastic material thicknesses. The metal bands are periodically attached to the primary structure to be damped. Relative motion between 2 attachment points induces shear strains in the viscoelastic material via the metal bands.

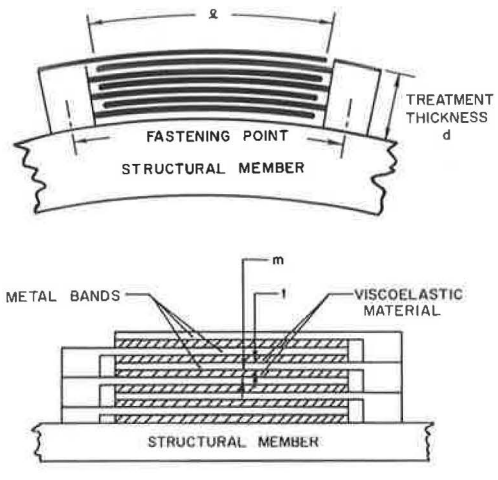

Figure 4. Schematic representation of multiple-band damping treatment.

The viscoelastic material was selected on the basis of providing an optimum peak loss factor when its properties were determined at a frequency of 1.0 Hz and a temperature of 77 F. The change of properties with frequency for a viscoelastic material implies that the loss factor of the bridge will be approximately a maximum for the first mode of vibration and will decrease with higher modes. The width of each damper is approximately 11 ft, and 3 dampers are installed side by side to cover the full width of the bridge (33 ft). The total length of the damping treatment is 250 ft. The viscoelastic material is cemented to the steel bands. In the installation, a typical 4-ft long unit is lifted into place, and the viscoelastic material and contact cement are applied to attach the unit to the previous unit placed before it. Concurrently, fasteners are welded to the bottom flanges.

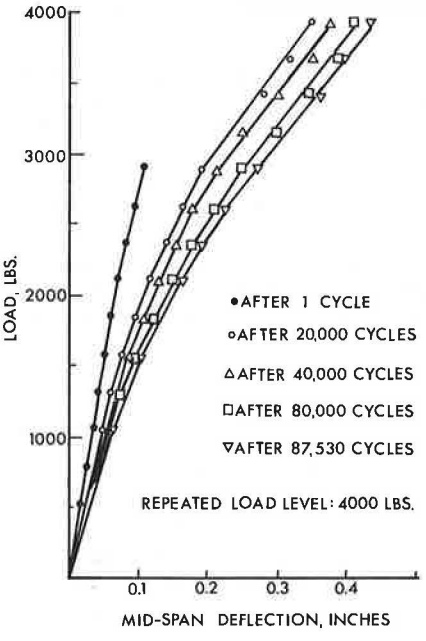

Figure 5. Load-deflection characteristics of specimen D-4 during course of repeated loading test RL-2.

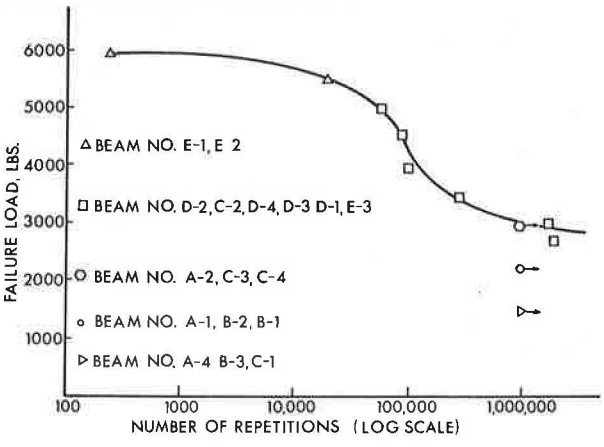

Figure 6. Repeated loading test results.

load deflection curves from intermediate static tests is shown in Figure 5. It is quite clear that there was a gradual reduction in beam stiffness as the number of load applications increased.

Figure 6 shows the results of the repeated load tests in which the peak magnitude of the repeated load is plotted as a function of the number of cycles of loading at which failure occurred. The L-N curve is characteristically Z-shaped with the upper end approaching asymptotically the static ultimate load and the lower end approaching asymptotically the load level of 2,500 lb, which corresponds to approximately 80 percent of the calculated cracking load for the tension element.

CONCLUSIONS

The following conclusions may be drawn on the basis of this investigation.

1. Over the upper range of loads from 1.7 to 2.0 P_{cr}, failure resulted from fatigue of concrete well before 1 million cycles, indicating a low fatigue life.
2. A typical curve of repeated load versus number of cycles of loading corresponding to fatigue failure (on semilog scale) consists of a central segment from P_{cr} to 1.7 P_{cr} that has a steep slope and represents the loading range over which failures resulted from fatigue of prestressing steel after a load application of less than 1 million cycles.
3. Over the range of load less than 0.7 P_{cr} (or approximately 0.3 P_u), the composite beam sustained repeated load application of well over 1 million cycles without fatigue failure.
4. The tests substantiated previous investigations that failure by fatigue before 1 million cycles of load is unlikely when the magnitude of the repeated load does not exceed the cracking load of the prestressed element.
5. The use of such a tension element for continuity reinforcement creates a section that is superior to mild steel reinforcement because it increases the cracking load of the section by 52 percent and, thus, provides better protection of the reinforcement against corrosion.
6. The loss of stiffness of the composite member, as measured by the deflections, was dependent on the magnitude of the repeated load. In general, the higher the magnitude of the repeated load is, the greater the rate of progressive loss of stiffness will

be. When the magnitude of the repeated load is less than the cracking load, stiffness loss is negligible.

7. A gradual loss in stiffness was definitely detected with the application of repeated loads of magnitude in excess of the cracking load. This is probably due to the progression of cracks deeper and deeper into the section and also due to some deterioration in concrete strength.

8. Because the progressive loss of stiffness is usually a signal that cracking is gradually advancing into the section, it is also a positive signal that failure due to fatigue before 1 million cycles of load is highly probable.

9. The loss of stiffness after initial cracking of the composite section was much smaller than expected. This further reinforces the belief that cracks may be prevented from advancing deeper into the section by the restraining effect of the tension element.

ACKNOWLEDGMENT

This paper is based on a research project conducted through the Highway Research Program in the Department of Civil Engineering at North Carolina State University (6). The project was sponsored by the North Carolina State Highway Commission and the Federal Highway Administration. Gratitude is expressed to E. G. Kandasamy for assistance in conducting the testing program and to Arnold Stone Company, Greensboro, North Carolina, for manufacture and supply of the prestressed tension elements.

REFERENCES

1. Evans, R. H., and Parker, A. S. Behavior of Prestressed Concrete Composite Beams. ACI Jour., Proc. Vol. 51, May 1955, pp. 861-878.
2. Evans, R. H., and Kong, F. K. The Extensibility and Microcracking of the Insitu Concrete in Composite Prestressed Concrete Beams. Structural Engineer, Vol. 42, June 1964.
3. Burns, N. H. Development of Continuity Between Precast Prestressed Concrete Beams. Jour. of Prestressed Concrete Institute, Vol. 2, No. 3, June 1966.
4. Hanson, N. W. Prestressed Concrete Prisms as Reinforcement for Crack Control. Jour. of Prestressed Concrete Institute, Vol. 14, No. 5, Oct. 1969, pp. 14-31.
5. Bishara, A., and Almeida, F. N. Concrete Beams With Prestressed Reinforcement. Jour. of Struct. Div., Proc. ASCE, Vol. 96, No. ST7, July 1970, pp. 1445-1460.
6. Mirza, J. F., Zia, P., and Bhargava, J. R. Static and Fatigue Strengths of Beams Containing Prestressed Concrete Tension Elements. North Carolina State University, Raleigh, final report.

Steel was selected as the material for the metal bands because it yielded values of loss factors slightly higher than those yielded by aluminum when the weight limitations were considered. The steel selected is COR-TEN "A", provided by U.S. Steel, which resists progressive rusting. The steel band thicknesses are in commercially available gage thicknesses.

Passive Absorber

The analysis of the passive absorber considers a rigid mass attached to the midspan of the bridge by a linear spring with viscous damper in parallel.

It is desirable to have the absorber mass, M_a, as large as possible so that forces acting on it (and hence on the bridge) are large enough to effectively reduce bridge vibrations without resulting in large absorber deflections. However, because the bridge structure must support the absorber mass, consideration must be given to the increase in bridge stress due to the added absorber weight. Therefore, in all cases, the absorber mass was selected so that its static weight caused an increase in stress no greater than 4 percent of the design stress. The actual increase in stress was 1,000 psi for bridges S-C and S-O and 2,000 psi for bridges NS-C and NS-O. The selected values of the absorber weights are 59, 64, 35.5, and 35 kips for bridges S-C, NS-C, S-O, and NS-O respectively.

Two other parameters need to be chosen to describe the characteristics of the passive absorber: stiffness of the spring, K_a, and the damping coefficient, C_a. Values for these parameters are selected indirectly by defining the undamped natural frequency as

$$f_a = \tfrac{1}{2}\pi \sqrt{K_a/M_a} \tag{4}$$

and the viscous damping ratio as

$$\zeta_a = \frac{C_a}{2\sqrt{K_a M_a}} \tag{5}$$

In all cases, the undamped natural frequency, f_a, was set equal to the first mode bridge frequency. The viscous damping ratio, ζ_a, was chosen by considering values of DI_{max} and DI_{rms} where ζ_a had values ranging from 0 to 0.5. A consideration of these results and the practicality of obtaining damping (i.e., it is quite common to have viscous damping ratios of 0.1 or less but rather difficult to obtain values greater than 0.1) led to a selection of a viscous damping ratio of $\zeta_a = 0.1$ for all cases.

The 3 elements that make up the passive absorber are the rigid mass, the linear spring, and the viscous damper. The rigid mass is simply composed of a block (or blocks) of concrete of proper size to make up the required mass. The linear spring is made from elastomeric material. One of the advantages of using elastomeric materials in the design of spring elements is their inherent damping capacity that ranges from $\zeta = 0.05$ to 0.1, depending on the material. If steel springs are used to generate the required stiffness values, additional damping devices would be needed to provide the necessary values of damping. Figure 5 shows the manner in which the elastomeric spring elements could be used in this application.

Becasue of molding limitations, the thickness of each pad is restricted to 3 in. Therefore, steel plates are bonded to each side of the pads, and the plates are bolted together for assembly. The total weight of the absorber and the corresponding stress increase at midspan are given in Table 5.

Active Absorber

The analysis of the active absorber assumes that a rigid mass is attached to the midspan of the bridge by an actuator capable of applying a force to the absorber (and hence an equal but opposite force to the bridge at midspan) according to the following equation:

$$M_a\ddot{u}(s) = \left(\frac{s}{s+\omega_H}\right)^3 \left(\frac{\omega_c}{s+\omega_c}\right) G_v \dot{y}_m(s) + \left(G_{rv}s + G_{rd}\right)\left\{\left[y_m(s) - u(s)\right]\right\} \qquad (6)$$

where

M_a = mass of the absorber, lb-sec^2/in.;

$\ddot{u}(s)$ = $\mathcal{L}[\ddot{u}]$ (Laplace transform of the absorber acceleration), in./sec;

s = Laplace transform variable, 1/sec;

ω_H = lead function cutoff frequency, rad/sec;

ω_c = lag function cutoff frequency, rad/sec;

G_v = midspan velocity gain, lb-sec/in.;

$\dot{y}_m(s)$ = $\mathcal{L}[\dot{y}_m]$ (Laplace transform of the bridge midspan velocity), in.;

G_{rv} = relative velocity gain, lb-sec/in.;

G_{rd} = relative displacement gain, lb/in.;

$y_m(s)$ = Laplace transform of bridge midspan displacement, in.-sec; and

$u(s)$ = Laplace transform of absorber displacement, in.-sec.

Values of the active absorber mass for each bridge were selected in a manner similar to that used for the passive absorber; namely, an increase in bridge stress no

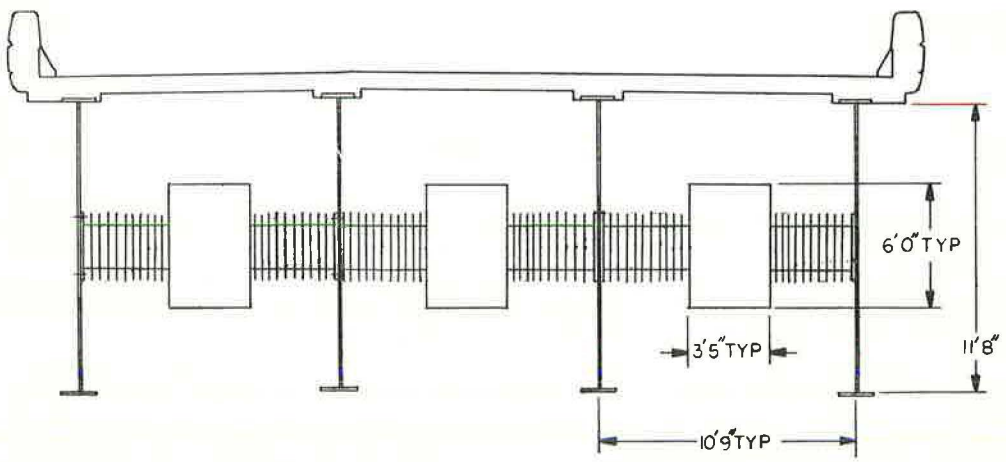

Figure 5. Typical passive absorber installation on bridge S-C.

TABLE 5

STRESS INCREASE DUE TO ADDING PASSIVE ABSORBER TO BRIDGE AT MIDSPAN

Bridge	Weight of Inertia Block (kip)	Weight of Steel (kip)	Weight of Rubber (kip)	Total Weight (kip)	Stress Increase on Lower Flange at Midspan	
					psi	Percent of Design Stress
S-C	59	13.63	5.49	78.12	1,323	4.9
NS-C	64	20.95	11.77	96.72	3,020	5.5
S-O	35.5	10.25	3.61	49.36	1,391	5.2
NS-O	35	17.28	9.10	61.38	3,505	6.4

greater than 4 percent of the design stress. The actual increase in stress was 1,000 psi for bridges S-C and S-O and 2,000 psi for bridges NS-C and NS-O. The selected values of the active absorber weights for each bridge are given in Table 6.

The active absorber acts essentially as a damper at the bridge midspan (i.e., it applies a force on the bridge, proportional but opposite in sign to the bridge midspan velocity). The gain, G_V, is essentially the damping coefficient. The 3 lead functions are used to attenuate low frequency components in order to avoid large deflections of the absorber. The lag function is used for stability. The relative velocity and displacement gain are used to position the absorber relative to the bridge. The values of the parameters selected for each of the 4 bridges are given in Table 6.

Because of the large masses and forces that are involved in the design of the active system, it was concluded that an electrohydraulic system could best meet the requirements of system response. Hydraulic systems are inherently among the stiffest systems available to the designer and can respond quickly and accurately to command signals.

The force acting on the absorber and, hence, on the bridge is applied by means of a hydraulic actuator connecting the absorber to the bridge. The actuator must put out a force according to Eq. 6. The oil in the actuator is assumed to be incompressible. Therefore, the flow of oil into the actuator is given by

$$Q(s) = A[\dot{u}(s) - \dot{y}_m(s)] \tag{7}$$

where Q is the flow of oil, $in.^3/sec$, and A is the piston area, $in.^2$. Combining Eqs. 6 and 7 results in an equation for the flow that will ensure that the desired force equation is satisfied. The flow can be written as a function of the bridge midspan acceleration and the relative deflection between the bridge and the absorber multiplied by shaping functions. The acceleration and relative deflection are measured with electronic transducers. These signals are fed to a servoamplifier that applies the shaping functions and puts out a signal proportional to the desired flow. The flow is delivered to the actuator by means of a hydraulic power supply and servovalve.

It is impractical to have the actuator support the weight of the absorber. Therefore, a very soft supporting spring will also connect the absorber to the bridge. Figure 6 shows a schematic representation of the active system installation.

COMPARISON OF TREATMENT EFFECTIVENESS

This section presents a comparison of the various treatments and an evaluation of the degree of bridge vibration control that can be attained with each. Performance effectiveness is calculated for the 2 rigidization treatments, the 2 damping treatments, the passive absorber, and the active absorber for each bridge and roadway condition based on the maximum and rms values of dynamic increment. In addition, a cost effectiveness comparison is made based on values of dynamic increment and cost estimates for each treatment. The solution of the equations of motion and method of calculation are given in another report (1).

Although the vehicle travels across the span, 2 roadway conditions and 2 response criteria, DI_{max} and DI_{rms}, can be considered to evaluate the effectiveness of each treatment in reducing bridge vibrations. Average values were calculated for each of

TABLE 6

PARAMETER VALUES FOR THE ACTIVE ABSORBER

Bridge	W_a (lb)	ω_H (rad/sec)	ω_c (rad/sec)	G_V (lb-sec/in.)	G_{rv} (lb-sec/in.)	G_{rd} (lb/in.)
S-C	59,000	2.48	9.92	33,400	1,340	58.7
NS-C	64,000	1.76	7.03	15,100	1,030	32.0
S-O	35,500	2.38	9.54	17,500	777	32.7
NS-O	35,000	1.49	5.96	4,840	478	12.6

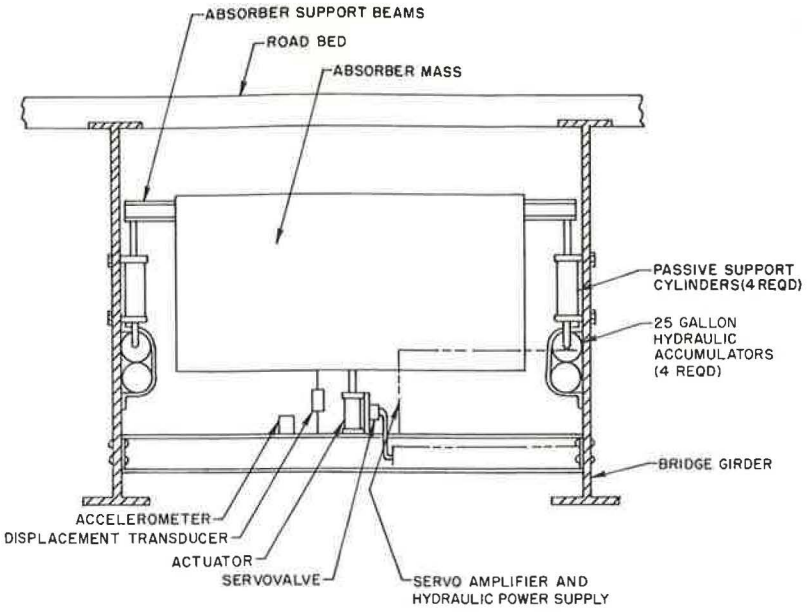

Figure 6. Schematic representation of active system installation.

the 3 vehicle velocities and the 3 vehicle types. From these data, percentage reductions were calculated comparing the treated to the untreated bridge response. These results are shown in Figures 7 through 10 for bridges S-C, NS-C, S-O, and NS-O respectively.

Performance Effectiveness Comparison

The results shown in Figures 7 through 10 indicate that, with a few minor exceptions, there is a reasonably good correlation between the 2 criteria involving the actual

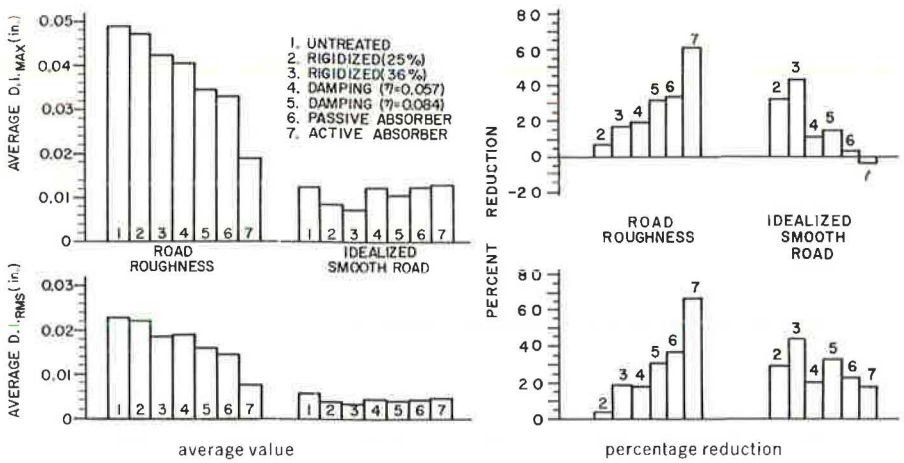

Figure 7. DI_{max} and DI_{rms} for all treatments on bridge S-C.

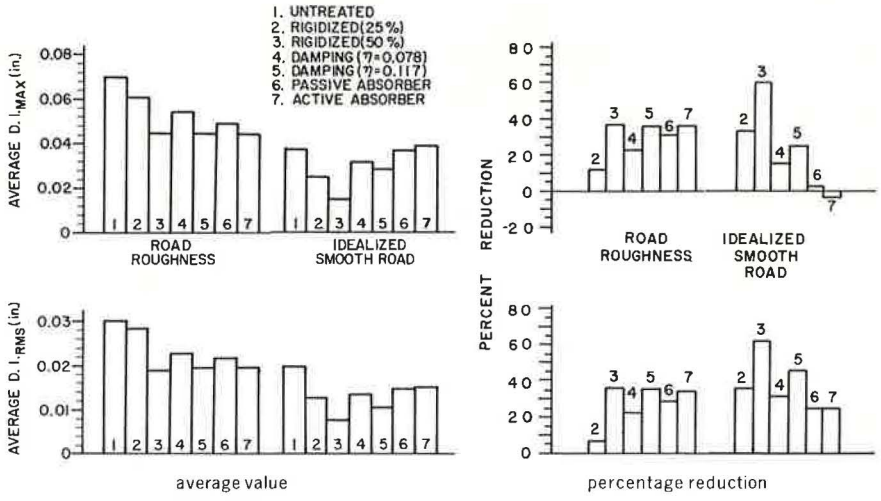

Figure 8. DI_{max} and DI_{rms} for all treatments on bridge NS-C.

values of DI_{max} and DI_{rms}. These results are presented only to show the levels of midspan response with and without treatments for a particular bridge, roadway condition, and criterion. The comparison of the performance effectiveness of the various treatments is done on the basis of the percentage reduction in the response of each treatment. For each bridge type, percentage reductions are indicated for all treatments, roadway conditions, and criteria (DI_{max} and DI_{rms}). The percentage reductions based on the 2 different criteria correlate reasonably well. Values of DI_{rms} can, in a sense, be thought of as an indication of the "average" dynamic increment occurring throughout the entire travel of the vehicle along the span. Therefore, the average percentage reduction of the rms of the dynamic increment is used as a basis for comparing the performance effectiveness among treatments.

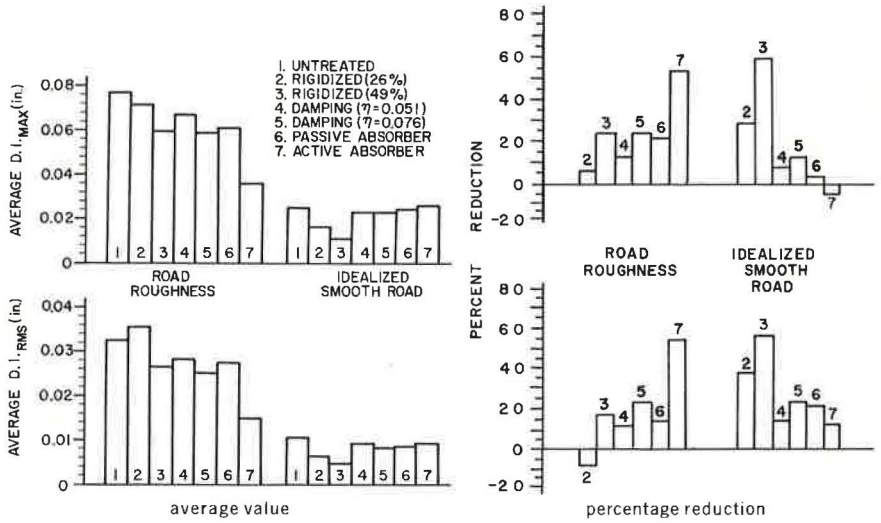

Figure 9. DI_{max} and DI_{rms} for all treatments on bridge S-O.

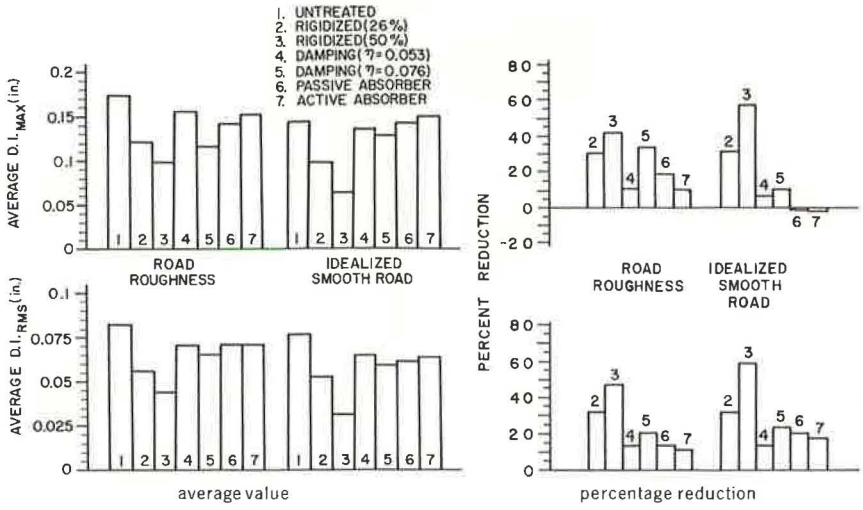

Figure 10. DI_{max} and DI_{rms} for all treatments on bridge NS-O.

Figures 7 through 10 show that the treatment offering the greatest performance effectiveness (or percentage reduction) differs depending on the roadway condition and bridge. As previously mentioned, the idealized smooth road condition is physically unrealizable. Bridge motions resulting from it can help in defining what portion of the total response under the road roughness condition is due to the vehicle weight.

For bridge S-C under the road roughness condition, the active absorber is most effective and the passive absorber is next best. Under the idealized smooth road condition, the high value of rigidization is best. For bridge NS-C under the road roughness condition, the high value of damping, the high value of rigidization, and the active absorber provide approximately the same percentage reduction. For the idealized smooth road condition, the high value of rigidization is the most effective. For bridge S-O under the road roughness condition, the active absorber is best; while for the idealized smooth road condition, the high value of rigidization is most effective. For bridge NS-O, the high value of rigidization provides the largest percentage reduction under both roadway conditions.

In one case under the road roughness condition (bridge S-O, low value of rigidization, Fig. 7), the interaction between the vehicle and bridge frequencies, together with the particular frequency content of the road profile, resulted in an increase in the motion of the treated bridge when compared to the untreated one (negative value of percentage reduction of DI_{rms}). In this instance, the oscillations due to deck irregularities are in phase with the motions induced by the vehicle weight.

Cost Effectiveness Comparison

In addition to the treatment performance effectiveness, an important consideration in choosing a treatment is its cost. The estimated cost of each treatment is given in Table 7. For purposes of comparison, the estimated cost of steel in the untreated bridges is also shown. The determination of the treatment that gave the highest cost effectiveness was made by dividing the values of percentage reduction for the rms of the dynamic increment for each treatment by the cost of each particular treatment. The number so calculated for cost effectiveness was multiplied by 10^5 to obtain reasonable values of a cost effectiveness index. Values of the cost effectiveness index for all treatments, bridges, and roadway conditions are shown in Figures 11 and 12 for the road roughness and idealized smooth road conditions respectively.

TABLE 7

ESTIMATED COST OF TREATMENTS

Bridge	Untreated (steel cost only)	Rigidized		Damping		Absorber	
		Low	High	Low	High	Passive	Active
S-C	$172,440	$59,400	$138,000	$54,914	$73,941	$23,000	$105,000
NS-C	142,520	52,300	185,400	55,930	71,955	36,000	110,000
S-O	168,810	52,200	123,000	43,013	64,058	18,000	99,000
NS-O	102,460	57,600	142,140	43,013	57,000	30,000	102,000

BRIDGE TYPE	S-C	NS-C	S-O	NS-O
2. RIGIDIZED	25%	25%	26%	26%
3. RIGIDIZED	36%	50%	49%	50%
4. DAMPING η=	0.057	0.078	0.051	0.053
5. DAMPING η=	0.084	0.117	0.076	0.076
6. PASSIVE ABSORBER				
7. ACTIVE ABSORBER				

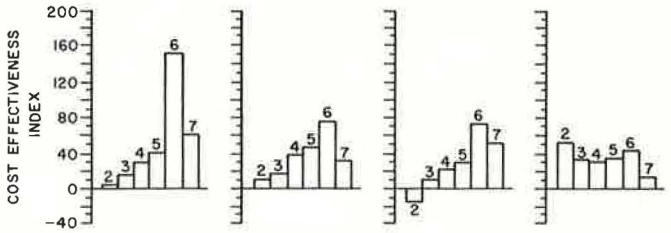

Figure 11. Cost effectiveness for all treatments and bridges based on bridge response to road roughness condition.

BRIDGE TYPE	S-C	NS-C	S-O	NS-O
2. RIGIDIZED	25%	25%	26%	26%
3. RIGIDIZED	36%	50%	49%	50%
4. DAMPING η=	0.057	0.078	0.051	0.053
5. DAMPING η=	0.084	0.117	0.076	0.076
6. PASSIVE ABSORBER				
7. ACTIVE ABSORBER				

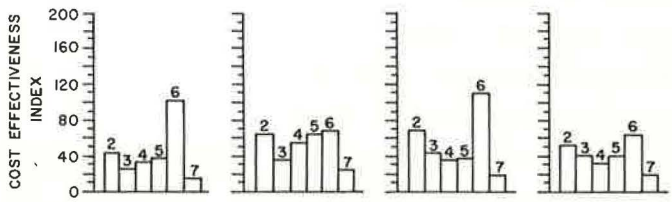

Figure 12. Cost effectiveness for all treatments and bridges based on bridge response to idealized smooth road condition.

Figure 11 shows that, for the road roughness condition, the passive absorber yields the highest cost effectiveness on bridges S-C, NS-C, and S-O. On bridge NS-O, the low value of rigidization provides the highest cost effectiveness. Figure 12 shows that, for the idealized smooth road condition, the passive absorber yields the highest values of cost effectiveness for all bridges.

Care should be exercised in using the cost effectiveness indexes to reach conclusions regarding any of the treatments. For example, the high values of cost effectiveness indicated for the passive absorber are due mainly to its low cost and not to its high performance effectiveness. Also, it must be realized that the cost figures are only estimates and would not necessarily apply to any particular bridge.

CHOICE OF TREATMENT

A decision as to which type of treatment to use based on the reduction in DI_{rms} would have to consider the type of bridge and the nature of the roadway. This study has dealt with 4 specific bridge designs and 2 roadway conditions, one of which (idealized smooth road) cannot be attained in practice because it assumes a mathematically or ideally smooth roadway on the bridge. It would seem reasonable to base the choice of treatment on the road roughness condition. However, it must be emphasized that an infinite variety of road roughness conditions actually exist in the field, that are greater or lesser in magnitude than the one chosen in this study. In addition, actual roadways may have a significantly different frequency content. If the roughness of the actual roadway is not severe, the results based on the idealized smooth road condition could be used to select the suitable treatment. On the other hand, the field roadway profile may be worse than the road roughness selected for this study. Such a case does not necessarily imply that the actual bridge roadway would be visually rougher, but rather that some characteristics of the spatial frequency content of the actual road may result in a different level of treatment effectiveness than those shown here. Therefore, in order to select an appropriate treatment based on the results presented here, it is necessary to determine which of the 2 roadway conditions is more representative of the response of a particular bridge.

The magnitude and characteristics of the bridge response to the idealized roadway condition can be shown to be closely approximated by the first mode response occurring when the vehicle is replaced by a traveling force of constant magnitude whose value is the weight of the vehicle. An approximate expression for the first mode dynamic increment of a uniform beam under a moving force of constant magnitude is given as follows (3):

$$DI = \alpha Y_{st} e^{-\pi \eta_1 f_1 t} \sin 2\pi f_1 t \qquad (8)$$

where

α = speed parameter, $(V/2\ell)/f_1$;

Y_{st} = midspan static deflection, $F\ell^3/48EI$;

V = velocity of moving force;

ℓ = length of span;

F = magnitude of concentrated force at midspan;

EI = flexural stiffness of span;

f_1 = first mode frequency of span; and

η_1 = loss factor of span for first mode.

According to Eq. 8, (a) the maximum dynamic increment due to a moving force of constant magnitude always occurs at the first quarter-cycle of bridge motion or when the force has just entered the span; (b) the dynamic increment decreases exponentially because of damping in the span; (c) the maximum dynamic increment is directly proportional to both the speed and the magnitude of the moving force; and (d) the frequency of oscillation of the dynamic increment is the first mode frequency of the bridge.

For the low values of loss factor assumed for the untreated bridges ($\eta_1 = 0.02$), the maximum dynamic increment for a moving force may be closely approximated by

$$DI_{max} = \alpha Y_{st} \tag{9}$$

Values of maximum dynamic increment were calculated by using Eq. 9 for all vehicle speeds, force, and bridge frequencies. Good correlation was found between the calculated values based on a moving force and the corresponding computed values for the vehicle traversing the idealized smooth road.

The expression for the rms of the dynamic increment for a moving force is given by

$$DI_{rms} = \sqrt{1/T \int_0^T (DI)^2 dt}$$

$$= \alpha Y_{st} \sqrt{1/T \int_0^T e^{-2\pi\eta_1 f_1 t} \sin^2 2\pi f_1 t \, dt} \tag{10}$$

where $T = \ell/V$.

Values of the rms of the dynamic increment were calculated by using Eq. 10 for all values of speed, force, and bridge frequencies. The correlation is good, although not quite as good as was the case for the values of maximum dynamic increments. The values of the rms of the dynamic increment computed for the vehicle traversing the idealized smooth road are slightly lower than the values calculated by using Eq. 10. This is considered to be due to the vehicle acting as a vibration absorber as it undergoes a small amount of springing.

For the long-span bridges considered in this study, the parameter αY_{st} provides a measure of the level of dynamic increment that will occur for the idealized smooth road condition for a given vehicle and speed. The actual dynamic increment may be different from that indicated by this parameter because of the fact that bridge approach and deck roadways are never ideally smooth. Road roughness or bumps will induce additional oscillations, and this dynamic motion may reinforce or cancel the response under the idealized smooth road condition because of the weight of the vehicle alone. Nevertheless, the calculation of the level of idealized smooth road response by the use of the parameter αY_{st} is considered worthwhile. The actual level of dynamic motion indicated by field tests, when compared to αY_{st}, would provide an indication of the effect that roadway roughness has on the total dynamic motion. If, for a statistically significant number of field tests, the actual dynamic motion is much greater than that indicated by αY_{st}, then a treatment can be selected based on the results for the road roughness condition. If, however, the actual dynamic motions for a sufficient number of test vehicle runs are of the order of magnitude that would be predicted by the use of αY_{st}, then treatments of choice would be as indicated under the idealized smooth road condition.

CONCLUSIONS

Based on the results presented in this report, the following conclusions can be made:

1. The large dynamic motions associated with bridges employing higher strength steels can be reduced to the levels associated with bridges employing low-alloy steels by means of appropriate treatments.
2. A technique is provided to select vibration control treatments, which on the average reduce the midspan dynamic motions of long-span bridges from 20 to 40 percent when compared to the untreated bridges. However, care must be exercised in selecting appropriate treatments because no single treatment was found equally effective for all cases considered. Also, the analysis indicates that, depending on the character-

istics of deck irregularities, use of a treatment may actually result in a larger bridge response for certain combinations of vehicle speed and weight.

3. Different values of treatment effectiveness were obtained contingent on whether the bridge deck is considered to be mathematically smooth (idealized smooth condition) or to have an irregular pavement (road roughness condition). A parameter can be calculated to approximate for the untreated bridge the level of dynamic increment that will occur under the idealized smooth road condition (constant traveling force). A comparison between calculated and measured values of this parameter can define whether results based on this condition can be used to select the most effective treatment for vibration control.

4. If field measurements of the untreated bridge indicate that the dynamic motions are primarily due to the constant traveling force, then reducing the rms level of road profile will have very little effect on the bridge dynamic motions.

5. The choice of the treatment to be applied to a bridge whose dynamic motion is unsatisfactory must be based not only on the particular bridge properties but also on the nature of the roadway. Specifically, some measure must be obtained as to the degree of influence that the level of road roughness exerts on the total dynamic response. In addition, the choice of a treatment must consider the actual amount of reduction achievable with that treatment, its cost, and whether that level of reduction is sufficient.

ACKNOWLEDGMENT

This paper is based on results of an investigation conducted under a contract with the Federal Highway Administration.

REFERENCES

1. DesMarais, D. A., Derby, T. F., and Calcattera, P. C. Feasibility Study of Methods, Materials and Devices for Controlling Bridge Vibrations. Barry Controls, Division of Barry Wright Corp., Watertown, Mass., final report, June 1970.
2. Whittemore, A. P., et al. Dynamic Pavement Loads of Heavy Highway Vehicles. NCHRP Rept. 105, Oct. 1970.
3. Inglis, C. E. A Mathematical Treatise on Vibrations in Railway Bridges. Cambridge Univ. Press, London, 1934.

DYNAMIC PROPERTIES OF SUSPENSION BRIDGES

V. R. McLamore and Ian R. Stubbs, Teledyne Geotronics, Long Beach, California; and Gary C. Hart, Mechanics and Structures Department, University of California, Los Angeles

Experimental determination of the natural frequencies of vibration, the vertical and torsional mode shapes, and the modal damping of the Newport Bridge, Rhode Island, and the William Preston Lane Memorial Bridge, Maryland, is briefly described. The results of the 2 measurements are compared to show fundamental similarities in their dynamic behavior. The similarities include the order that the types of motion of the deck occur. This order is as follows: symmetric vertical, antisymmetric vertical, antisymmetric vertical, symmetric vertical, symmetric vertical, symmetric torsional, and antisymmetric vertical. The ratios of higher order modal frequencies to the lowest modal frequencies are graphed. The mean ratios on the 2 bridges are found to agree within 10 percent. These factors may serve as useful rules of thumb during the design of suspension bridges.

•THE DYNAMIC behavior of bridge structures has been studied by engineers and scientists for many years. It is safe to say that, while techniques for studying dynamic response of structures have advanced rapidly during the past few decades, we are still a long way from a complete understanding of the behavior of these complex structures.

In developing new analytical techniques to model bridge structures more accurately, we must keep 2 very important points in mind.

1. The engineer seeks to create a mathematical or analytical model to describe a physical entity. Therefore, while advancements can be made following prescribed mathematical guidelines, the validity of the model depends on its verification with reality.
2. Engineering by its very history is a science that is based on experience. Often this means learning from experimental studies. The lessons learned from either full-scale or model studies are invaluable in expanding our experience. Therefore, it is this blend of theoretical development and implementation plus experimental testing that continual improves our method of bridge design.

The digital computer has made dynamic studies of structures economically feasible. Analyses using the natural modes of vibration have been used for simple structures such as high-rise buildings for some time. Similar techniques are now being used for the analysis of more complex structures such as suspension bridges. In high-rise buildings, simple rules of thumb have been developed to aid in determining the reasonableness of the analysis, for example, building period, in sec, 0.1 × number of floors; frame building, $f_n/f_1 = 1, 3, 5, 7$; and cantilever building, $f_n/f_1 = 1, 6.25, 17.5$.

This paper suggests that similar rules may be developed for bridges as more information on their dynamic properties becomes available. This suggestion is supported by summarizing the experimental results obtained during 2 recent full-scale studies to determine the dynamic properties of medium-sized suspension bridges and by showing how a comparison of the results may be used to establish some preliminary rules of thumb for this class of bridge.

Sponsored by Committee on Dynamics and Field Testing of Bridges and presented at the 50th Annual Meeting.

These preliminary guides should be helpful to design engineers during the early stages of a bridge design and serve as a qualitative check on the final design even though data from more bridges must be gathered and evaluated before rules that may be considered universal are developed.

DESCRIPTION OF BRIDGES

The Newport Bridge, which crosses the Narragansett Bay in Rhode Island, and the William Preston Lane Memorial Bridge, which crosses the Chesapeake Bay in Maryland, were studied. The Newport Bridge opened in June 1969. The William Preston Lane Memorial Bridge opened in 1952.

The suspended section of the Newport Bridge is 2,976 ft long, including a 1,600-ft main span, and two 688-ft side spans. The cables are 66 ft apart, and the roadway is 48 ft wide. The towers are 400 ft high. The roadway at the towers is approximately 218 ft above mean water level.

The suspended section of the William Preston Lane Memorial Bridge is 2,920 ft long, including a 1,600-ft main span and two 658-ft side spans. The distance between the cables is 39 ft, and the roadway is 28 ft wide. The towers are 354 ft tall. The roadway at the towers is approximately 194 ft above mean water level.

THE AMBIENT VIBRATION SURVEY

Ambient vibration surveys (AVS) were performed on the 2 suspension bridges in 1969. The details of these surveys can be found in other reports (1, 2, 3).

The main objective of the AVS of these bridges was to measure the natural frequencies and mode shapes of bridge deck vertical and torsional modes. In addition to this primary objective, the surveys also provided estimates of lateral deck natural frequencies of vibration.

The procedure used in the AVS of the bridge was to record on magnetic tape the motion sensed from an array of 7 seismometers. After a period of time, all but one of the seismometers were moved to different locations and data were again recorded. The seismometer that was not moved was used as a reference, and all data were normalized or compared to the reference. Five arrays were used to complete the survey. Figure 1 shows qualitatively the distribution of the seismometers in the arrays.

Traffic was moderate, and winds were generally light during the survey of the Newport Bridge. Traffic was heavy, and the wind varied from calm to strong (approximately 30 mph) during the survey of the William Preston Lane Memorial Bridge.

The recorded data were analyzed by using random vibration theory and power spectral density techniques. Other reports (3, 4, 5, 6) give more details on the statistical methods used to estimate the natural frequencies, modal damping coefficients, and mode shapes.

The analysis included generation of a graph of autopower spectral density of the motion at each instrument location and comparing the motion at each station to the motion at the reference station. The cross-spectral comparison yields graphs of the relative amplitudes and phase angles of the motion at the two points. Examples of the graphs are shown in Figures 2, 3, and 4 respectively. The locations on the bridge represented by the graphs are indicated in the lower left corners.

The damping values given in Tables 1 and 2 were obtained by using the "½ power point" method. The analysis procedure is described elsewhere (3).

BRIDGE CHARACTERISTICS

The dynamic behavior of both bridges included vertical, lateral, and twisting modes of vibration. The measurement plan was designed to obtain detailed information on the vertical and twisting modes only. The analyses were limited to investigation of frequencies less than 1 cycle per second. Table 1 gives the frequencies of vibration identified for the Newport Bridge and Table 2 gives similar information for the Memorial Bridge.

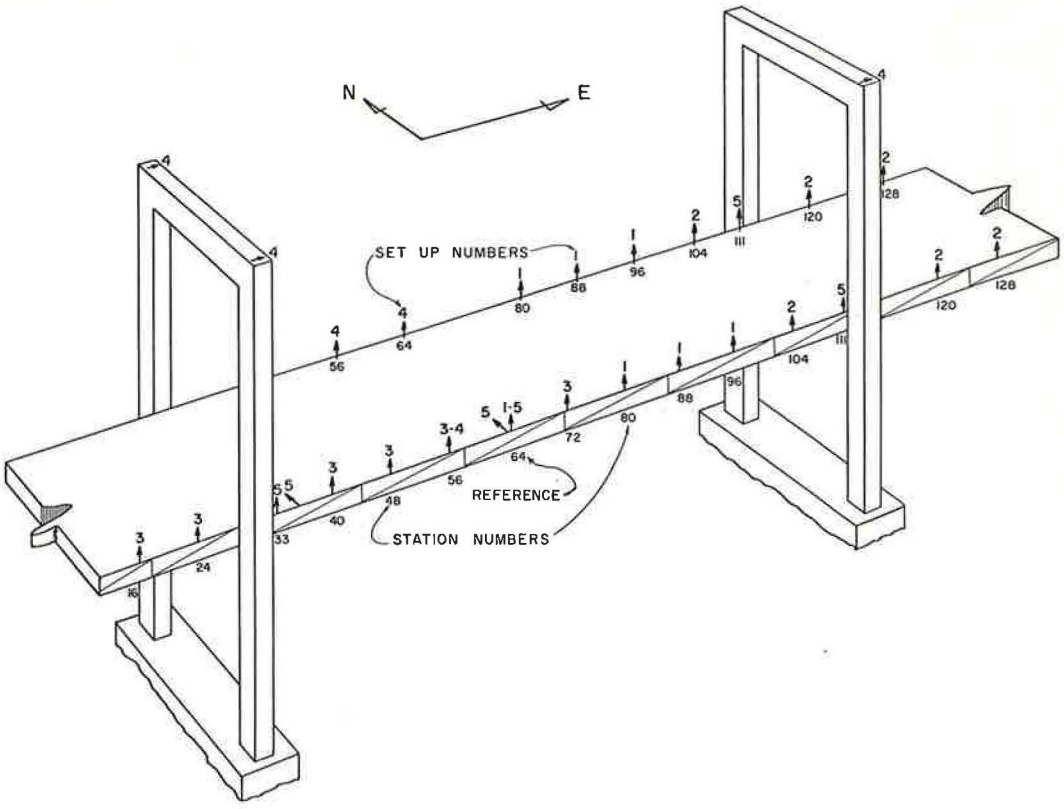

Figure 1. Instrument locations for ambient vibration surveys of bridges.

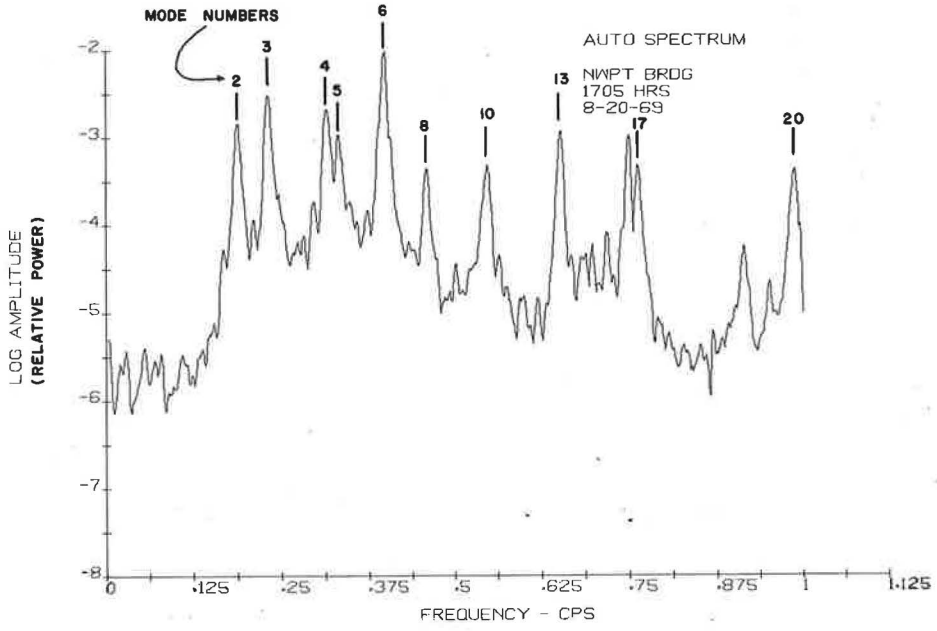

Figure 2. Power spectral density showing frequencies of vibration.

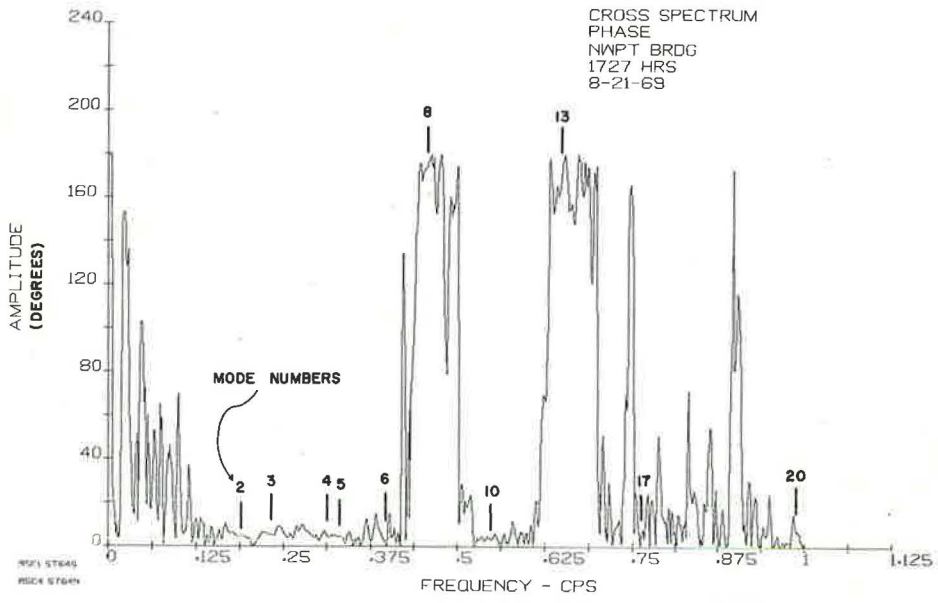

Figure 3. Relative phase angle between 2 seismometer locations.

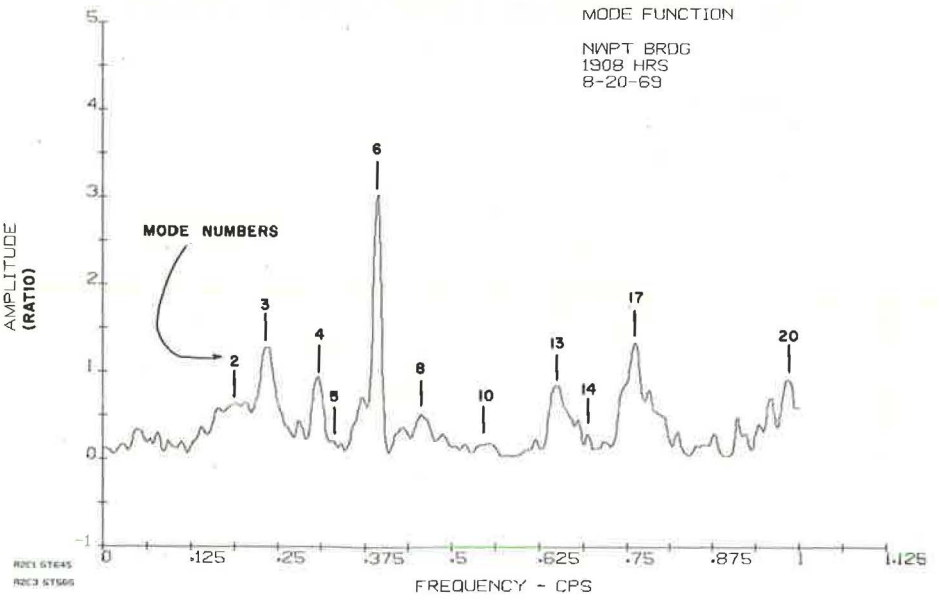

Figure 4. Relative amplitude between 2 seismometer locations.

TABLE 1

SUMMARY OF MODES OF VIBRATION FOR NEWPORT BRIDGE

Mode	Frequency (cpm)	Period (sec)	Damping		Classification
			Percent of Critical Damping	Logarithmic Decrement	
1	9.3	6.45	3.0	0.188	First lateral
2	11.1	5.42	2.0	0.126	First symmetric vertical
3	13.8	4.53	1.7	0.107	First antisymmetric vertical
4	18.7	3.2	2.0	0.126	Second antisymmetric vertical
5	20.0	3.00	1.1	0.069	Second symmetric vertical
6	23.6	2.54	1.1	0.069	Third symmetric vertical
7	25.2	2.38	1.1	0.069	Second lateral
8	27.3	2.20	0.8	0.050	First symmetric torsional
9	31.2	1.92	1.2	0.075	Third lateral
10	32.5	1.85	0.9	0.056	Third antisymmetric vertical
11	37.2	1.62	0.6	0.038	First longitudinal tower
12	38.4	1.56	0.5	0.031	Fourth lateral
13	39.0	1.54	0.8	0.051	First antisymmetric torsional
14	41.3	1.45	0.6	0.038	Fourth symmetric vertical (side spans)
15	42.3	1.42	0.6	0.038	Fifth lateral
16	44.8	1.34	0.5	0.031	Second longitudinal tower
17	45.3	1.32	0.8	0.050	Fifth symmetric vertical
18	48.4	1.24	0.8	0.050	Third longitudinal tower
19	49.2	1.22	0.9	0.056	Sixth lateral
20	59.6	1.006	0.4	0.025	Fourth antisymmetric vertical

TABLE 2

SUMMARY OF MODES OF VIBRATION FOR WILLIAM PRESTON LANE MEMORIAL BRIDGE

Mode	Frequency (cpm)	Period (sec)	Damping		Classification
			Percent of Critical Damping	Logarithmic Decrement	
1	6.3	9.52	5.4	0.339	First lateral
2	12.3	4.88	2.5	0.157	First symmetric vertical
3	15.6	3.85	2.2	0.138	First antisymmetric vertical
4	19.2	3.13	1.4	0.088	Second lateral
5	21.0	2.86	1.4	0.088	Second antisymmetric vertical
6	24.9	2.41	1.1	0.069	Second symmetric vertical
7	28.8	2.08	1.6	0.100	Third symmetric vertical
8	35.1	1.71	0.5	0.031	Third lateral
9	37.7	1.59	1.3	0.082	Fourth lateral
10	40.5	1.481	1.4	0.088	First symmetric torsional
11	44.4	1.351	0.9	0.057	Third antisymmetric vertical
12	51.9	1.16	0.9	0.057	Fifth lateral
13	55.9	1.07	0.4	0.025	Sixth lateral

In other reports (1, 2, 3), the mode shapes were drawn for each of the vertical and twisting modes of the decks. In order to assist in the physical understanding of the modal response of the bridges, Figure 5 shows the first symmetrical vertical and torsional mode shapes of the Newport Bridge. Figure 6 shows the first and third antisymmetrical vertical mode shapes of the Memorial Bridge.

COMPARISON OF RESULTS

Each bridge's vertical mode dynamic characteristics is presented in a form conducive to a comparative study of the 2 bridges. While such a comparison can be supported by using similarities in each bridge's ratio of center span length to side span length, it should be noted that the opening dates of these bridges were separated by nearly 20 years. Therefore, the main purpose of this section is to show the surprising similarity of the dynamic characteristics of these bridges in some important aspects.

Figures 7 and 8 show the first 7 vertical and torsional deck natural frequencies and mode shapes for the Newport Bridge and the Memorial Bridge respectively. The right

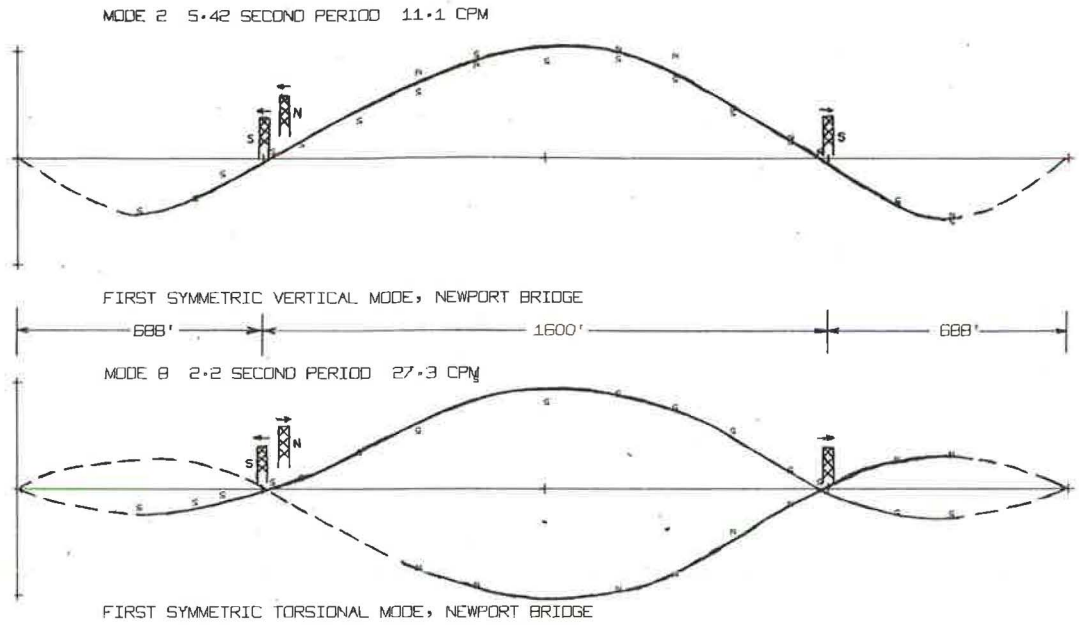

Figure 5. Symmetrical mode shapes of Newport Bridge.

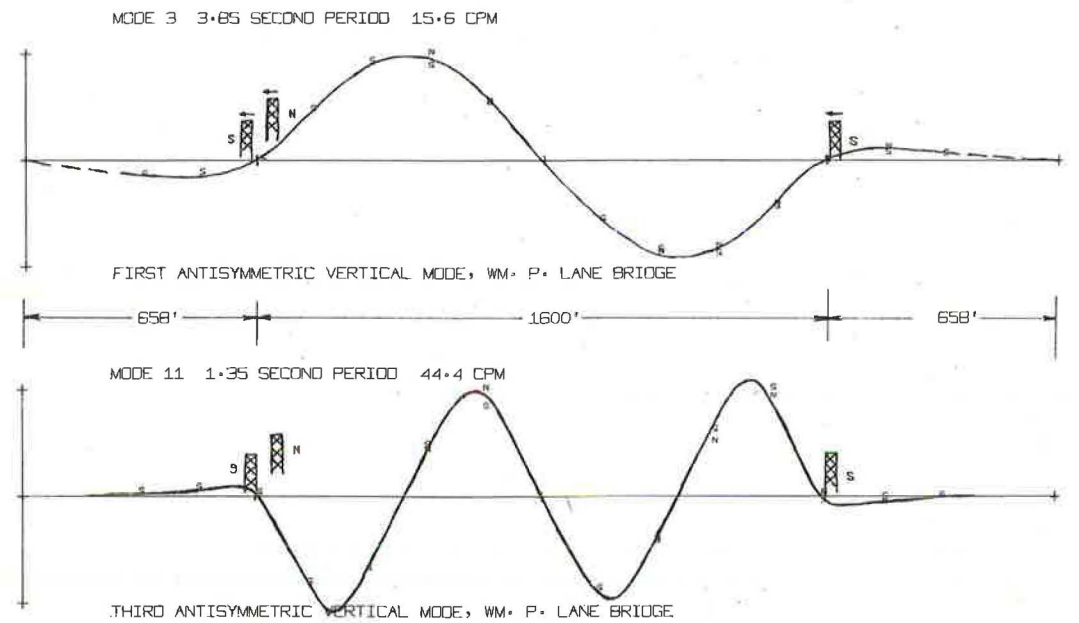

Figure 6. Antisymmetrical mode shapes of William Preston Lane Memorial Bridge.

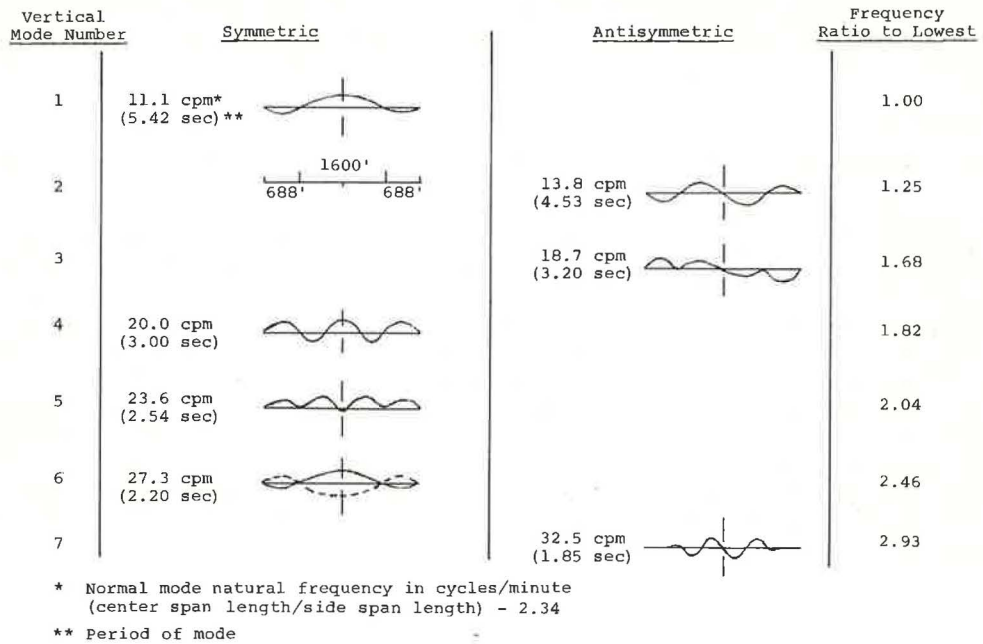

* Normal mode natural frequency in cycles/minute
(center span length/side span length) - 2.34

** Period of mode

Figure 7. Vertical mode shapes and natural frequencies of Newport Bridge.

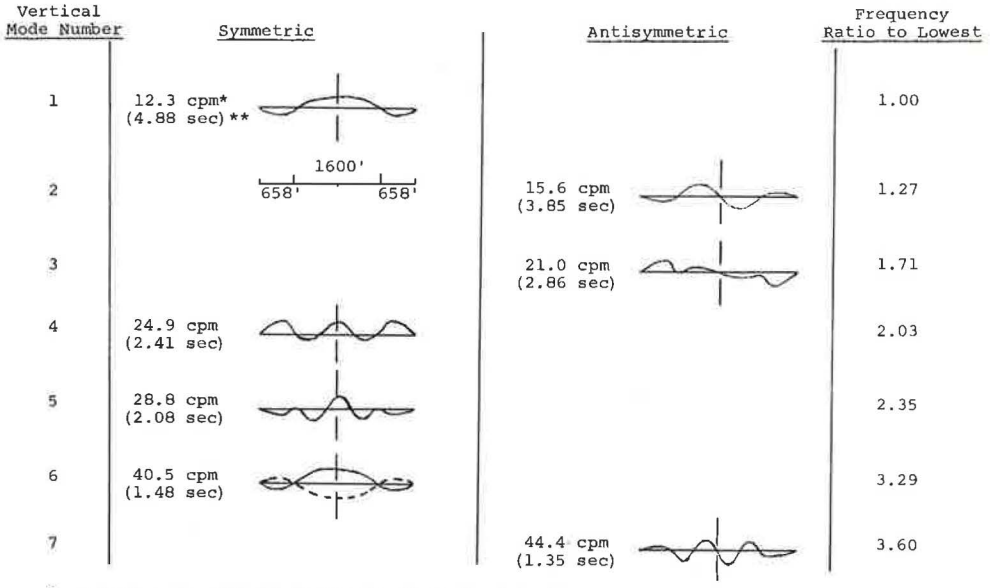

* Normal mode natural frequency in cycles/minute
(center span length/side span length) = 2.43

** Period of mode

Figure 8. Vertical mode shapes and natural frequencies of William Preston Lane Memorial Bridge.

column in each figure gives the ratio between the higher mode natural frequencies and the fundamental vertical natural frequency. These ratios are shown graphically in Figure 9a. The ratio between the higher symmetric and antisymmetric vertical frequencies and the lowest natural frequency in each of these categories is shown in Figure 9b and c.

A careful study of Figures 7, 8, and 9 shows the following:

1. Each bridge possesses the same sequencing of symmetric vertical, S; antisymmetric vertical, AS; and symmetric torsional, ST, mode shapes. This sequence is S, AS, AS, S, S, ST, and AS.
2. Figure 9a shows that the ratio between the higher order natural frequencies and the fundamental vertical natural frequency was nearly constant for both bridges. If the estimated mean (or average) ratios between the higher order and the fundamental vertical natural frequencies of 1.25, 1.70, 1.90, 2.20, 2.88, and 3.25 are used, then the percentage differences between these values and any one of those calculated are a minimum of 1.2 percent (third mode) and a maximum of 10.7 percent (seventh mode).
3. The ratio between each higher symmetric vertical frequency and the lowest symmetric vertical frequency is shown in Figure 9b. If mean ratio estimates of 1.90 and 2.20 are used, then these ratios differ from the original by 6.8 and 8.2 percent respectively. For the antisymmetric vertical frequencies, the corresponding mean ratios are 1.35 and 2.60. The percentage differences in these cases are 0.0 and 9.6 percent respectively.

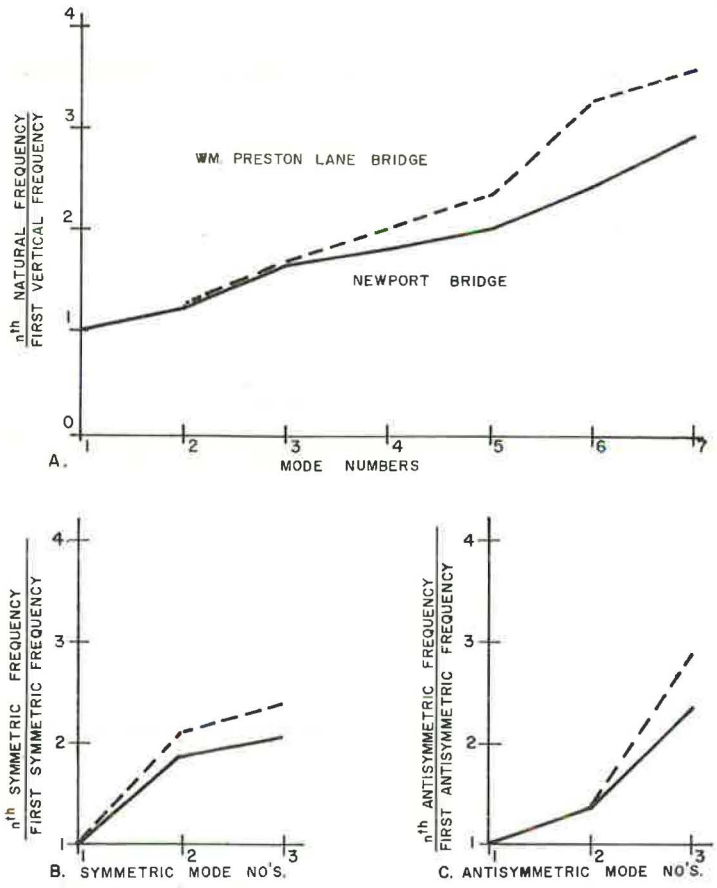

Figure 9. Frequency ratios.

These observations provide helpful insight into frequency ratios for these 2 bridges. While these bridges differ in many aspects, it is clear that common general trends exist in their frequency ratios. To be sure, these vertical frequency ratios reflect the fact that each bridge deck behaved to a fair degree of approximation like a multiple-span, simply supported, continuous beam.

The previous paragraphs of this section provide a qualitative basis for the assumption that the gross behavioral characteristics of bridges can, to a fair degree of accuracy, be placed into categories. Of course, for the final design of a bridge, natural frequencies should be obtained by using state-of-art analysis techniques. However, experimentally obtained guidelines such as these will help in preliminary design and analysis verification phases of a project.

ACKNOWLEDGMENT

The work in this paper was financed, in part, by the Federal Highway Administration.

REFERENCES

1. McLamore, V. R. Ambient Vibration Survey of Chesapeake Bay Bridge. Teledyne Geotronics, Long Beach, Calif., 1970.
2. McLamore, V. R. Ambient Vibration Survey of Newport Bridge. Teledyne Geotronics, Long Beach, Calif., 1970.
3. McLamore, V. R., Hart, G. C., and Stubbs, I. R. Ambient Vibration of Two Suspension Bridges. Submitted for publication to Jour. Struct. Div., Proc. ASCE.
4. Crandall, S. H., and Mark, D. Random Vibration. Academic Press, Boston, 1963.
5. Crawford, R., and Ward, H. S. Determination of the Natural Periods of Buildings. Bull. Seis. Soc. America, Vol. 54, Dec. 1964, pp. 1743-1756.
6. Bendat, J. S., and Piersol, A. G. Measurement and Analysis of Random Data. John Wiley and Sons, New York, 1966.

STATIC AND FATIGUE STRENGTHS OF BEAMS CONTAINING PRESTRESSED CONCRETE TENSION ELEMENTS

J. F. Mirza and Paul Zia, North Carolina State University at Raleigh; and
J. R. Bhargava, Atlas Prestressing Corporation, Alexandria, Virginia

This study concerns the static and fatigue behavior of composite beams containing a 2-in. square precast tension element, concentrically prestressed with a single $^{7}/_{16}$-in. diameter 7-wire strand. The element was positioned in the 6 in. wide, 9 in. deep, and 120 in. long beam such that its centroid was 2 in. from the tension face. Two static tests were conducted to obtain the elastic and inelastic load-deflection behavior of the composite member and to determine P_{cr}, the load corresponding to initial cracking in the tension element, and P_u, the ultimate load. Repeated load tests were conducted on 17 beams. The principal objective was to determine the behavior of the tension element under conditions that simulated those at a continuity connection in a highway bridge and, in particular, to ascertain the fatigue strength of the tension element. The scope of this investigation was limited to the application of repeated loads over a range of 0.5 to 2 P_{cr}. Test results clearly indicate that the magnitude of the peak load determines the mode of failure. Results revealed that use of the tension element for continuity connection creates a section that is superior to one using conventional reinforcement because it increases the cracking load of the section by 58.0 percent and, thus, provides better protection of the reinforcement against corrosion.

•THE USE of precast, prestressed concrete prisms (or rods) as tension elements has been discussed earlier by a number of investigators (1, 2) and more recently by Burns (3), Hanson (4), Bishara and Almeida (5). The earlier investigations have been summarized by Hanson.

The principal advantage of using precast, prestressed concrete tension elements as reinforcement is crack control. The precompressed concrete tension element exerts a restraining effect on the surrounding cast-in-place concrete so that the cracking moment of a section can be increased. In addition, cracks also tend to close after the load is removed because of the high tensile force in the pretensioned strands.

In prestressed concrete bridge construction, it is sometimes advantageous to establish continuity between precast, prestressed girders by placing reinforcement in the cast-in-place deck across the interior support. Control of flexural cracking in the composite T-beam flanges is then a problem in the negative moment regions of the continuous bridge. Both Burns and Hanson have suggested that precast, prestressed concrete prisms can be used to advantage as reinforcement in this type of continuous bridge. Their studies, however, have been limited to static tests only.

In order for this technique for developing continuity to be usable and acceptable for highway bridge construction, the fatigue behavior of the composite section consisting of the tension rods requires evaluation. The purpose of this investigation is to determine the effects of repeated load on the behavior of the composite member reinforced with the prestressed concrete tension element.

Sponsored by Committee on Concrete Superstructures and presented at the 50th Annual Meeting.

EXPERIMENTAL PROGRAM

Scope of Test Program

Nineteen beams were tested under 3 different loading conditions. These tests may be categorized as follows:

1. Two beams were tested under static load to failure to observe their static behavior and to determine the cracking and ultimate load.
2. Nine beams were subjected to different magnitudes of repeated loading, not more than the cracking load, that was discontinued after 1 million cycles and followed by a static test to failure. At several intermediate stages, static load tests were conducted after a predetermined number of cycles of loading. The load for these intermediate static tests never exceeded the magnitude of the repeated load. From these static tests, the variation of the beam stiffness was determined from the load-deflection curve.
3. Eight beams were subjected to repeated loading, in excess of the cracking load, that was continued until failure occurred. Intermediate static tests were also conducted to determine change of the beam stiffness.

Precast, Prestressed Concrete Tension Element

Each element was a concrete prism of 2 in. by 2 in. by 10 ft axially prestressed by a $^{7}/_{16}$-in. diameter 7-wire strand. The elements were fabricated on a prestressing bed in a continuous wooden form with end blocks at 10-ft intervals. The initial tension in the prestressing strand was 18,900 lb. The strand had a yield strength of 249 ksi corresponding to 1 percent extension, an ultimate strength of 270 ksi, and a modulus of elasticity of 28,000 ksi.

The concrete used in the elements was made with type III portland cement. The fine aggregate was well-graded sand with a fineness modulus of approximately 3.0, and the coarse aggregate was gravel with a maximum size of $^{3}/_{8}$ in. The concrete mix per cubic yard consisted of 708 lb cement, 1,280 lb sand, 1,650 lb gravel, 36 gal water, and 17$^{1}/_{2}$ oz admixture.

The ingredients were mixed thoroughly in a power-driven mixer and carefully scooped into the form. The concrete was vibrated by external application to the form. The element was rough-finished by wooden float in order to have a good bonding surface. After the concrete had been cured under wet burlap for 7 days, the strands were released. The concrete cylinder strength at the time of prestress transfer was 5,328 psi.

Twenty elements were cast, one of which was used as a control specimen to measure the loss of prestress periodically during the period of investigation.

Test Beams

Concrete test beams reinforced with the prestressed element were cast in 4 groups of 4 beams each and 1 group of 3 beams. The groups are labeled A, B, C, D, and E according to the order of casting. The beams were cast in plywood forms. Before concrete was placed, the tension element was secured by steel wires and aligned in position. All the test beams were of rectangular cross sections, 6 in. wide, 9 in. deep, and 10 ft long. The tension element was positioned such that its centroid was 2 in. from the top as shown in Figure 1. There was no other reinforcement.

Ready-mixed concrete was used in the test beam. The concrete mix per batch was made up of 615 lb cement, 1,213 lb sand, 1,800 lb gravel, 283 lb water, and 13 oz Placewell and 2.16 oz Aircon as admixtures. After being placed, the concrete was internally vibrated with needle vibrators and trowel-finished at the surface. The average cylinder strength at 28 days was 3,250 psi.

Twenty-four hours after casting, the concrete was covered with wet burlap. The forms were removed 2 days later, and the specimens were further cured for 15 days under wet burlap. Following this, the beams were allowed to be air-cured in the laboratory for at least 21 days before testing.

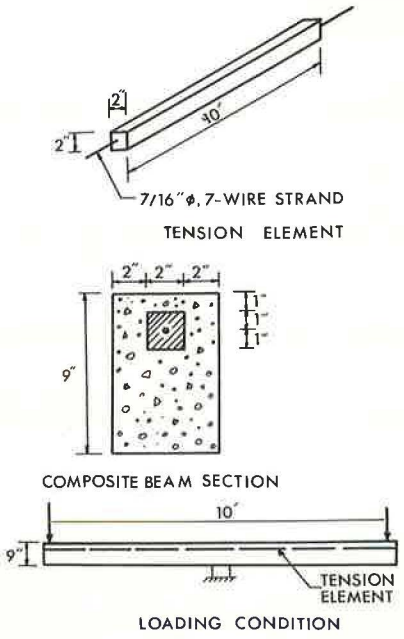

Figure 1. Tension element and composite beam.

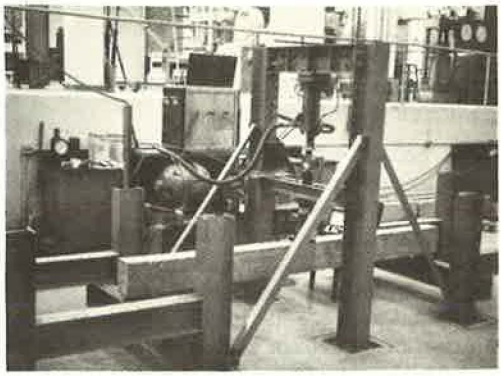

Figure 2. Static test arrangement.

Test Procedure

Static Tests—The typical arrangement of the test setup is shown in Figure 2. The beam was supported on roller bearings over a 10-ft span with a single point load applied at midspan by a 5-ton capacity hydraulic jack. The applied load was monitored by a Bourdon hydraulic gage. Midspan deflection was measured by a 0.001-in. dial gage at the centerline on the tension face of the beam. Following the application and removal of a small load to ensure proper seating of the test specimen, the load was applied in increments of 504 lb until failure. Load and deflection readings were recorded.

Intermediate Static Tests—The test setup was only slightly different from that of the static tests in that the load was applied by means of a smaller hydraulic jack and measured by a load cell. Static loads were applied in small increments until they were equal to the magnitude of the repeated load. Load cell and deflection gage readings were recorded.

Repeated Load Test—The arrangement of the test setup is shown in Figure 3. The repeated load machine consists of 2 systems: the hydraulic system for applying the load and the electronic system for controlling the frequency and magnitude of the maximum and minimum load. The frequency of the repeated load was maintained at 1.5 cps for all tests. The electronic system includes a counter for recording the number of cycles of load application. In each load application, the minimum load was kept as 10 percent of the maximum. Load was monitored by a load cell and required periodic adjustment as the stiffness of the test specimen changed. After the predetermined number of loadings, the machine was stopped and intermediate static tests were conducted before the repeated loading was resumed. The machine was equipped with a limit switch that would turn off all systems if

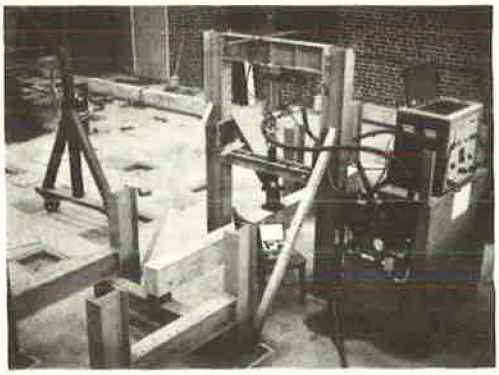

Figure 3. Repeated load test arrangement.

the deflection of the test beam became excessive because of either fracture or excessive loss of stiffness.

TEST RESULTS

Static Tests

The initial cracking load P applied at midspan of a simply supported beam of span L is

$$P = (4f_tS)/L$$

where S is the section modulus and f_t is the tensile strength of the concrete. For a split cylinder strength of 385 psi and for S = 81 in.^{3} and L = 120 in., the predicted initial cracking load for the composite test beam was 1,039 lb. The transformed section of the steel was neglected.

To determine the load at which cracks would initiate in the tension element, consider the force F_{tc} in the tendon when the element is on the verge of cracking.

$$F_{tc} = F_i(1 - L) + nF_i(1 - L)\,(A_s/A_c) + f_{tt}nA_s$$

where

E_s = modulus of elasticity of steel;
E_c = modulus of elasticity of tension element concrete;
$n = E_s/E_c$ = modular ratio taken as 6;
A_s = area of steel strand = 0.116 in.^{2};
F_i = initial tendon force = 18,900 lb;
L = total measured loss of prestressing force = 45.8 percent for 53 days or 57.3 percent for 62 days;
A_c = net area of tension element; and
f_{tt} = tensile strength of concrete used in tension element = 500 psi.

Thus,

$$F_{tc} = 12{,}428 \text{ lb for 53 days and } 12{,}093 \text{ lb for 62 days}$$

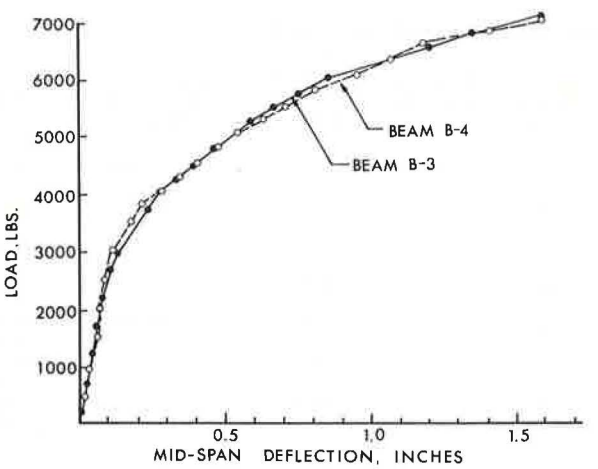

Figure 4. Load-deflection characteristics of specimen B-4 and A-3 subjected to static loading.

TABLE 1

RESULTS OF REPEATED LOAD TESTS RL-1

Beam	Magnitude of Repeated Loads (lb)	Frequency of Loading (cps)	Intervals for Intermediate Static Test (cycles)	Ultimate Load (lb) in Final Static Load Test[a]
A-4	1,500	1.5	1 million	8,315
B-3	1,500	1.5	1 million	8,120
C-1	1,500	1.5	1 million	8,038
A-1	2,250	1.5	¼ million	6,666
B-2	2,250	1.5	¼ million	7,778
B-1	2,250	1.5	½ million	7,206
A-2	3,000	1.5	1 million	6,652
C-3	3,000	1.5	¼ million	7,037
C-4	3,000	1.5	¼ million	7,037

Note: Repeated load test discontinued after a total of 10^6 cycles of load applications.

[a]Yielding of steel was mode of failure for all beams in final static load test.

The total tensile force causing cracking in the tension element is, therefore,

$$T = F_{tc} + f_{tt}A_c = 14{,}035 \text{ lb for 62 days}$$

The neutral axis of the cracked section (tension element on verge of cracking) is 2.81 in. from the extreme compression fiber, and the resultant compressive force is located at 0.94 in. from the compression face. The internal moment arm is, therefore, 6.06 in. Thus, the cracking moment M_{cr} is 85,053 in.-lb, which corresponds to an applied load P_{cr} = 2,835 lb for the 62-day test. For the 53-day test, the corresponding cracking load is 2,903 lb.

Consider a similar beam with conventional reinforcing steel placed at the same location as the prestressed tension element. The moment corresponding to a tensile stress of 385 psi in concrete at the level of the steel is 56,000 in.-lb. This indicates that the use of the tension element increases the cracking moment capacity by approximately 52 percent (85,053/56,000 = 1.52).

The theoretical ultimate moment of the composite section computed at the 1 percent yield strength of the prestressing strand and a concrete cylinder strength of 3,250 psi is 177,000 in.-lb. This corresponds to an applied load of 5,940 lb, which is a conservative estimate as shown by Figure 4.

The load-deflection curves of the 2 static tests are shown in Figure 4. Almost no change in beam stiffness is noted at the load corresponding to initial cracking of beam which is 1,039 lb. However, a decrease in beam stiffness is noted at approximately 3,000 lb corresponding to the calculated cracking load of the tension element.

Repeated Load Tests

The magnitude of the repeated loads, the interval for intermediate static tests, the number of load applications at which tests were discontinued, and the mode of failure are all given in Tables 1 and 2 for tests RL-1 and RL-2 respectively. A typical set of

TABLE 2

RESULTS OF REPEATED LOAD TESTS RL-2

Beam	Magnitude of Repeated Load (lb)	Frequency of Loading (cps)	Intervals for Intermediate Static Text (cycles)	Number of Cycles at Which Failure Occurred	Mode of Failure
E-3	2,750	1.5	—[a]	1,903,362	Rupture of steel due to fatigue
D-1	3,000	1.5	—[a]	1,787,961	Rupture of steel due to fatigue
D-3	3,500	1.5	20,000	288,000	Rupture of steel due to fatigue
D-4	4,000	1.5	20,000	105,651	Rupture of steel due to fatigue
C-2	4,500	1.5	20,000	90,720	Rupture of steel due to fatigue
D-2	5,000	1.5	10,000	59,572	Rupture of steel due to fatigue
E-1	5,500	1.5	10,000	20,700	Fatigue failure of concrete
E-2	6,000	1.5	—[a]	250	Fatigue failure of concrete

Note: Repeated load tests continued to failure.

[a]No static test conducted.

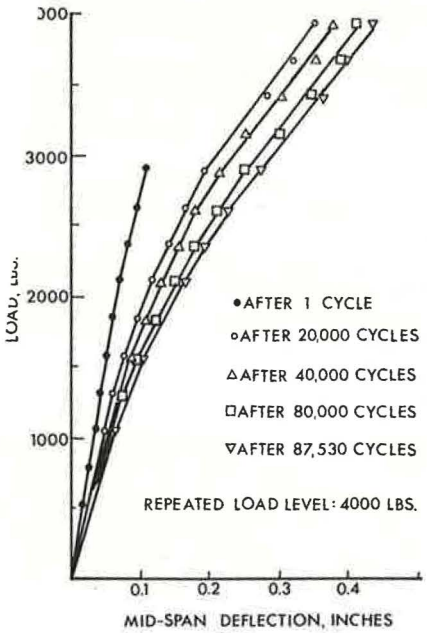

Figure 5. Load-deflection characteristics of specimen D-4 during course of repeated loading test RL-2.

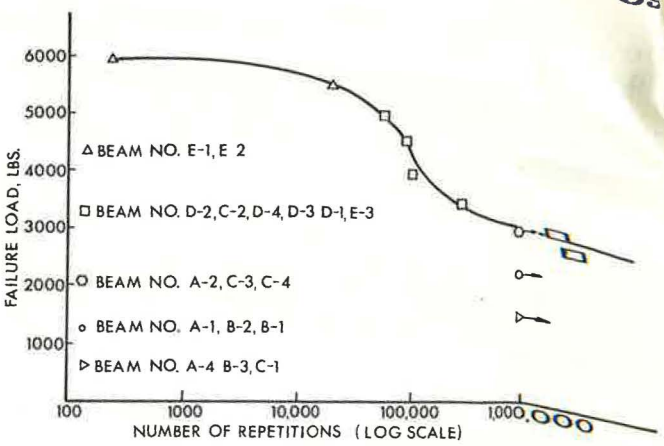

Figure 6. Repeated loading test results.

load deflection curves from intermediate static tests is shown in Figure 5. It is quite clear that there was a gradual reduction in beam stiffness as the number of load applications increased.

Figure 6 shows the results of the repeated load tests in which the peak magnitude of the repeated load is plotted as a function of the number of cycles of loading at which failure occurred. The L-N curve is characteristically Z-shaped with the upper end approaching asymptotically the static ultimate load and the lower end approaching asymptotically the load level of 2,500 lb, which corresponds to approximately 80 percent of the calculated cracking load for the tension element.

CONCLUSIONS

The following conclusions may be drawn on the basis of this investigation.

1. Over the upper range of loads from 1.7 to 2.0 P_{cr}, failure resulted from fatigue of concrete well before 1 million cycles, indicating a low fatigue life.
2. A typical curve of repeated load versus number of cycles of loading corresponding to fatigue failure (on semilog scale) consists of a central segment from P_{cr} to 1.7 P_{cr} that has a steep slope and represents the loading range over which failures resulted from fatigue of prestressing steel after a load application of less than 1 million cycles.
3. Over the range of load less than 0.7 P_{cr} (or approximately 0.3 P_u), the composite beam sustained repeated load application of well over 1 million cycles without fatigue failure.
4. The tests substantiated previous investigations that failure by fatigue before 1 million cycles of load is unlikely when the magnitude of the repeated load does not exceed the cracking load of the prestressed element.
5. The use of such a tension element for continuity reinforcement creates a section that is superior to mild steel reinforcement because it increases the cracking load of the section by 52 percent and, thus, provides better protection of the reinforcement against corrosion.
6. The loss of stiffness of the composite member, as measured by the deflections, was dependent on the magnitude of the repeated load. In general, the higher the magnitude of the repeated load is, the greater the rate of progressive loss of stiffness will

be. When the magnitude of the repeated load is less than the cracking load, stiffness loss is negligible.

7. A gradual loss in stiffness was definitely detected with the application of repeated loads of magnitude in excess of the cracking load. This is probably due to the progression of cracks deeper and deeper into the section and also due to some deterioration in concrete strength.

8. Because the progressive loss of stiffness is usually a signal that cracking is gradually advancing into the section, it is also a positive signal that failure due to fatigue before 1 million cycles of load is highly probable.

9. The loss of stiffness after initial cracking of the composite section was much smaller than expected. This further reinforces the belief that cracks may be prevented from advancing deeper into the section by the restraining effect of the tension element.

ACKNOWLEDGMENT

This paper is based on a research project conducted through the Highway Research Program in the Department of Civil Engineering at North Carolina State University (6). The project was sponsored by the North Carolina State Highway Commission and the Federal Highway Administration. Gratitude is expressed to E. G. Kandasamy for assistance in conducting the testing program and to Arnold Stone Company, Greensboro, North Carolina, for manufacture and supply of the prestressed tension elements.

REFERENCES

1. Evans, R. H., and Parker, A. S. Behavior of Prestressed Concrete Composite Beams. ACI Jour., Proc. Vol. 51, May 1955, pp. 861-878.
2. Evans, R. H., and Kong, F. K. The Extensibility and Microcracking of the Insitu Concrete in Composite Prestressed Concrete Beams. Structural Engineer, Vol. 42, June 1964.
3. Burns, N. H. Development of Continuity Between Precast Prestressed Concrete Beams. Jour. of Prestressed Concrete Institute, Vol. 2, No. 3, June 1966.
4. Hanson, N. W. Prestressed Concrete Prisms as Reinforcement for Crack Control. Jour. of Prestressed Concrete Institute, Vol. 14, No. 5, Oct. 1969, pp. 14-31.
5. Bishara, A., and Almeida, F. N. Concrete Beams With Prestressed Reinforcement. Jour. of Struct. Div., Proc. ASCE, Vol. 96, No. ST7, July 1970, pp. 1445-1460.
6. Mirza, J. F., Zia, P., and Bhargava, J. R. Static and Fatigue Strengths of Beams Containing Prestressed Concrete Tension Elements. North Carolina State University, Raleigh, final report.

FLANGE PROPORTIONS FOR CURVED PLATE GIRDERS

Charles G. Culver, Department of Civil Engineering, Carnegie-Mellon University, Pittsburgh, Pennsylvania

The results of analytical studies dealing with local flange buckling of horizontally curved plate girders are discussed. The relationship between the factor of safety against local buckling and the ratio of warping torsional normal stress to bending stress is plotted for several values of the flange width-thickness ratio. Two possible allowable stress design criteria are used to determine the factor of safety. In the first, the total stress at the flange tip, warping plus bending, is limited to $0.55F_y$. In the second, the total stress at the quarterpoint of the flange width is limited to $0.55F_y$. The influence of residual stresses is included in the results for girders fabricated by heat-curving or flame-cutting curved plates and then welded. Both A-36 and A-441 steel girders are considered. The results indicate that the factor of safety against local buckling using the first criterion for curved girders fabricated by welding or heat-curving and having width-thickness ratios equal to or less than those currently given by the AASHO specification remains substantially the same as for straight girders. For the second criterion, the factor of safety decreases as the ratio of warping to bending normal stress increases. Critical width-thickness requirements for girders fabricated by cold-bending are shown to be smaller than the present AASHO limit if local buckling is to be prevented during the fabrication process.

•DESIGN specifications for highway bridges (1) contain provisions limiting the width-to-thickness ratio for the compression flanges of beams and plate girders. These provisions based on local buckling considerations are currently limited to straight girders. Similar provisions do not exist for horizontally curved girders. The purpose of this paper is to summarize existing analytical work (2, 3, 4) on local buckling of curved plate girders. The results may be used to establish design requirements for curved girder flanges. Provisions for spacing of lateral bracing (usually expressed in terms of the flange width) based on overall lateral torsional buckling will not be considered here. Comparison of the analytical results with recent tests on curved plate girders is presented elsewhere (5).

BACKGROUND

The following 3 factors affect the local buckling behavior of curved girders: (a) flange curvature (geometrical effect) expressed in terms of the width of half of the flange, b, and the radius of the girder, R_w, i.e., b/R_w; (b) prebuckling stress condition (stresses due to applied loads); and (c) fabrication process, which affects the residual stresses. Values of flange curvature up to $b/R_w = 0.01$ were considered in the analytical studies. This would correspond to a girder with a 2-ft flange on a 100-ft radius. A survey of 28 curved bridges built in the United States indicated that an average value of this parameter was $b/R_w = 0.0025$. Numerical results indicated that, for flange curvatures less than or equal to 0.01, curvature was not important. Differences between the buckling stress for a straight girder, $b/R_w = 0$, and that for a curved girder, $b/R_w = 0.01$, were only 2 to 3 percent. The results presented in the next sec-

Sponsored by Committee on Steel Superstructures.

tion for $b/R_w = 0.01$ are, therefore, applicable within the entire range of practical flange curvatures.

The prebuckling stress condition in a curved plate girder is different from that in a straight girder. Because of the curvature, the girder twists under load and warping normal stresses develop in addition to the bending stresses (3). The magnitude of these torsional stresses, which vary linearly across the flange width, is influenced by the torsional rigidity of the bridge cross section. The efficient use of lateral diaphragms can significantly reduce the magnitude of these stresses. Results presented here will be given for a wide range of warping to bending stress ratios, σ_w/σ_B (Fig. 1a).

Residual stresses developed in the fabrication process significantly affect the flange buckling behavior. Girders fabricated as follows will be considered: (a) flame-cutting the flanges to the desired curvature and then welding the flanges and web; (b) cold-bending a straight girder or rolled beam; and (c) heat-curving. Residual stress patterns produced by these 3 fabrication processes are presented elsewhere (2, 6).

NUMERICAL RESULTS

Before the requirements for curved girders are considered, it is of interest to evaluate the "factor of safety" inherent in the AASHO specification for straight girders. For an A-36 steel girder, the width-thickness requirement in this specification is $b/t = 11.5$. Using the residual stress pattern for a welded plate girder with $b/t = 11.5$ and solving the buckling problem for a girder subjected to pure bending gave a critical moment (moment at which local buckling occurs) of 99 percent of the yield moment, $M_y = \sigma_y S$ (2). For an allowable stress of $0.55\sigma_y$, this gives a factor of safety of 1.80. Similar computations for a girder with A-441 flanges and $b/t = 10$ gave a factor of safety of 1.69. Dividing the critical moment for a curved girder by the allowable design moment to determine the factor of safety provides a direct means of comparison between the straight and curved girder.

To determine the design moment requires that the allowable stress criteria first be established. One possibility involves limiting the total stress at the flange tip, warp-

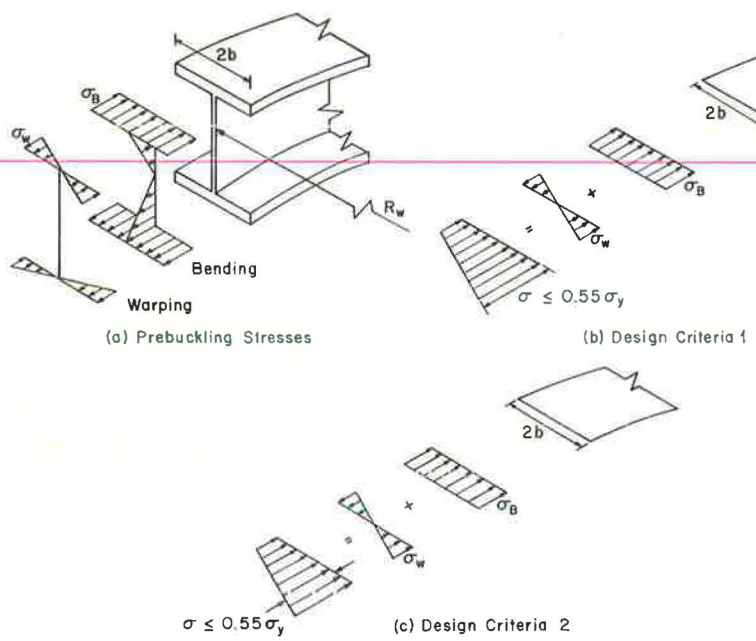

Figure 1. Possible allowable stress design criteria.

ing plus bending, to $0.55\sigma_y$ as shown in Figure 1b. In view of the fact that the warping stresses vary over the flange width, some designers choose to limit the average stress, warping plus bending at the middle of half the flange or at the quarterpoint of the flange, to $0.55\sigma_y$ (Fig. 1c). Obviously the total stress at the flange tip for this case is greater than that currently allowed for straight girders. Both criteria will be considered here.

Graphs of the factor of safety as a function of the warping to bending stress ratio for A-36 and A-441 welded and heat-curved girders are shown in Figures 2 through 5 for both design criteria. Curves for specific values of b/t are given. The points plotted represent the values of σ_w/σ_B for which the critical moments were calculated. No attempt was made to consider all the possible combinations of this ratio. The factor of safety was determined by dividing the critical bending moment for the particular ratio of σ_w/σ_B by the bending moment for each of the 2 design criteria using the same ratio of σ_w/σ_B. The influence of residual stresses was taken into account in determining the critical moment.

The residual stress pattern used for the welded girder was obtained from measured values used in previous studies (2). For the heat-curved girder, calculated residual stresses for a type 3 heat and a temperature of 1,150 F were used (6). Because the residual stress pattern for a welded girder is the same for both halves of the flange, the results shown in Figures 2 and 3 do not depend on the direction of the warping stress gradient (compression on inside or outside flange tip). For the heat-curved girder, however, the residual stress pattern is not symmetric about the web. The results were obtained for compressive warping stresses on the inside flange tip (toward the center of curvature). Because for this heating condition (type 3) the tensile residual stresses produced by heat-curving are theoretically somewhat lower on the inner flange tip than on the outer flange tip and are beneficial from the standpoint of local buckling (2, 4),

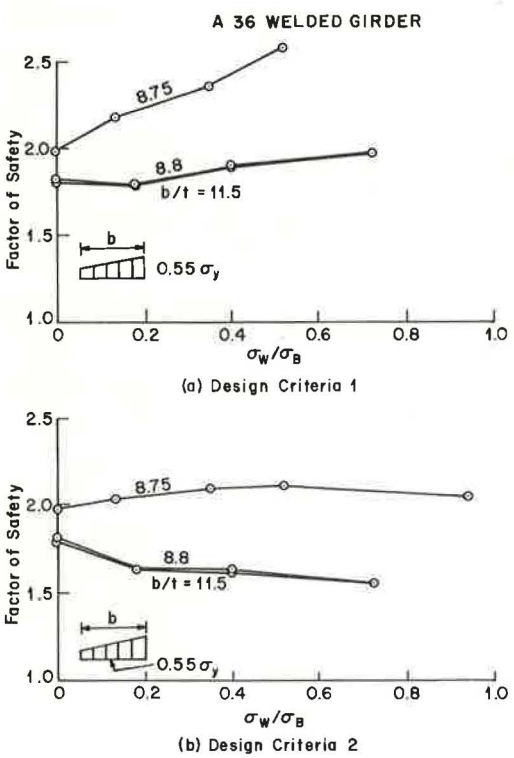

Figure 2. Factor of safety for A-36 welded girder.

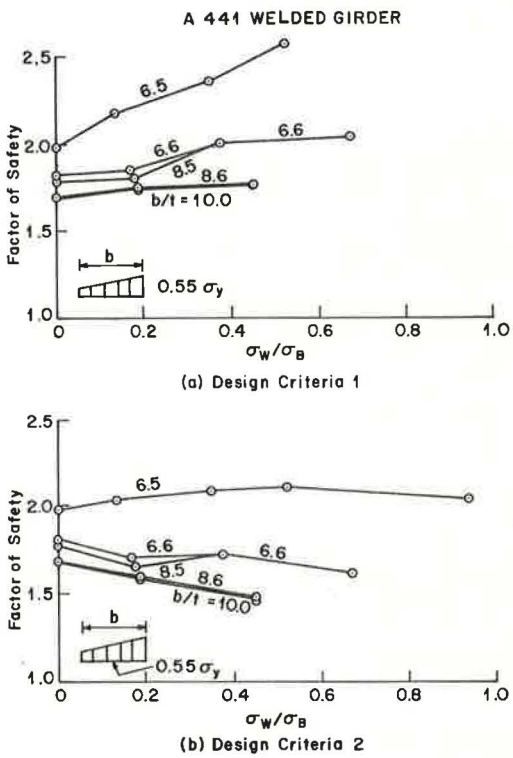

Figure 3. Factor of safety for A-441 welded girder.

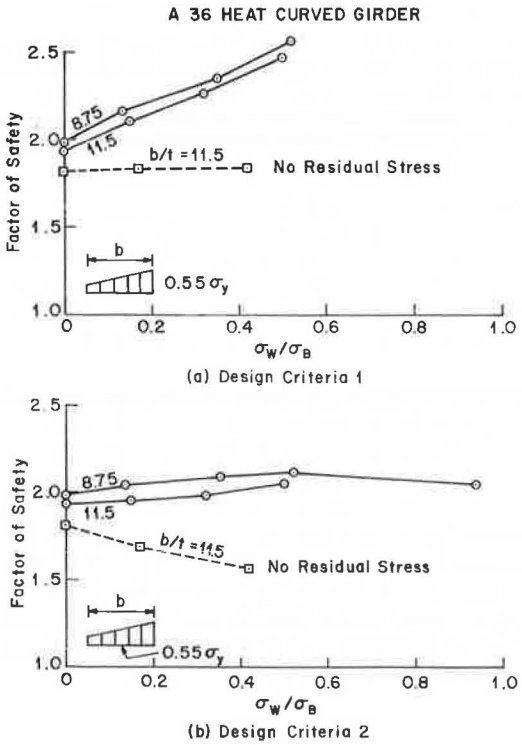

Figure 4. Factor of safety for A-36 heat-curved girder.

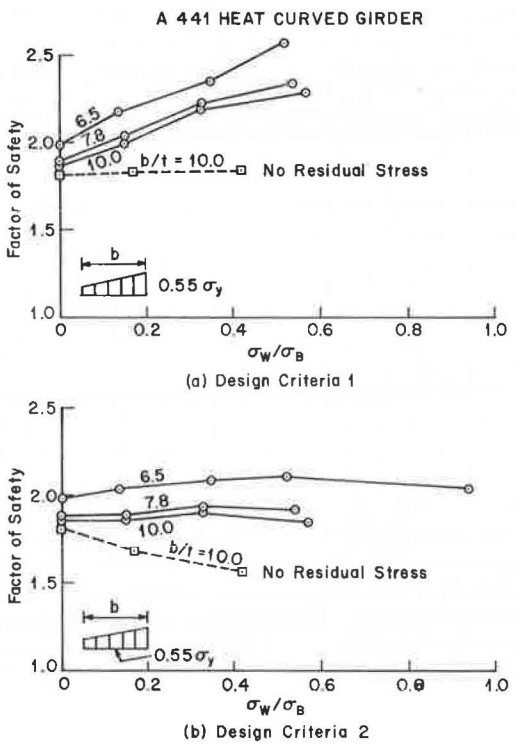

Figure 5. Factor of safety for A-441 heat-curved girder.

the results presented are conservative. The tensile residual stresses produced by lower heat-curving temperatures are less than those produced by the type 3 heat used in the analytical study (2). In Figures 4 and 5 curves are, therefore, shown for the case of zero residual stress. These curves represent lower bounds for heat-curved girders because the beneficial effect of the tensile residual stress at the flange tip produced by the heat-curving has been neglected.

Figure 2a shows that the factor of safety for b/t = 11.5 remains almost constant regardless of the value of σ_w/σ_B. Decreasing b/t to 8.8 hardly affects the results. This minor influence of width-thickness ratio on the factor of safety is due to the behavior of the plate buckling curves in the elastic-plastic region. The transition curves in this region differ from the overall column buckling slenderness ratio curves in that yielding at the outer flange tip produces a rapid reduction in buckling strength. For b/t = 8.75, however, the factor of safety is substantially increased. For this value of b/t, it is possible to fully yield half of the flange before local buckling occurs. For $\sigma_w/\sigma_B = 0$ and b/t = 8.75, the factor of safety is higher than that provided by the AASHO b/t value of 11.5. Because the girder can reach the fully plastic moment, the factor of safety reflects the shape factor, Z/S, of the cross section [$FS = M_p/0.55M_y = (M_y/0.55M_y)(Z/S) = (1.80)\,1.1 = 1.98$]. As σ_w/σ_B increases, the factor of safety with b/t = 8.75 increases. This is due to the fact that the rate of reduction in the plastic moment due to combined bending and torsion is less than the rate of reduction in allowable bending moment for combined bending and warping normal stress.

For the second criterion, Figure 2b shows a reduction in the factor of safety as σ_w/σ_B increases. Because the critical moment is not affected by the design criteria, this decrease is due to the higher allowable moment permitted by criterion 2 that limits the average flange stress rather than the maximum stress. It should be pointed out

that the state of stress at the flange tip has a significant effect on the buckling strength. For example, yielding of only a small portion of the flange near the tip drastically decreases the buckling strength (2). Note that, for $\sigma_W/\sigma_B \simeq 0.7$, the factor of safety is still 1.55. For b/t = 8.75, no reduction in factor of safety occurs.

The results shown in Figure 3 for an A-441 flange are similar to those shown in Figure 2 for A-36 steel.

The factors of safety shown in Figures 4 and 5 for a heat-curved girder designed by using criterion 1 actually increase as σ_W/σ_B increases. This is due to the beneficial effect of the tensile residual stresses produced at the flange tip by the heat-curving process. As noted previously for type 1 and type 2 heat-curving, this increase would be less. Also, because subsequent loading and unloading of the girder tends to reduce the residual stresses (7), this increase would be somewhat less after the first few loadings of the bridge. When criterion 2 is used, the tensile residual stresses offset the reduction because of the use of an average stress or a higher allowable design moment, and the factor of safety remains relatively constant as σ_W/σ_B increases.

Results for a cold-bent girder are shown in Figure 6. Instead of the factor of safety being determined, the flange proportions required to prevent local buckling during the cold-bending process were determined. Figure 6a shows the percentage of half flange width, ηb, which must be yielded during cold-bending to produce a particular curvature, b/R_W. This stress distribution was used to determine the corresponding values of b/t required to prevent local buckling during fabrication (Fig. 6b). Figure 6b shows that to cold-bend a girder to a curvature of $b/R_W = 0.001$ requires that the value of b/t be less than or equal to 9.1. These results indicate that the width-thickness ratios necessary to cold-bend girders to practical curvatures, $b/R_W > 0.0005$, are less than currently allowed in the AASHO specification.

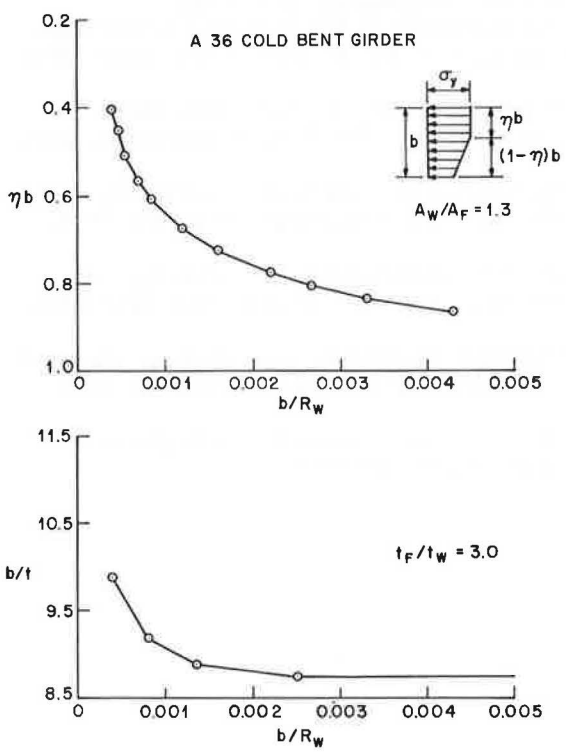

Figure 6. Flange requirements for cold-bending.

SUMMARY AND CONCLUSIONS

The factor of safety against local buckling for various flange width-thickness ratios for horizontally curved girders was evaluated. Two possible design criteria were considered. For the case in which the total stress at the flange tip, warping stress plus bending stress, is limited to $0.55\sigma_y$, the factor of safety for curved girders using present straight girder flange proportions, b/t, remains substantially the same regardless of the ratio of σ_W/σ_B. If the average stress in the most critically stressed half of the flange is limited to $0.55\sigma_y$, thus allowing the stress at the flange tip to exceed $0.55\sigma_y$, the factor of safety decreases if straight girder flange proportions are used. The maximum decrease is 14 percent for a welded girder with $\sigma_W/\sigma_B = 0.7$ ($\sigma_W/\sigma_B = 0$, FS = 1.80; $\sigma_W/\sigma_B = 0.7$, FS = 1.55).

The results presented here were concerned with allowable stress design. If a "load factor" design philosophy (8) is adopted for curved girder bridges, more stringent flange width-thickness requirements would be necessary (2). These requirements are

similar to those proposed for straight beams and girders (8).

NOTATION

The following symbols are used in this paper:

A_F = area of 1 flange;
A_W = area of web;
b = width of half of flange;
M = bending moment;
M_p = plastic moment;
M_y = yield moment;
R_W = centerline radius of girder;
S = section modulus;
t = flange thickness;
t_W = web thickness;
Z = plastic section modulus;
η = percentage of half flange that is yielded;
σ = normal stress;
σ_B = bending stress;
σ_W = warping normal stress; and
σ_y = yield stress.

ACKNOWLEDGMENTS

The results presented here were obtained in a research program concerning instability of horizontally curved bridge members sponsored at Carnegie-Mellon University by the Pennsylvania Department of Transportation. The cooperation of Foster Sankey, Wade Gramling, and Heinz Juhl of the Department of Transportation is gratefully acknowledged. Ghulam Nasir and Darryl Brogan provided invaluable assistance in preparing the material presented. The comments of Roger Brockenbrough, Applied Research Laboratory of the United States Steel Corporation, are also acknowledged.

REFERENCES

1. Standard Specifications for Highway Bridges, 10th Ed. American Association of State Highway Officials, Washington, D.C., 1969.
2. Culver, C., and Nasir, G. Instability of Horizontally Curved Members—Flange Buckling Studies. Carnegie-Mellon Univ., Pittsburgh, Nov. 1969.
3. Culver, C., and Frampton, R. E. Local Instability of Horizontally Curved Members. Jour. of Struct. Div., Proc. ASCE, Vol. 96, No. ST2, Proc. Paper 7079, Feb. 1970, pp. 245-265.
4. Culver, C., and Nasir, G. Inelastic Flange Buckling of Curved Plate Girders. Jour. of Struct. Div., Proc. ASCE, Vol. 97, No. ST4, Proc. Paper 8072, April 1971, pp. 1239-1256.
5. Mozer, J., and Culver, C. Horizontally Curved Highway Bridges—Stability of Curved Plate Girders. Carnegie-Mellon Univ., Pittsburgh, Rept. P1, Sept. 1970.
6. Brockenbrough, R. Theoretical Stresses and Strains From Heat Curving. Jour. of Struct. Div., Proc. ASCE, Vol. 96, No. ST7, Proc. Paper 7410, July 1970, pp. 1421-1444.
7. Brockenbrough, R. Criteria for Heat Curving Steel Beams and Girders. Jour. of Struct. Div., Proc. ASCE, Vol. 96, No. ST10, Proc. Paper 7638, Oct. 1970, pp. 2209-2226.
8. Vincent, G. S. Tentative Criteria for Load Factor Design of Steel Highway Bridges. American Iron and Steel Institute, Bull. 15, March 1969.

DYNAMIC DETERMINATION OF PILE LOAD-BEARING CAPACITY

Paul F. Gnirk, Kenneth E. Krause, Vernon L. Bump, and Kenneth E. Anderson,
South Dakota Department of Highways, Pierre

Consideration has been given to the development of an accurate method for obtaining the load-bearing capacity of a pile based on dynamic pile driving information. Based on the neglect of inertial forces and the assumption that the pile is a rigid body, the bearing capacity is approximately equal to the centroid (along the force axis) of the interaction force-time curve. The interaction force is obtained by the use of a load cell situated between the hammer and pile top. A more accurate determination of load-bearing capacity may be obtained by including the inertial effect in the analysis. The agreement between the dynamic predictions and the static load-test values for 8 full-scale piles is quite good. On the basis of force-displacement curves derived from force-time and displacement-time traces, approximately 95 percent of the rated energy output of the hammer is transferred to the soil-pile system. Finally, initial consideration is given to the model simulation of a hammer-pile-soil system on an analog computer.

•THE PRIMARY purpose of this study is to provide a predictive estimate of the load-bearing capacity of a pile based on dynamic information obtained during the driving process. The "static" bearing capacity of a pile generally changes with time subsequent to driving; i.e., the initial capacity of a pile immediately after driving may be more or less than that measured at some future date. The analyses presented here utilize information obtained during the driving process; hence, the calculated values of load-bearing capacities are of an initial nature.

The theoretical treatment of the dynamic features of hammer-pile-soil interaction as given here is patterned after the analytical approach and subsequent results obtained by Scanlan and Tomko (1). By the use of one-dimensional elastic wave theory, they demonstrate that the elastic contribution to the motion of the pile is small compared to the rigid-body contribution. Their investigation disclosed that the predicted load-bearing capacities of full-scale piles are not appreciably altered when the elastic portion of the pile motion is neglected. The elastic-rigid dynamic theory requires that the total dynamic displacement of a pile due to a hammer blow be the sum of the elastic and the rigid-body displacements. The rigid-body dynamic theory disregards the elastic motion of the pile.

By neglecting inertial forces and assuming that a rigid-body condition exists during the driving, we relate here the bearing capacity of a pile to the maximum interaction force developed between the hammer and the pile-soil system. Subsequently, the analysis is improved by inclusion of the inertial effects during pile motion. Comparisons are made between measured and predicted values of load-bearing capacities of full-scale piles. The rated kinetic energy outputs of the hammers are compared with the corresponding values of energy transfer during driving. Finally, a model of the hammer-pile-soil system is simulated on an analog computer.

Sponsored by Committee on Construction of Bridges and Structures and presented at the 50th Annual Meeting.

FIELD EXPERIMENTATION

During the course of the investigation, 21 full-scale piles were driven and subsequently load-tested at 5 different soil locations. Dynamic measurements of driving force and pile displacement were obtained for 7 of the 21 piles. The piles were fabricated from Douglas fir, precast concrete, steel H-beam, and steel pipe.

A diagram of the dynamic force-displacement measurement system and apparatus configuration is shown in Figure 1. The interaction force between the pile-soil system and the hammer was measured as a function of time by means of a calibrated load cell. The pile displacement as a function of time was measured with a linear variable differential transformer (LVTD). The same time base was used in recording the hammer force and pile displacement simultaneously on 2 channels of a magnetic tape recorder. Examples of the force and displacement-time traces are shown in Figures 2 through 5.

The force-time curves shown in Figures 2, 3, and 4 were recorded at a high sensitivity level on the magnetic tape recorder. Because of the hammer spike after the pulse maximum, the high-sensitivity FM amplifier on the recorder was overloaded, resulting in a distortion of the remainder of the force-time trace. In particular, the "tensile" portions of the traces are exaggerated. The force-time curve shown in Figure 5 was recorded on dc to 10 kHz regular FM and does not exhibit a negative pulse feature. However, because of internal reflections within the hammer-pile-soil system, the existence of a tensile "tail" on the interaction force-time record would not be physically unreasonable.

Static load tests were conducted by use of a hydraulic jack and a dial indicator in conjunction with a reaction beam and a configuration of anchor piles around the test pile. All piles were statically tested within 1 to 2 weeks after being driven and during a period of 3 to 12 months thereafter. During a test, the load was applied in 15-ton increments until the ultimate or failure load was attained. The minimum elapse time between load increments was 0.5 hour. Typical load-displacement curves are shown in Figure 6.

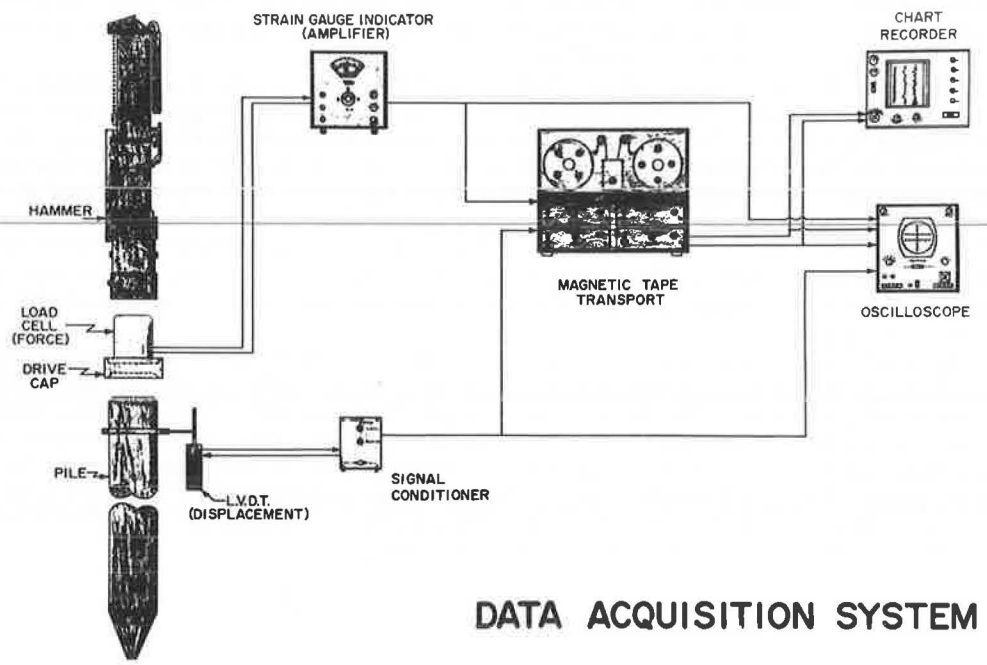

Figure 1. Schematic diagram of force-displacement measurement system and apparatus configuration for dynamic pile testing.

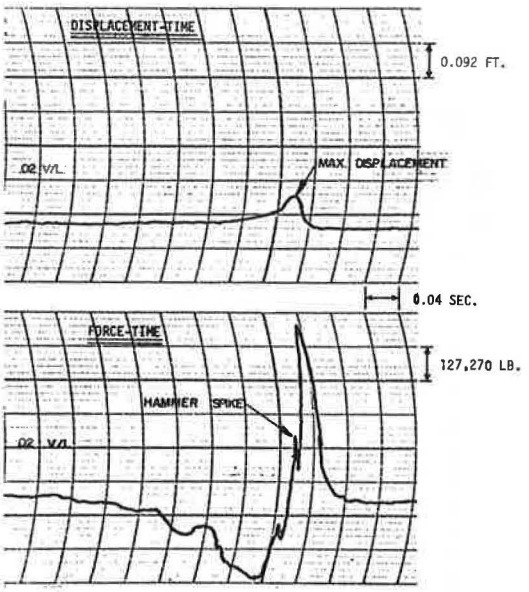

Figure 2. Displacement-time and force-time records for a 59-ft steel-pipe pile driven by a Link Belt 520 at the Watertown field site.

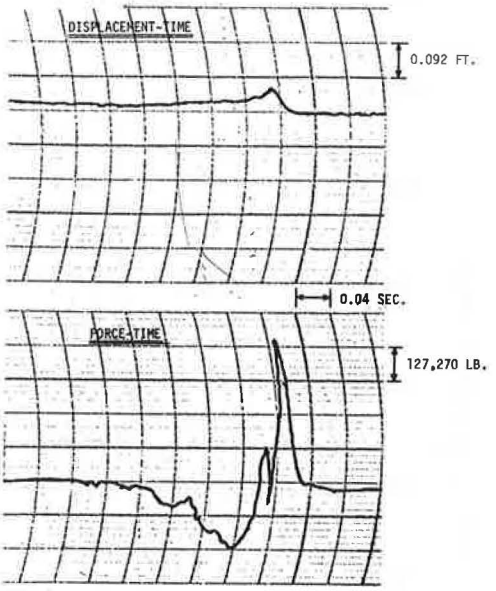

Figure 3. Displacement-time and force-time records for a 30-ft Douglas fir pile driven by a Link Belt 520 at the Madison field site.

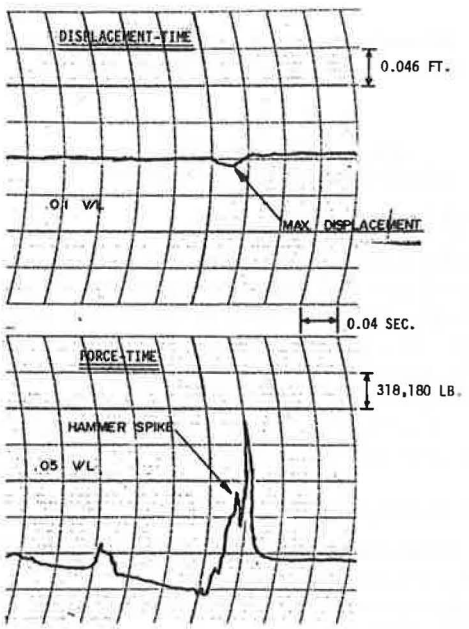

Figure 4. Displacement-time and force-time records for a 59-ft concrete octagonal precast concrete pile driven by a Link Belt 520 at the Watertown field site.

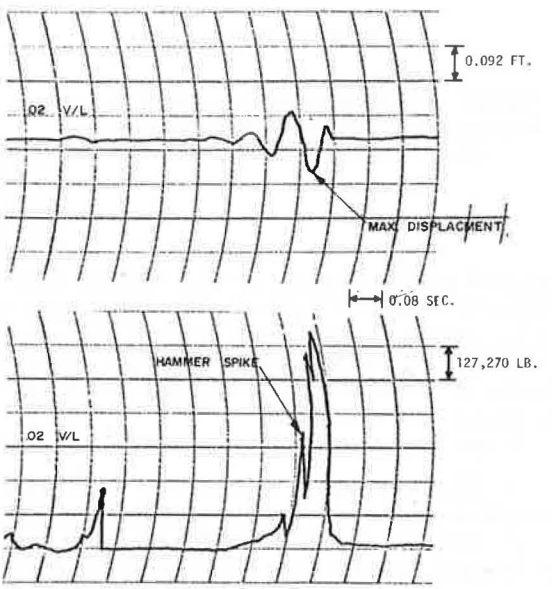

Figure 5. Displacement-time force-time records for a 123-ft steel H-beam pile driven by a Delmag D-22 at the Chamberlain field site.

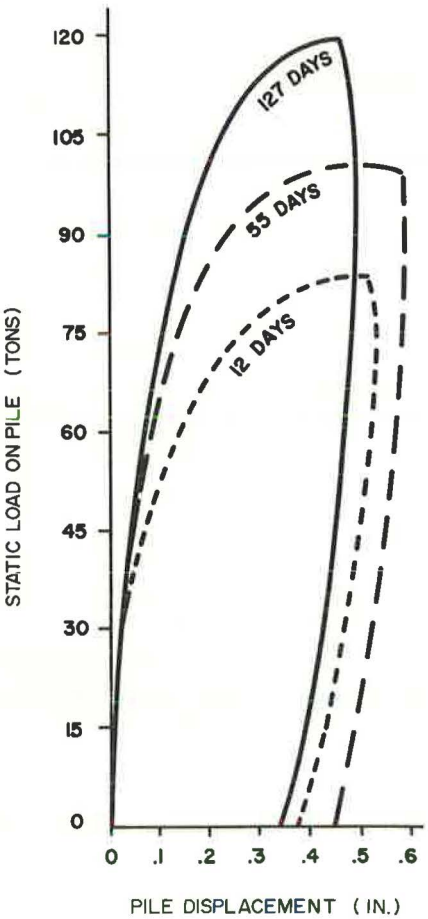

Figure 6. Load-displacement curves obtained from static load tests on a 35-ft tapered concrete pile at the Madison field site.

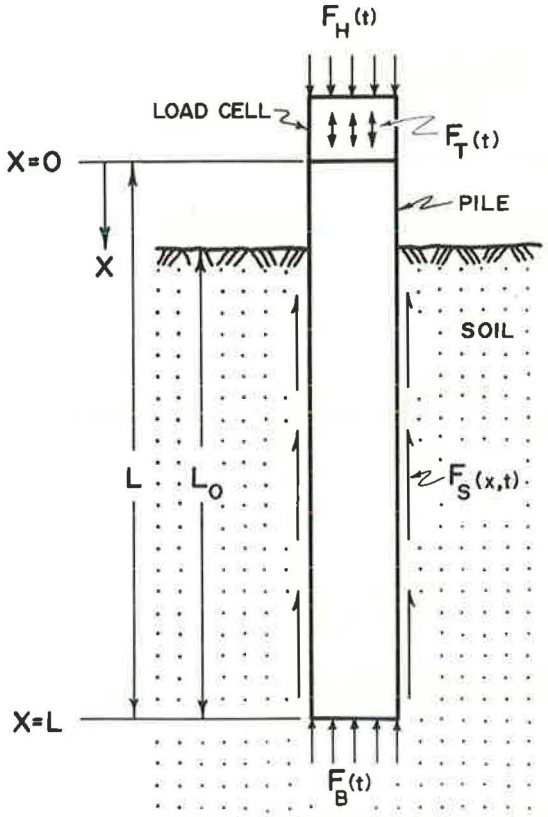

Figure 7. Schematic diagram of a pile subjected to an idealized system of driving and resistive soil forces.

ANALYSIS OF PILE LOAD-BEARING CAPACITY

Simplified Pile Model

Consider a pile of total length L and weight W_p situated in a soil mass, as shown in Figure 7; the length of pile actually in the soil is designated as L_o, where $L_o \leq L$. The top of the pile, i.e., at $x = 0$, is subjected to a time-dependent hammer force $F_H(t)$. The weight of the hammer is designated as W_H. The soil exerts a normal force $F_B(t)$ on the base of the pile, and a distributed "frictional" force $F_S(x, t)$ on the sides of the pile, i.e., for $L - L_o \leq x \leq L$. If the mechanical behavior of the soil is rate dependent, then the base and side forces must be considered as being time dependent.

In the analyses to follow, we use the following assumptions:

1. That the elastic wave motion in the pile is immediately dissipated by the soil and the predominant pile motion is effectively that of a rigid body; and
2. That the forces exerted by the soil on the pile at the base and along the sides can be lumped together into a composite resistive force of the form

$$F_B(t) + F_S(x, t) = F_R + cv(t) \qquad (1)$$

where F_R is the "static" bearing resistance of the soil, c is a "viscous" damping constant for the soil, and v(t) is the instantaneous rigid-body velocity of the pile.

If u(t) is the instantaneous rigid-body displacement of the pile and v(t) is the pile velocity, then the following energy terms are pertinent to the composite hammer-pile-soil system:

$$\begin{aligned} KE &= \tfrac{1}{2}[Mv(t)^2] \\ PE &= \tfrac{1}{2}[ku(t)^2] \\ DE &= \tfrac{1}{2}[cv(t)^2] \end{aligned} \tag{2}$$

where

KE = kinetic energy, ft-lbf;
PE = potential energy, ft-lbf;
DE = dissipation energy by viscous damping, ft-lbf;
$M = (W_p + W_H)/g$ = combined mass of hammer and pile, lb_f-sec^2/ft;
W_p = pile weight, lb_m;
W_H = hammer weight, lb_m;
g = 32.174 lb_m-ft/lb_f-sec^2; and
k = elastic constant for the composite hammer-pile-soil system, lb_f/ft.

The energy dissipated by Coulomb damping, i.e., by the resistive force F_R, is

$$DE = \int F_R \, du \tag{3}$$

The time-dependent force $F_T(t)$, as measured by a load cell situated between the hammer and the top of the pile, is not simply the hammer force $F_H(t)$; rather, $F_T(t)$ is the interaction force between the hammer and the pile-soil system. In view of data shown in Figures 2 through 5, $F_T(t)$ can be approximated by a sine function over the first half cycle.

$$F_T(t) = F_o \sin(\omega t) \quad \left(0 \le t \le \frac{\pi}{\omega}\right) \tag{4}$$

where F_o is the maximum force and ω is the frequency. The corresponding work or energy expended during the displacement of the pile is

$$W = \int F(u)du = \int F(t)\, v(t)dt \tag{5}$$

where $du = (du/dt)dt = v(t)dt$.

Load-Bearing Capacity Based on Energy-Impulse Considerations

In order to obtain a reasonable estimate of the initial load-bearing capacity of a pile, let us consider an energy balance over the hammer-pile-soil system. The work done by the forces of the hammer and the soil on the rigid pile during a displacement is equal to the change in kinetic energy of the pile during the same displacement. The change in kinetic energy of the pile over a time period of $t = \pi/\omega$, where ω is the frequency of the interaction force $F_T(t)$, is

$$E_H = \int_0^{\pi/\omega} F_T(t)\, v(t)dt \tag{6}$$

where E_H is the rated kinetic energy output of the hammer. The work done by the dissipative resistive force of the soil on the rigid pile over the same time interval is

$$E_R = \int_0^{\pi/\omega} \left[F_R + cv(t)\right] v(t)dt \tag{7}$$

The elastic strain energy stored in the entire system, including that of the hammer, pile, and soil, over the same time interval is

$$E_o = \int_0^{\pi/\omega} ku(t)\,v(t)dt \tag{8}$$

Let us suppose that the energy stored in the system over the time interval $0 \le t \le \pi/\omega$ is entirely dissipated in work done by the soil on the pile as the pile displaces into soil.

$$E_R = E_o \tag{9}$$

Basically, this implies that the entire hammer-pile-soil system is first compressed in a springlike manner with a potential energy E_o, and then the stored energy is completely dissipated by Coulomb and viscous damping as the pile is permanently displaced into the soil. Thus, an energy balance over the time interval $0 \le t \le \pi/\omega$, $E_o + E_R = E_H$ or $2E_R = E_H$, by Eq. 9 is written as

$$\int_0^{\pi/\omega} \left[F_T(t) - 2F_R\right] v(t)dt = 0 \tag{10}$$

where use is made of Eqs. 6 and 7, and the viscous damping coefficient c is taken as zero for simplification. As a good approximation, we may suppose

$$v(t) \cong BF_T(t) \tag{11}$$

where B = constant. This supposition implies that, if the function $F_T(t)$ is known, then v(t) is approximately a function of the same form, differing only by a constant; experimental field results indicate that $F_T(t)$, u(t), and v(t) are all of a sinusoidal nature, thus lending credence to the assumption. Substitution of Eq. 11 into Eq. 10 gives

$$F_R = \frac{\int_0^{\pi/\omega} F_T(t)^2 dt}{2\int_0^{\pi/\omega} F_T(t)dt} \tag{12}$$

According to this result, the bearing capacity of a pile is equal to the centroid of the interaction force-time curve. In particular, if $F_T(t) = F_o \sin(\omega t)$, then

$$F_R = (\pi/8)F_o \tag{13}$$

where F_o is the maximum interaction force.

From another viewpoint, this result implies that the impulse of the hammer force $F_H(t)$ must equal the impulse of the resistive bearing force F_R of the soil, and the sum of the 2 impulses must equal the impulse of the interaction force $F_T(t)$ as measured by the load cell. This result is intuitively reasonable on physical grounds. The primary deficiency in the analysis is the disregard of the effect of the inertial force of the hammer-pile system. The effect is additive with regard to the bearing force F_R. As the pile is displaced with relative ease into the soil, the inertia term is small as compared with F_R. However, at refusal, the inertial contribution is significant. In summary, this analysis yields a lower bound or minimum value on the bearing capacity of a pile; inclusion of the inertia term in the formulation will improve the estimate of the load-bearing capacity of the pile.

Load-Bearing Capacity Based on Energy-Displacement Considerations

The pile-soil system, when dynamically acted on by the hammer, behaves in a manner analogous to that of a damped simple harmonic oscillator. This premise is made with the assumptions that the pile acts as a rigid body and the pile-soil interaction acts as a damped elastic medium. The premise is substantiated by the fact that during a hammer blow the pile first exhibits a maximum displacement and then rebounds to a permanent displacement.

Under the assumption that the pile-soil system behaves as a simple harmonic oscillator, the sum of the kinetic energy and potential energy corresponding to the unrestricted movement of the oscillator will always be a constant. At the point of maximum displacement u_o, corresponding to zero velocity, the kinetic energy is zero and the potential energy is

$$PE = \tfrac{1}{2}(K u_o^2) \tag{14}$$

where K is the elastic constant of the oscillator. At any instant when the oscillator is in motion, the total potential and kinetic energy is equal to the potential energy at the point of maximum displacement, or zero velocity. The natural frequency of the displacement is

$$\omega_n = \sqrt{K/M} = 2\pi/T \tag{15}$$

where M is the total mass of the system, i.e., hammer plus pile, and T is the period of 1 cycle of the pile displacement. Thus, at any instant the energy required for the pile to exhibit simple harmonic motion is

$$E_o = \tfrac{1}{2}[M(\omega_n u_o)^2] \tag{16}$$

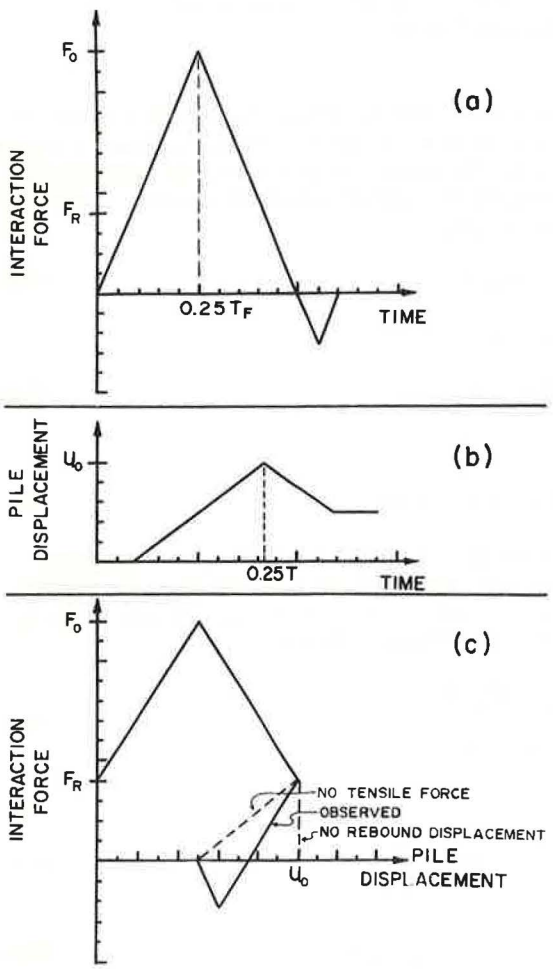

Figure 8. Simplified force-displacement-time curves for approximate simulation of dynamic pile behavior.

The triangular functions shown in Figure 8a and b are utilized as approximations to the sinusoidal forms of the interaction force $F_T(t)$ and the pile displacement u(t). We note that the force-displacement curve corresponding to these approximate functions, as shown in Figure 8c, bears a striking resemblance to the dynamic force-displacement curve obtained by field experimentation with a full-scale pile, as shown in Figure 9. In actuality, the analytical approach employed here is valid for any situation in which the functional forms of $F_T(t)$ and u(t) are similar; the use of triangular functions is only for the purpose of simplification.

The difference between E_o and the output energy of the hammer E_H is the energy required to permanently displace the pile into the soil. With reference to data shown in Figure 8c, we have (corresponding to time t = 0.25 T)

$$E_H - E_o = F_R u_o + \tfrac{1}{2}(F_o - F_R)u_o \tag{17}$$

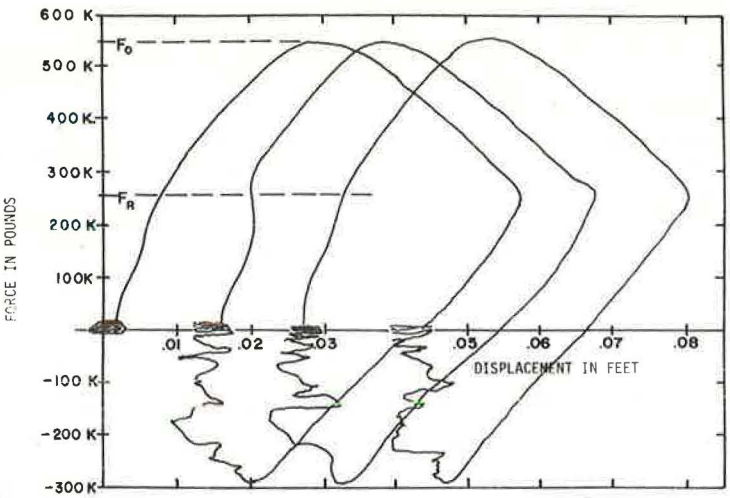

Figure 9. Dynamic force-displacement curves obtained from force-time and displacement-time records for a 59-ft steel-pipe pile driven by a Link Belt 520 at the Watertown field site.

According to the theory developed in the previous section, where the inertial force is neglected, the bearing capacity F_R of the pile is equal to the maximum interaction force F_o multiplied by the centroid of the force-time function. In this case, the forcing function is of a triangular shape, as shown in Figure 8a, and the centroid is equal to one-third of the maximum value of the interaction force; i.e,

$$F_R = F_o/3 \tag{18}$$

By substitution of Eq. 18 into Eq. 17, we obtain

$$F_o = \tfrac{3}{2}[(E_H - E_o)/u_o] \tag{19}$$

A force balance on the pile yields

$$M\{d[v(t)]/dt\} + F_R = F_T(t) \tag{20}$$

where v(t) is the instantaneous rigid-body velocity of the pile, and M is the combined mass of the hammer and the pile. Consider the instant of time during the pile motion at which the pile displacement is maximum, i.e., $u(t_o) = u_o$. At $t = t_o$, the pile velocity is zero and the pile acceleration is a negative maximum. Hence,

$$\begin{aligned} F_T(t_o) &= F_o/3 \\ d[v(t_o)]/dt &= -u_o\omega_n^2 \end{aligned} \tag{21}$$

Substitution of Eq. 21 into Eq. 20 gives

$$F_R = (F_o/3) + Mu_o\omega_n^2 \tag{22}$$

or

$$F_R = \tfrac{1}{2}(E_H/u_o) + \tfrac{3}{4}(Mu_o\omega_n^2) \tag{23}$$

where use is made of Eqs. 16 and 19. Thus, the bearing capacity F_R of the pile can be related to the hammer output energy E_H and the maximum pile displacement u_o; this analysis includes the effect of the hammer-pile inertia.

TABLE 1

COMPARISON OF CALCULATED AND MEASURED LOAD-BEARING CAPACITIES OF FULL-SCALE PILES

Pile	Total Length (ft)	In-Place Length (ft)	u_o Period (sec)	Maximum u_o (ft)	Total Weight of Hammer-Pile System, $W_H + W_p$ (lb_m)	Rated Out-Put Energy of Hammer, E_H(ft-lb_f)	Maximum Force, F_o (lb_f)	Load-Bearing Capacity (tons)		
								Equation 13	Equation 23	Static Field Test
Madison, tapered concrete	35	26	0.104	0.66	13,360	18,700	432,730	85	105	82 to 120
Madison, precast concrete	35	26.5	0.108	0.0734	13,640	20,700	483,640	95	110	80 to 115
Madison, wood	30	26	0.100	0.0734	8,855	17,700	560,000	110	90	90 to 140
Watertown west, wood	58.5	28.5	0.088	0.0624	9,945	19,500	636,360	125	115	135
Watertown east, wood	59.5	29.5	0.160	0.0550	9,985	13,700	432,730	85	72	80
Watertown, octagonal concrete	59	29	0.080	0.0174	18,200	21,200	1,209,090	237	326	330+
Watertown, steel pipe	59.3	29.5	0.100	0.041	9,080	17,700	661,820	130	125	140
Spearfish, steel H-beam	30	30	0.160	0.0587	8,175	12,500	560,000	110	61	50 to 75
Chamberlain, steel H-beam	123	123	0.112	0.0918	18,995	29,100	789,090	155	143	None

Comparison of Calculated and Measured Load-Bearing Capacity

On the basis of force-time and displacement-time data obtained during the actual pile-driving process, the load-bearing capacity of a pile can be calculated from either Eq. 13 or Eq. 23. The effect of the inertial force is included in the second expression, but not in the first. A comparison of the calculated load-bearing capacities with those measured statically for 8 full-scale piles is given in Table 1. In general, the quantitative correlation between the dynamically predicted and statically measured load-bearing capacities is quite good. A dynamic force-displacement curve, as obtained from a cross plot of the force-time and displacement-time records, can be utilized for an additional check on the general accuracy of the predictive techniques. Typical force-displacement curves for a steel-pipe pile driven with a Link Belt 520 are shown in Figure 9. The load-bearing capacity of the pile corresponds to the first break, or "knee," of the individual curves. From the curves for the steel-pipe pile, F_R is approximately 130 tons as compared with calculated values of 125 and 130 tons and a field-test value of 140 tons.

The area under a force-displacement curve represents the work done by the interaction force on the hammer-pile-soil system. In order to evaluate the transfer of energy between the hammer and the pile-soil system, the work done by the interaction force must be compared with the rated energy output of the hammer. Table 2 gives a tabulation of the percentage of energy transferred for a variety of piles driven by a Link Belt

TABLE 2

ENERGY TRANSFER FOR PILES DRIVEN BY LINK BELT 520

Pile	Rated Hammer-Energy Output (ft-lb_f)	Work Obtained By Integration of Force-Displacement Curve[a] (ft-lb_f)	Approximate Energy Transfer (percent)
Watertown west, wood	19,500	19,400	99
Watertown east, wood	13,700	12,850	94
Watertown, octagonal concrete	21,200	20,295	96
Watertown, steel pipe	17,700	17,575	99
Madison, wood	17,700	17,570	99

[a]Integration performed on compressive force portion of force-displacement curve.

520. Within the accuracy of the dynamic measurements of force and displacement as functions of time, the transfer of energy from the hammer to the pile-soil system appears to be in the order of 94 to 99 percent.

Analog-Computer Simulation of a Hammer-Pile-Soil System

Employing the premise that the linear impulse is equal to the change in linear momentum of a mass over a time interval, we may write

$$\frac{d(KE)}{dv} = \int_{t_1}^{t_2} \left[F_0 \sin(\omega t) - F_R - \frac{d(PE)}{du} - \frac{d(DE)}{dv} \right] dt \qquad (24)$$

where u(t) and v(t) are the instantaneous displacement and velocity respectively of the "rigid" pile. The quantity $[F_0 \sin(\omega t) - F_R]$ may be regarded as the generalized external force acting on the pile. By substitution of Eq. 2 into Eq. 24, we have after some simplification

$$M(d^2u/dt^2) + c(du/dt) + ku + F_R = F_0 \sin(\omega t) \qquad (25)$$

k may be regarded as a constant that represents the total elastic features of the hammer-pile-soil system, and c is a viscous damping constant for the soil. If the load-bearing capacity term F_R is considered to be analogous to friction at the soil-pile interface, then no pile motion can occur until the forcing function $F_0 \sin(\omega t)$ is equal to F_R; i.e., for $F_R = F_0 \sin(\omega t)$, we must have $u(t) = v(t) = 0$. If we assume that F_R and F_0 are related by Eq. 13, then the initial conditions on Eq. 25 are

$$u(t) = v(t) = 0 \quad \text{for } 0 \le t \le \tfrac{1}{\omega} \sin^{-1} (\pi/8) \qquad (26)$$

Inspection of Figures 2 through 5 reveals that this initial condition is indeed quite realistic; i.e., pile displacement is not initiated until the value of the forcing function exceeds $\pi F_0/8$.

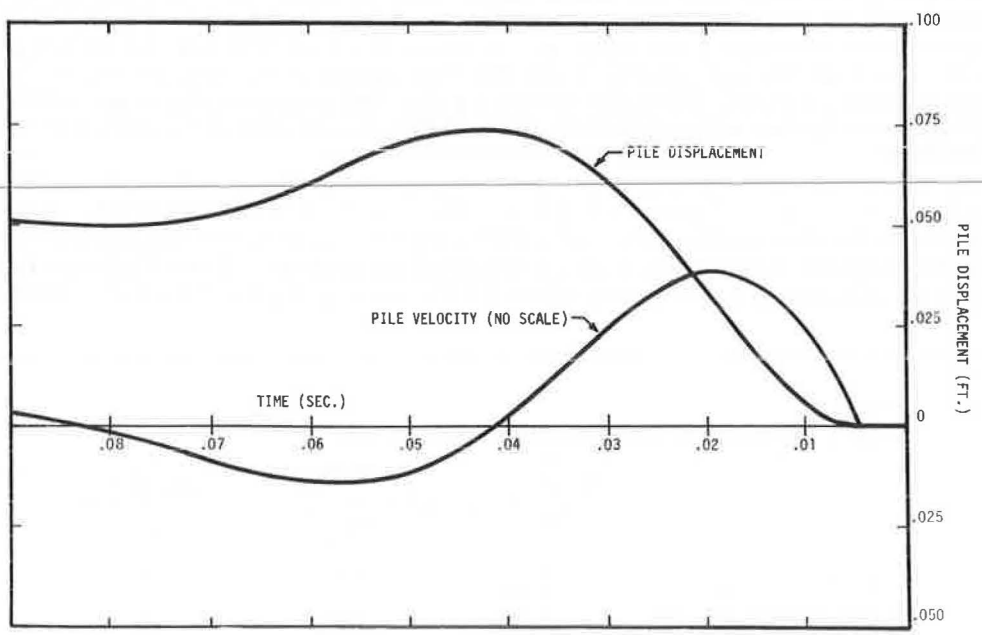

Figure 10. Displacement-time curve obtained by an analog simulation of a Douglas fir pile driven by a Link Belt 520 at the Madison field site.

The second-order, ordinary linear differential Eq. 25 governing the pile displacement can be adapted for solution to an analog computer, wherein the initial conditions (Eq. 26) are utilized. As an example, consider the 30-ft Douglas fir pile at the Madison site. From Figure 5, we obtain F_0 = 560,000 lb_f and ω = 63 cps. In addition, we take $W_p + W_H$ = 8,855 lb and $F_R = (\pi/8) F_0$ = 219,910 lb. According to data shown in Figure 5, a maximum displacement of u_0 = 0.0734 ft occurs at time t_2 = 0.04 sec. The values of the elastic and viscous constants, i.e., k and c, can be varied until the proper values of u_0 and t_2 are obtained. In this manner, a displacement-time curve for the pile can be determined. A comparison of the "theoretical" curve shown in Figure 10 with the experimental curve shown in Figure 5 reveals quantitative as well as qualitative similarities; the simulation appears to be relatively realistic, especially with regard to the permanent pile displacement. For this particular field example, the elastic and viscous constants were found to be k = 1,127,500 lb_f/ft and c = 192,500 lb_f-sec/ft.

The simulation assumes in effect that the pile behaves as a rigid body as it is displaced into the soil. This assumption is reasonably valid if Young's modulus of elasticity between the soil and the pile is approximately a factor of ten, with the pile having the larger numerical value. The elastic constant k is essentially representative of the elasticity of the soil.

CONCLUDING REMARKS

The primary purpose of this study has been to develop a predictive estimate of the "static" load-bearing capacity of a pile on the basis of "dynamic" information obtained during the driving process. By assuming that a pile behaves as a rigid body during the driving process and by neglecting the inertial force, we found the load-bearing capacity to be equal to the centroid (along the force axis) of the hammer-pile-soil interaction force-time curve; this force-time relationship is determined by means of a load cell situated between the hammer and the top of the pile. A subsequent analysis, involving the energy output of the hammer and the maximum pile displacement, includes the inertial effect and yields a more accurate estimate of the load-bearing capacity. The values calculated from both analyses for full-scale piles are found to be in good agreement with static-load test results. In view of the relative simplicity of the theoretical considerations, the quantitative comparison between the calculated and measured values of load-bearing capacity is indeed quite satisfying. Additional verification of the calculated capacities is obtained from dynamic force-displacement curves as constructed from force-time and displacement-time records.

Because the area under a force-displacement curve represents the work done on the entire system by the interaction force, an evaluation of the energy transfer from the hammer is possible. On this basis, approximately 95 percent or more of the rated energy output of the hammer is transferred to the pile-soil system. This energy-transfer percentage is considerably higher than previously anticipated.

Through the use of an analog computer, the simulation of a hammer-pile-soil system is possible. The particular model considered in this study includes the viscous behavior of the soil and the gross elastic features of the entire system. Employing a matching procedure, we can obtain pile displacement-time curves with reasonable quantitative accuracy with regard to comparison with full-scale pile data.

In summary, the primary accomplishments of this investigation have been (a) to develop relatively simple but accurate methods of predicting the static load-bearing capacity of a pile on the basis of dynamic information obtained during the driving process; (b) to demonstrate that the energy transfer from the hammer to the pile-soil system is of the order of 95 percent or better; and (c) to provide preliminary insight into the model simulation of a hammer-pile-soil system on an analog computer.

ACKNOWLEDGMENTS

This investigation was undertaken in cooperation with the Federal Highway Administration. A special acknowledgment is made to W. W. Grimes, formerly of the South Dakota Department of Highways, for his efforts in initiating the pile-bearing capacity study and interest in continuation of the project to a successful conclusion. The

opinions, findings, and conclusions expressed in this paper are those of the authors and not necessarily those of the Federal Highway Administration.

REFERENCE

1. Scanlan, R. H., and Tomko, J. J. Dynamic Prediction of Pile Static Bearing Capacity. Jour. Soil Mechanics and Foundations Div., Proc. ASCE, Vol. 95, No. SM2, March 1969, pp. 583-604.

DISCUSSION

G. G. Goble and Frank Rausche, Case Western Reserve University, Cleveland, Ohio

The authors are to be complimented for the work presented and particularly for the dynamic measurements made on load test piles. So far as the writers are aware, this work represents the first application of analog magnetic tape for recording pile dynamic measurements.

Questions do arise regarding the accuracy of the force measurements due to the presence of tension forces at the end of the record. The authors indicate that this portion of the record should be disregarded. It is possible to hypothesize on the reasons for this tension force. However, any possible explanation will imply as a consequence that earlier portions of the record are also in error. It is also observed that the rise time on the force records is very slow particularly when compared with the records given in a Michigan report (2). It would be expected that the force records obtained by the South Dakota researchers would resemble those obtained in Michigan (2) because of the similarity of the force transducer and driving assembly. Furthermore, because the pile force is proportional to the velocity, this implies that the peak force is dependent on the hammer velocity and not on the pile resistance. This is counter to the resistance prediction given by Eq. 22.

It is noted that the results given in Table 2 show a variety of values for the rated energy for a single hammer, the Link Belt 520. It is assumed that these values are obtained from measurements of the bounce chamber pressure. When they are compared with the manufacturer's rating, they are similar to those reported by others.

Reference

2. A Performance Investigation of Pile Driving Hammers and Piles. Michigan State Highway Commission, Lansing, March 1965.

AUTHORS' CLOSURE

The authors would like to thank Goble and Rausche for their comments concerning the paper. With regard to the accuracy of the force-time measurements, attention is directed to the records shown in Figures 4 and 5. The force-time trace shown in Figure 4 was recorded at a high sensistivity level on the magnetic tape unit. As a consequence of the hammer spike after the pulse maximum, the FM amplifier on the recorder was overloaded, whereupon the remainder of the trace was distorted. The force-time trace shown in Figure 5 was recorded at the correct sensitivity level. By comparison, the only significant difference in form of the 2 pulses occurs after the hammer spike. In particular, the tensile forces shown in Figure 5 are noticeably absent. As a consequence, the authors do not feel that the portions of the force-time records shown in Figures 2, 3, and 4 prior to the hammer spikes are in error. It is not unreasonable to expect a tensile force in the later portion of the records, because of the physics of

the composite hammer-pile-soil system; however, it is felt that the tensile forces should be negligible as compared to the compressive forces, as indeed is shown in Figure 5. In addition, the rise times of the force records shown in Figures 2, 3, and 4 are comparable with the rise times of the force-time traces obtained with an oscilloscope by the investigators in Michigan (2). However, the majority of the force-time traces they illustrate were graphically constructed from hand-digitized data obtained from oscillograph records. By comparison with these traces, the rise times of our force-time records are indeed slow. Consideration must also be given to the improvement in the recording system used to obtain our data as compared to the system employed by the investigators in Michigan. Because of the nature of the instrumentation system, the authors are of the opinion that careful consideration should be given to the use of the dynamic data given in the Michigan report as a standard or a reference frame for the evaluation of the results of subsequent investigations.

On physical grounds, it is certainly plausible to expect that soil behaves in a viscous fashion during loading. As a consequence, the resistive force of the soil on the pile is dependent on the velocity of the pile as indicated in Eq. 1. In the derivation of Eq. 22, the assumption is made that the behavior of the pile-soil system during dynamic loading is analogous to that of a damped simple harmonic oscillator. At the instant of maximum pile displacement, the pile velocity is zero and the pile acceleration is a negative maximum. Because the calculation of the pile-bearing resistance is made at the instant of maximum displacement, the viscous contribution in the force balance on the system is zero. With reference to this condition, the energy required to permanently displace the pile into the soil is the difference between the rated output energy of the hammer and the energy required for simple harmonic motion of the pile. This energy difference is related to the work done by the hammer-pile-soil system interaction force and the pile resistive force. The interaction force is measured by means of a load cell situated between the hammer and the top of the pile. Because the interaction force is effectively measured internally within the hammer-pile-soil system, it must reflect the elastic characteristics of the entire system, as well as the viscous nature of the soil resistance to pile motion.

COMPARISON OF SINGLE- AND MULTIPLE-UNDERREAMED BORED PILES BASED ON LABORATORY AND FIELD EXPERIMENTS

M. Barrett Clisby, Mississippi State University, State College; and
Robert M. Mattox, Mississippi State Highway Department, Jackson

Bored piles are used extensively to meet foundation requirements in some soils. The maximum diameter of the belling tool for underreaming is limited to approximately 3 times the diameter of the shaft. This limitation causes an uneconomical design in some soils because of the resulting low stress in the concrete of the shaft. An increase in the area of that portion of the pile in point-bearing increases the bearing capacity of the pile. A method of increasing this effective area is to cut a bell at other locations along the shaft of the pile, in addition to the bell at the point. This paper describes the laboratory and field tests that were performed so that the load-carrying capacity of single- and multiple-underreamed bored piles could be determined. Bell spacings and failure planes in the soil of the model piles were studied extensively. The results of the model tests were used in the test design of the field piles. An analysis of all field test results was made by using the full area of both the bell in point-bearing and perimeter of the shaft in skin friction. Calculated load-deflection behavior using these assumptions compare reasonably well with the load-deflection values obtained by experimentation. Multiple belling of cast-in-place piles can result in economical designs for many soil conditions.

•STRUCTURAL foundation requirements for many soil conditions are satisfied by the use of cast-in-place concrete piles. Enlarging the bottom of the pile by underreaming or belling is one method of increasing the point resistance. The maximum diameter to which a bell can be cut is limited to approximately 3 times the diameter of the shaft because of size limitations of the belling tool. Many designers neglect the skin friction of belled piles; the resulting designs often involve shafts so large that the maximum stress in the concrete is less than 10 percent of the ultimate stress. This is uneconomical design because of the additional cost of excavation and concrete. Because it is nearly impossible to increase the shear strength of the soil, the alternative is to increase the relative areas of point to shaft of the pile. One method of accomplishing this is to underream at other elevations along the shaft in addition to the point as shown in Figure 1. This paper describes the laboratory and field tests that were performed so that the load-carrying capacity of various types of bored piles could be determined.

LABORATORY TESTS

Laboratory tests were conducted on models to determine the relative bearing capacities of the single- and double-bell piles. The top bell of the model could be moved along the shaft so that bell spacing could be varied. The model pile consisted of a 1-in. diameter steel shaft with a $2\frac{1}{2}$-in. diameter steel bell or bells. The material used for the soil was a mixture of ground, oven-dried Yazoo clay with 20 percent petroleum jelly

Sponsored by Committee on Foundation of Bridges and Other Structures.

added to replace the moisture and make the clay workable. This material remained consistent throughout repeated uses during the testing program. Static compaction yielded a material of constant density on which triaxial compression tests were run to determine the cohesion and friction angle. Load deflection curves were plotted from the data obtained from all model pile tests. The ultimate bearing capacity of each model pile was defined by using the tangent method. Table 1 gives the results of the average of 3 tests for each bell spacing.

Figure 2 shows a plot of the results given in Table 1. The double-bell pile produced a maximum increase of 48 percent in ultimate capacity over the single-bell pile. The optimum spacing between the bells of the double-bell pile corresponding to this maximum increase was found to be equal to, or greater than, 2 bell diameters.

After approximately 1-in. total deflection of the pile, the soil was carefully removed to allow visual observation of the failure planes that developed during the test. Figure 3 shows a typical failure surface obtained upon complete failure of the double-bell pile with 1.2- and 1.6-bell diameter spacings. It is evident that the increase in ultimate capacity of this pile is derived from the cylindrical shearing pattern that develops between the 2 bells. This cylinder is approximately equal in diameter to the diameter of the bells.

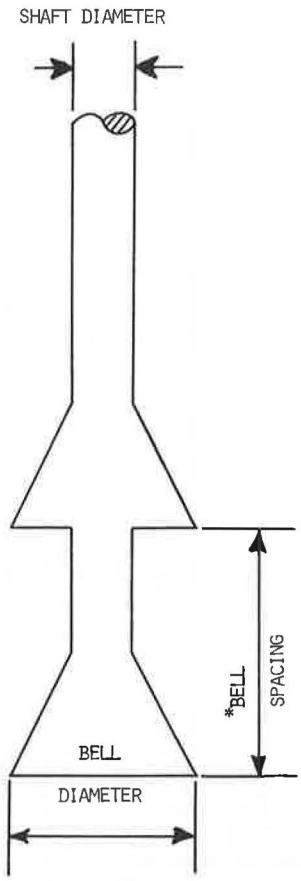

Figure 1. Double-bell pile.

Figure 4 shows a failure surface for one of the tests using a 2.0-bell diameter spacing. It appears that the 2.0-bell diameter spacing is the transition between the cylindrical shearing pattern and the pattern shown in Figure 5. The failure surfaces shown in Figures 5, 6, and 7 are typical of the bearing capacity failures derived by Prandtl, Terzaghi, and others. Therefore, the additional capacity of the double-bell pile using 2.4- and 2.8-bell diameter spacings is derived from the point-bearing capacity of the top bell.

The results obtained from the model tests indicated a sufficient increase in the capacity of a multiple-bell pile to justify conducting a series of full-sized pile tests.

TABLE 1

ULTIMATE CAPACITY OF MODEL TEST PILES

No. of Bells	Bell Spacing (diameter)	Load (lb)	Percent Increase
1	—	6,640	—
2	1.2	7,860	18.4
2	1.6	8,900	34.0
2	2.0	9,830	48.0
2	2.4	9,830	48.0
2	2.8	9,830	48.0

FIELD LOAD TESTS

The site selected for the field tests was on the right-of-way of Interstate 220 in the northwest section of Jackson, Mississippi. Soil borings and subsequent laboratory tests indicated the following: the top 18-ft is a stiff, brown, silty clay; the next 12 ft is a stiff, tan, highly desiccated, weathered Yazoo clay; and the next 30 ft is a hard, blue, unweathered Yazoo clay. The soil investigation terminated

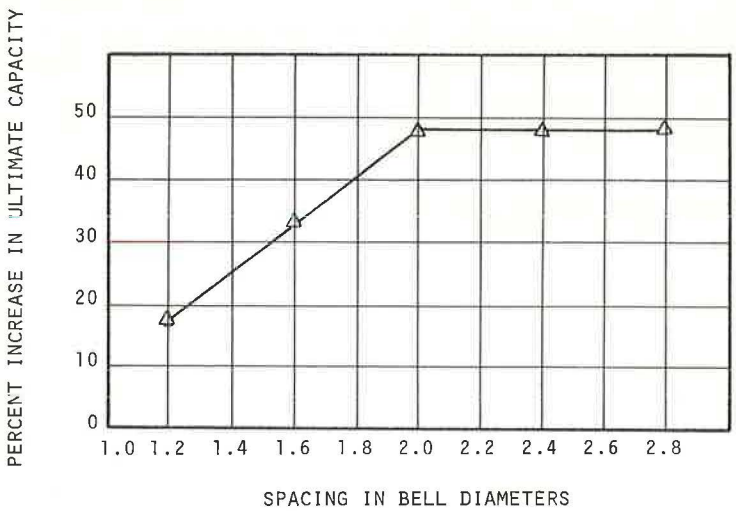

Figure 2. Increase in ultimate capacity of double-bell model piles over single-bell model piles.

at a depth of 60 ft. Figure 8 shows the plan view of the test site and the location of the test piles, the reaction piles, and the borings. Repetitive triaxial and direct shear tests were run on the undisturbed soil samples at approximately 5-ft intervals for the full 60-ft depth. Figure 9 shows a typical boring log on which cohesive shear strengths are graphically presented.

Fifteen piles were cast: 7 test piles and 8 reaction piles. Figure 8 shows that the geometrics of the layout were based on the maximum utilization of each reaction pile. The reinforcing steel in each reaction pile was arranged in such a manner that the piles could be used for 2 or more load tests. Each reaction pile was structurally designed to carry the predicted ultimate failure load of the test pile. All piles were cast of 5,000 psi concrete. The test piles had a shaft diameter of 12 in. and contained four No. 8 bars to their full depths except that pile 13 contained seven No. 11 bars to its full depth. Table 2 gives the physical properties of the test piles and the steel in each.

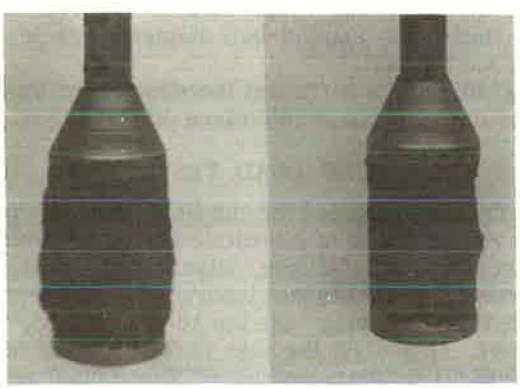

Figure 3. Failure patterns for double-bell piles with 1.2- and 1.6-bell diameter spacing.

Figure 4. Failure pattern for double-bell pile with a 2.0-bell diameter spacing.

Figure 5. Failure surface for 2.4-bell diameter spacing.

Figure 6. Failure surface for 2.8-bell diameter spacing.

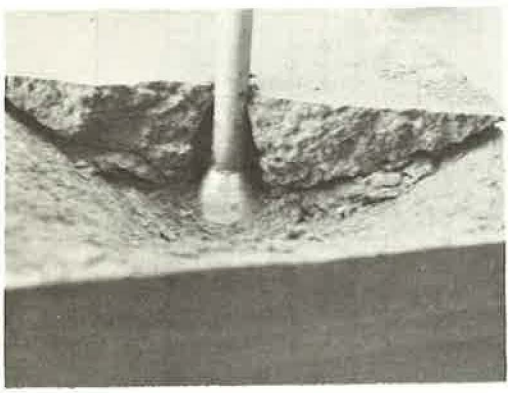

Figure 7. Failure plane for top bell for a 2.8-bell diameter spacing.

Each reaction pile as constructed with a 24-in. diameter shaft, 60-in. diameter bell, and 32-ft embedment. Figure 10 shows the profile of a typical loading arrangement.

Construction of the test piles began June 25, 1969, and was completed July 1, 1969. Construction of bored piles consisted of drilling the shaft with an auger to the desired tip elevation; the auger was then removed and the belling tool was lowered to form the bell. The cutting blades were activated by the weight and force of the drill stem that caused the blades to swing out and gradually cut the bell. The double-bell pile was constructed by advancing the shaft to the elevation of the base of the top bell; the belling tool was then used for con-

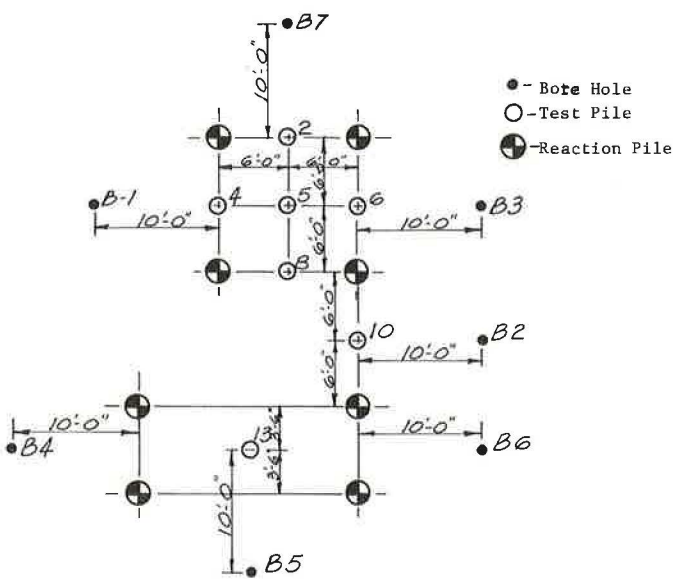

Figure 8. Test pile and boring location plan.

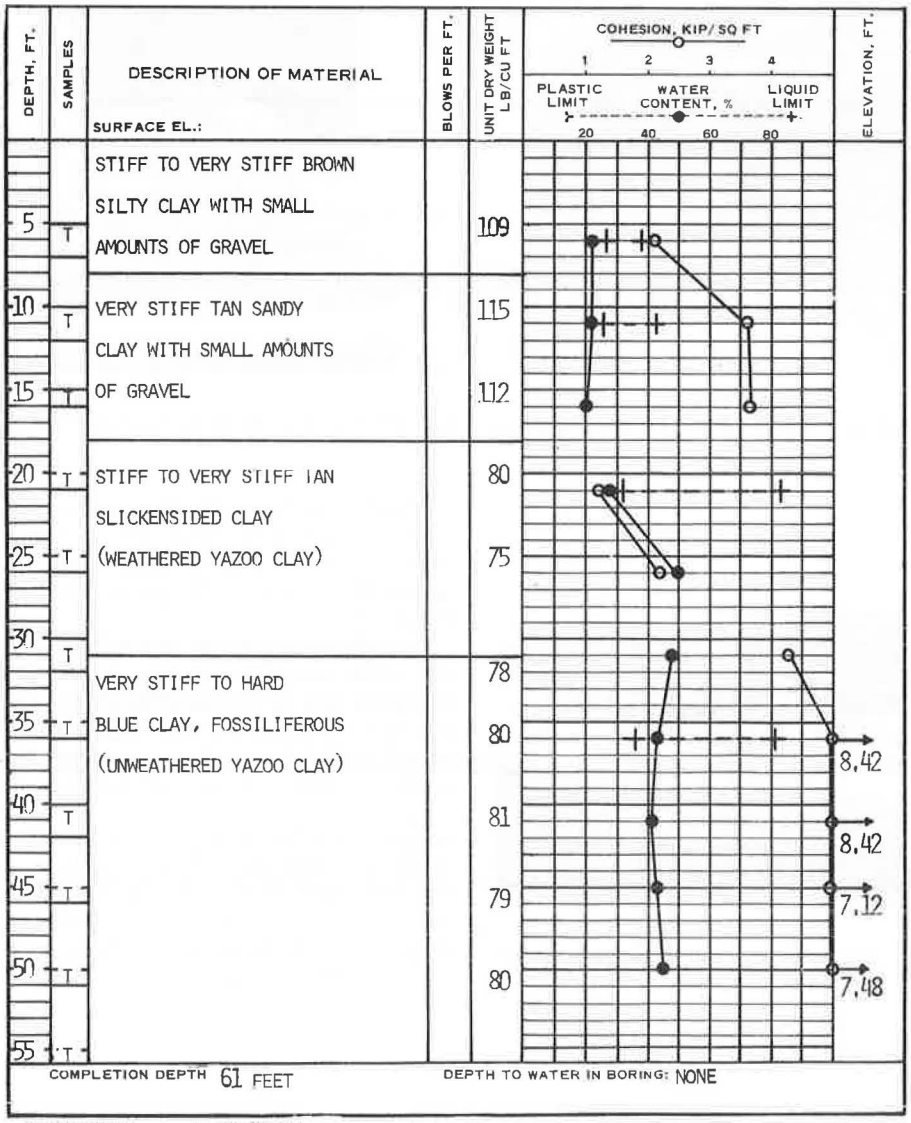

Figure 9. Typical boring log.

TABLE 2
SUMMARY OF TEST PILE DESIGNS

Pile	Shaft Diameter (in.)	No. of Bells	Embedment Length (ft)	Steel Bars	Ties
2	12	1, 36 in.	39	4, No. 8	No. 3 at 12 in.
4	12	2, 24 in. at 4 ft	39	4, No. 8	No. 3 at 12 in.
5	12	No point	37	4, No. 8	No. 3 at 12 in.
6	12	2, 24 in. at 8 ft	39	4, No. 8	No. 3 at 12 in.
8	12	Straight shaft	39	4, No. 8	No. 3 at 12 in.
10	12	1, 24 in.	39	4, No. 8	No. 3 at 12 in.
13	12	2, 36 in. at 4 ft	38.5	7, No. 11	No. 3 at 6 in. for top 6 ft and 3 at 12 in. lower 6 ft

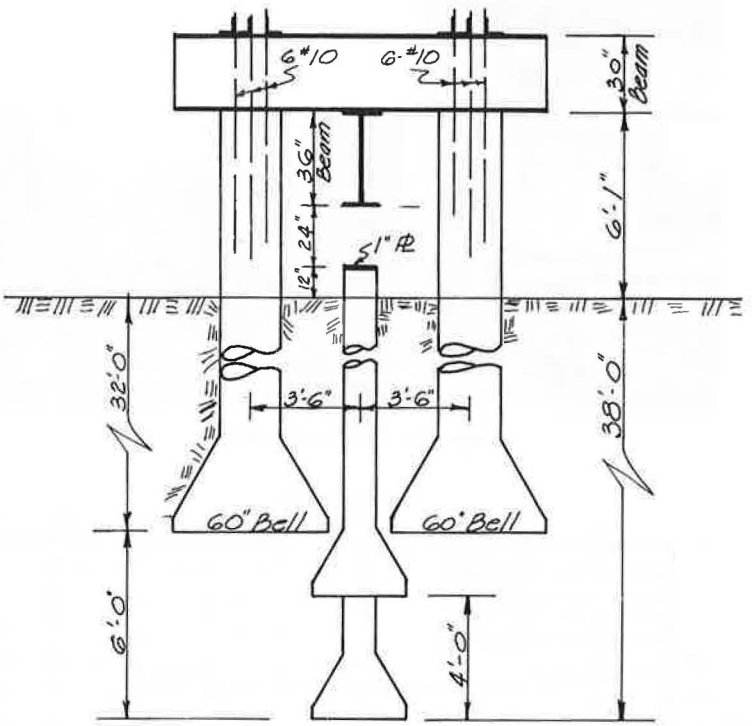

Figure 10. End profile of loading arrangement on pile 13.

struction of the top bell. The shaft was advanced to the elevation of the bottom bell, and then the bottom bell was reamed. The reinforcing steel then was placed, and the concrete was poured into the shaft, vibrated to eliminate voids, and finished at cutoff elevation.

The reference frame for measuring pile deflections was constructed of aluminum beams. Dial gages calibrated in 0.001 in. were used to measure the deflections. The loads were applied and maintained with a hydraulic jacking system. Figure 11 shows the load test on pile 13 in progress.

The approximate ultimate load capacity of each pile was computed, and the test loads were applied in increments of 25 or 50 kips, depending on the predicted ultimate load for each test pile. For each increment of loading, time-deflection readings were recorded at 0, 1, 2, 4, 8, and 15 and every 15 minutes thereafter for the duration of the loading increment. Each load was maintained until the deflection substantially ceased, or until at least 3 points formed a straight line in the lower portion of the time curve. Figure 12 shows the results of the time-loading data for pile 8. These results are typical for all piles tested.

Based on the time deflection data, equilibrium points for each loading increment were defined. These load deflection data for each test pile are given in Table 3.

ANALYSIS OF DATA

All piles, regardless of pile material, size, or shape, depend on both point-bearing and skin friction for their load-carrying capacities. However, many designers sometimes neglect either one or the other of these 2 components, depending on soil conditions or pile type. For comparative analysis of the capacity of the piles in this investigation, both components were used.

The computed load deflection values were determined by an iteration process, which accounts for the deformation of the pile itself. For computational purposes, each test

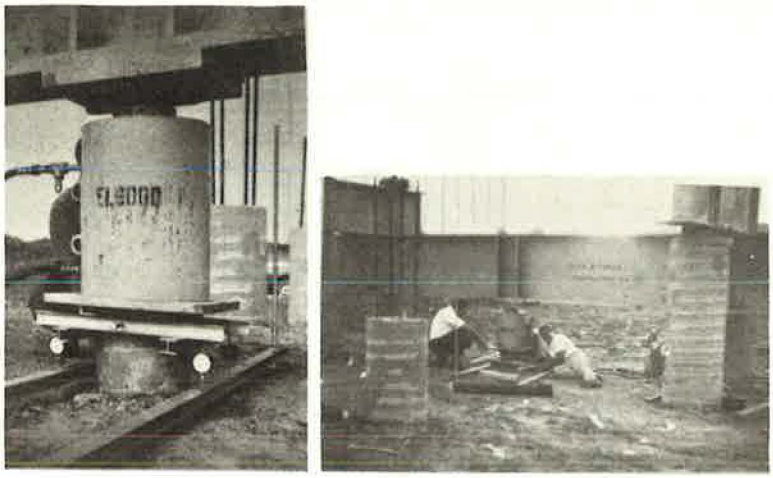

Figure 11. Field loading test.

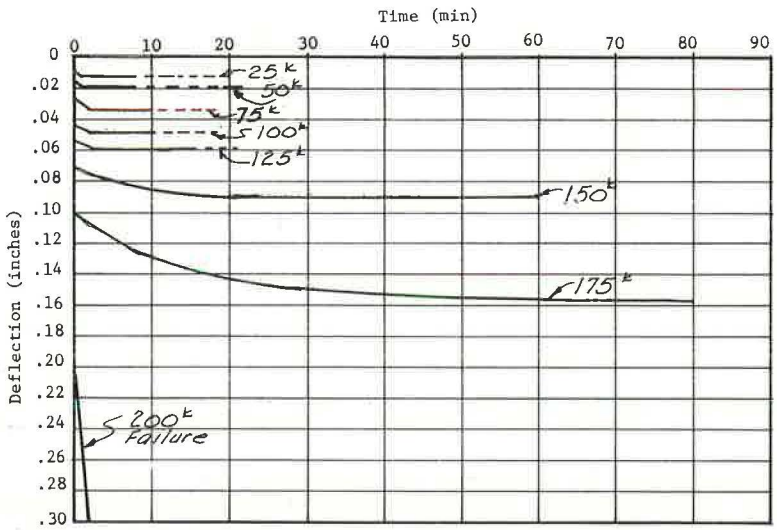

Figure 12. Time-deflection values for pile 8.

TABLE 3

TEST PILE DEFLECTIONS

Load (kip)	Pile 2	Pile 4	Pile 5	Pile 6	Pile 8	Pile 10	Pile 13
0	0	0	0	0	0	0	0
25			0.011		0.011	0.010	
50	0.017	0.016	0.026	0.018	0.018	0.020	0.019
75			0.039		0.034	0.029	
100	0.041	0.039	0.062	0.058	0.046	0.038	0.039
125		0.051	0.185	0.111	0.060	0.069	
150	0.072	0.110	1.809	0.491	0.088	0.149	0.069
175		0.269		1.143	0.159	0.329	
200	0.144	0.502		1.964	0.962	0.542	0.135
225	0.218	0.751				0.766	
250	0.351	1.005				1.006	0.247
275	0.640						
300	0.987						0.419
325	1.343						
350	1.678						0.593
375							
400							1.049
425							
450							1.664
475							2.025
500							2.490

Note: Values are in inches.

pile, excluding pile 13, has a transformed section area of 128 sq in. and perimeter of 37.7 in. Pile 13 has a transformed section area of 168 sq in. The modulus of the concrete was taken as 1,000 f'_c or 5,000,000 psi. This value is very close for the range of stresses applied to the top of the pile during testing.

The determination of the relationship between the point-bearing and point deflection utilized the undisturbed triaxial test results of the undisturbed sample nearest the pile tip. The confining pressure was taken as equal to the overburden pressure at the tip and the point stress as equal to the deviator stress. These values were substituted in the elastic deformation equation to obtain the final results. The relationship between skin friction force and deformation was computed by utilizing the remolded direct shear test results. The direct shear tests were run with the normal stress equal to the overburden stress at the location at which the sample was taken. The variation of shear stress on the face of the pile was assumed to be linear among soil sample locations. It was also assumed that the full shear strength of the soil was developed between the soil and the face of the pile, i.e., no reduction was made for adhesion.

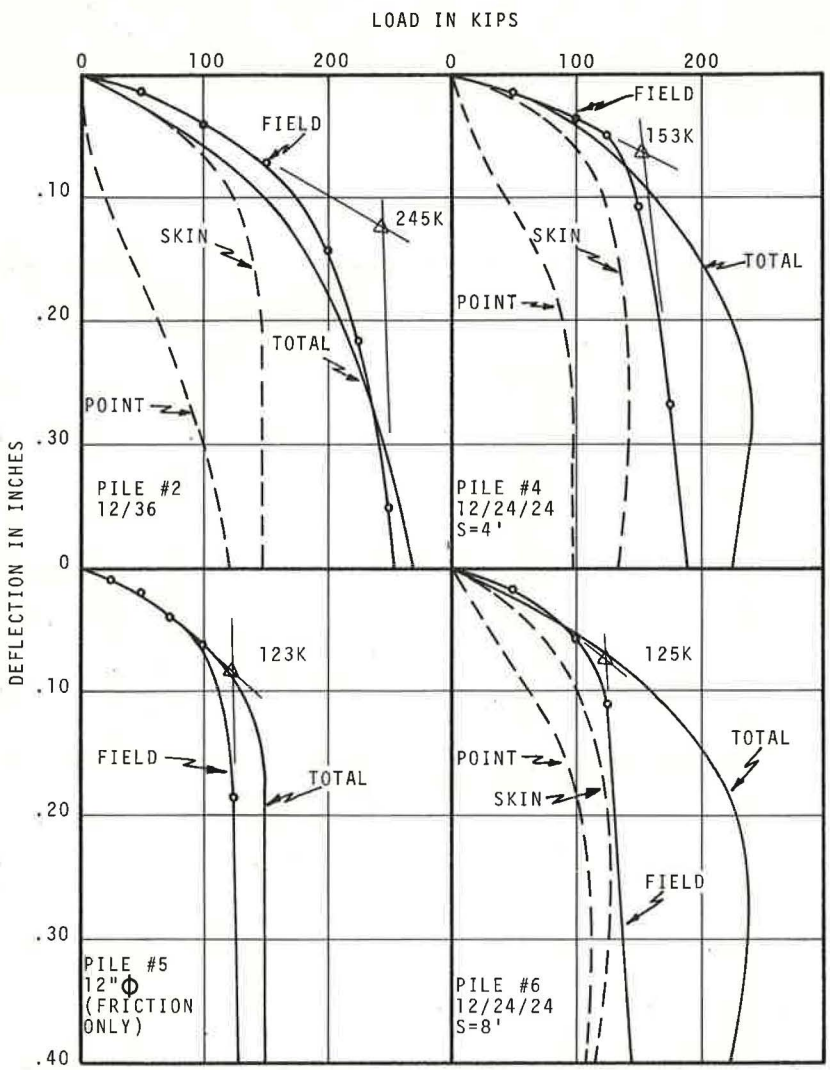

Figure 13. Computed and measured load deflection curves for piles 2, 4, 5, and 6.

Test pile 5 was cast on top of a 1-ft thick spacer that eliminated the point-bearing; therefore, only the skin friction was used to compute its bearing capacity. Test pile 8 was a straight shaft with end-bearing. The bearing capacity of this pile was computed by adding the point-bearing for the 12-in. diameter point to the skin friction for the entire length of the pile. The capacity of each single-bell pile, 2 and 10, was computed by using the area of the point and the skin friction from the top of the bell to the surface of the ground. The capacity for each double-bell pile was computed by using the point-bearing of both bells, the skin friction between the 2 bells, and the skin friction from the top of the upper bell to the surface of the ground. It is recognized that slightly different capacity values could be obtained with different assumptions.

Figures 13 and 14 show both the computed values and the field test results. On these figures, the computed values have been divided into the components of point-bearing and skin friction for study convenience. The dashed lines are the components, while the solid line is the sum of the 2 values. The field test results are shown as open points.

The ultimate capacity of each test pile was determined by the tangent method. These results are shown in Figures 13 and 14 as triangles.

The iteration method, which was used to determine the theoretical loading deflection curves, agreed well with the load test results throughout the elastic range of deflection. The theoretical and field curves began to diverge in the plastic range of deflection.

A comparison of the ultimate capacities of pile 2 (12/36) and test pile 13 (12/36/36) shows an increase of 47 percent. Therefore, a significant increase in ultimate capacity was realized by the addition of the second bell.

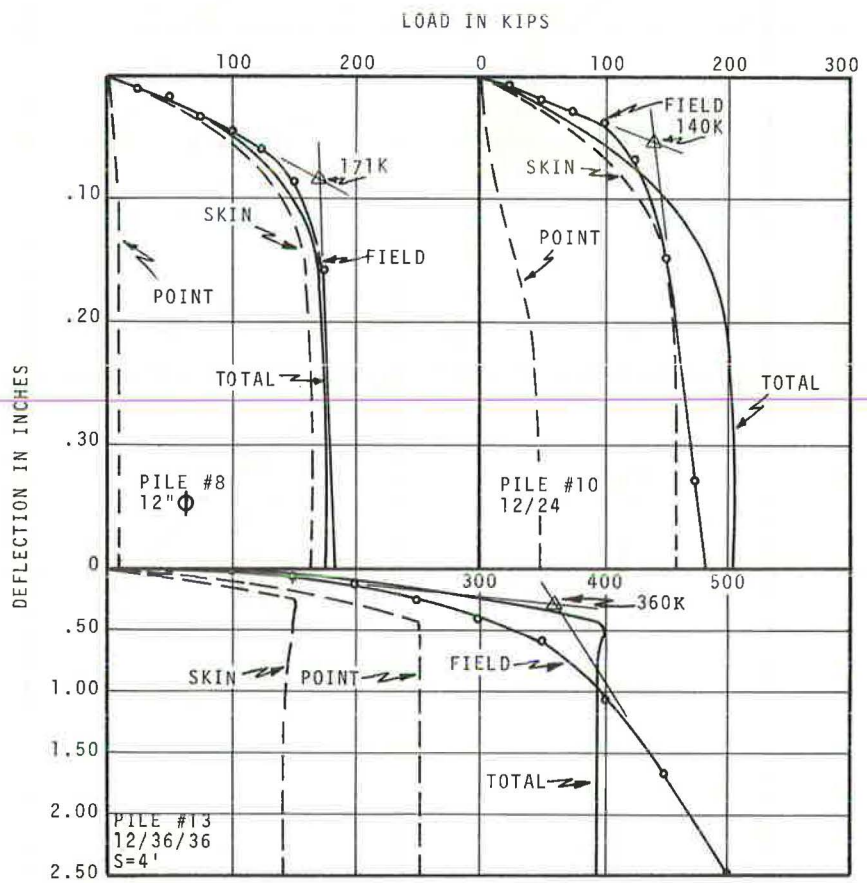

Figure 14. Computed and measured load deflection curves for piles 8, 10, and 13.

The ultimate capacities of all test piles having 24-in. bells fell in the range of 125 to 153 kips. These capacities are considerably lower than the 171-kip ultimate capacity of the straight shaft test pile (pile 8). It appears that the use of small bell-to-shaft ratios, in this case 2:1, may be detrimental to the ultimate capacity of the pile. Additional research must be conducted to properly evaluate this phenomenon.

SUMMARY

Because of the scope of this pilot research project, no firm conclusions can be drawn at this time. From the foregoing presentation, however, the following observations are made:

1. The assumptions made in calculating the bearing capacity of the piles seem to be reasonable. However, the relative accuracy of computation of the straight shaft with point-bearing as compared to the bell piles indicates that a better relationship would result with different assumptions. It appears that the belling operation alters the effect of skin friction for some distance above the top of the bell. This effect could be the result of prestressing the soil above the bell by the hydrostatic force of the concrete prior to hydration.
2. The remolded strength of the clay should be used in determining the frictional component of cast-in-place piles as it is for other piles. This remolded strength allows for disturbance caused by the auger and the increase in moisture content of the soil in contact with the wet concrete.
3. The 24-in. diameter bell on the 12-in. shaft did little to improve the capacity; in fact, it appears that this small ratio of bell-to-shaft diameter may be detrimental to the ultimate capacity of the pile.
4. For the category of piles having a bell-to-shaft ratio of 3:1, an increase of 47 percent in ultimate capacity was realized by the addition of the second bell. This increase in capacity, considering the small cost of the additional bell, points out that the double-bell pile may be a very economical design. Based on the knowledge of the shear patterns that were developed during the model test phase of this project, it appears that the only limitation on pile capacity is the number of bells that could be placed along the pile shaft.
5. It is recommended that additional research be conducted to fully develop design criteria for this type of pile.

ACKNOWLEDGMENTS

In addition to equipment and personnel furnished by Mississippi State University and the Mississippi State Highway Department, the work accomplished in this investigation was supported as follows: Hart-McCowan Foundation Company constructed all test piles, reaction piles, and reaction beams; Stanley M. Hart, E. H. Gabriel, and H. K. Davis provided engineering consultation; Jackson Ready Mix Concrete, Division of Delta Industries, furnished concrete; Mississippi Steel, Division of Magna Corporation furnished steel; C. & H. Steel Company furnished tying steel; and Anslem H. Barber, Jr., provided portions of model test results from his master's thesis.

FIELD MEASUREMENTS ON INSTRUMENTED PILES UNDER AN OVERPASS ABUTMENT

N. D. Nicu, New Jersey State Department of Transportation;
D. R. Antes, formerly King and Gavaris Consulting Engineers; and
R. S. Kessler, King and Gavaris Consulting Engineers

The usual design procedure for piled bridge abutments over thick deposits of soft compressible soils has been to consider only those forces acting above the footing level. Several structures have experienced large horizontal movements resulting in damage to the structure because of the shortcomings in the conventional design procedures. For this reason, a bridge abutment on Interstate 80 in New Jersey was instrumented to determine its behavior and to provide a clearer definition of the problem. The instrumentation installed on a pile-supported abutment is described, and suggestions are made regarding some improvement for possible future field research. Qualitative results were in accordance with the anticipated behavior of the soil-pile system. The results obtained from these field measurements have confirmed that abutments supported on piles driven through soft compressible soils have the tendency to tilt toward the backfill when the shearing strength of these soils was exceeded because of superimposed embankment loads. These findings permit the tentative establishment of limiting values for stresses imposed on compressible layers with relation to the backward tilting of such conventionally designed abutments, and they suggest various remedial measures.

•THE CONVENTIONAL design procedure for bridge abutments supported on piles driven through thick deposits of soft compressible soils is to consider only those forces acting on the abutment above the footing level. These forces usually include only the girder reactions, the weight of the abutment, and the conventionally determined active lateral earth pressure. In some cases, an estimate of the effect of the consolidating strata on the piles in bending is considered (1). The inherent shortcomings of this procedure has resulted in damage to several structures as the abutment tilts back toward the retained fill. In some cases large horizontal movements (as great as 10 in.) have developed, although to the writers' knowledge no catastrophic failures have been recorded (2, 3, 4).

The adequacy of the conventional design procedures was studied by instrumenting a bridge abutment to determine its behavior during and after construction. The instruments were installed on the west abutment of the bridge carrying the eastbound lanes of Interstate 80 over the Lehigh and Hudson Railroad near Allamuchy, New Jersey (Fig. 1). This bridge was chosen because it could safely be designed by conventional methods and, at the same time, provide measurable movements yielding data that would result in a clearer definition of the problem.

A profile including the soil stratigraphy at the Allamuchy site is shown in Figure 2. In general the profile includes approximately 30 ft of embankment over 14 ft of medium, compact silty sand and 44 ft of soft varved clay over very compact sand and gravel. Both the vertical and battered (1:3) piles penetrated approximately 35 ft into the sand

Sponsored by Committee on Foundation of Bridges and Other Structures.

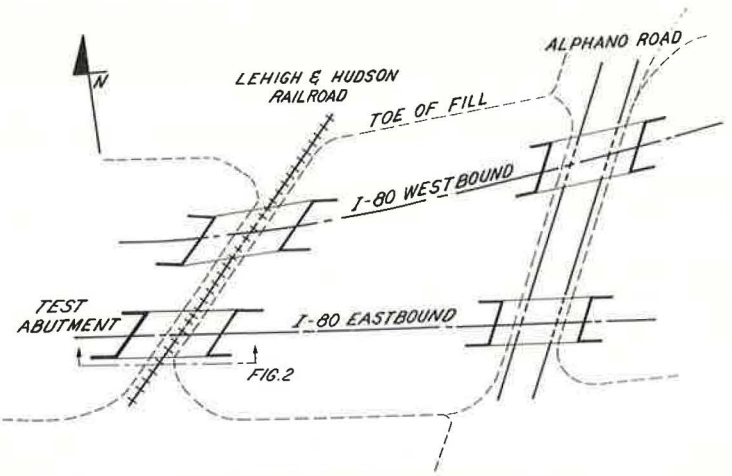

Figure 1. General plan of the Allamuchy site.

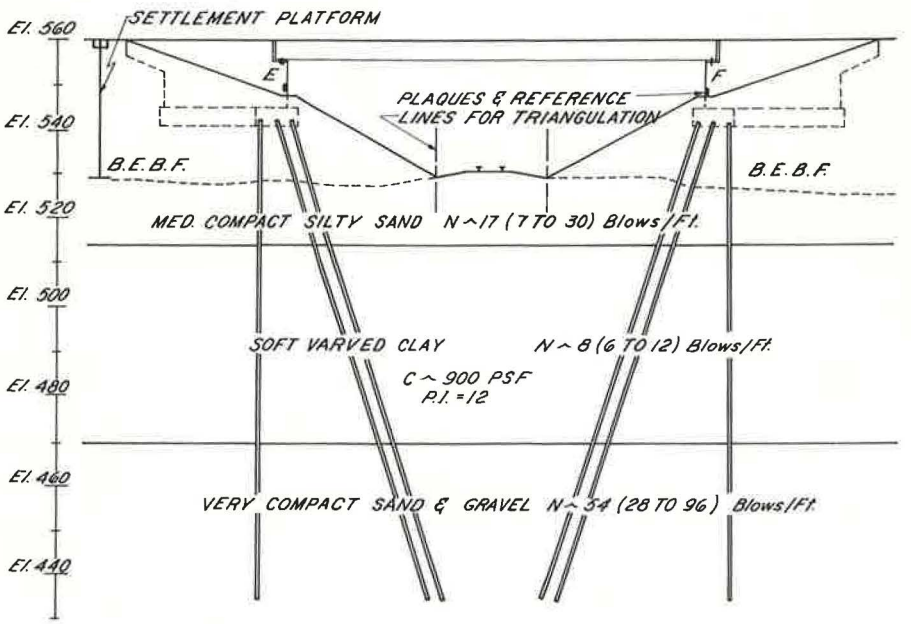

Figure 2. Profile and soil stratigraphy of the Allamuchy site.

and gravel. Steel H-piles (12 BP 53), using a design load of 28 tons per pile, were selected to minimize remolding of the varved clay (sensitivity = 3 to 4).

CONSTRUCTION PROCEDURES

Construction at the Allamuchy site started in May 1969 with the placement of settlement platforms and proceeded through July 1970 when the embankment construction was completed to subgrade elevation. The placement of the subbase and pavement has not yet begun. Additional measurements are planned after these operations are completed. For convenience, the significant events during the construction process have been divided into the following stages (Fig. 3):

0. May 1969, installation of settlement platforms on original ground;
1. July-August 1969, placement of bridge excavation borrow foundation, completion of pile-driving operations, completion of pile load test, and installation of Slope inclinometer guide casings;
2. September 1969, installation of stress and strain meters and pouring of abutment footing;
3. October 1969, completion of construction of abutments;
4. November 1969, placing of approximately 10 ft of embankment and erection of steel girders;
5. December 1969, completion of approximately 14 ft of embankment;
6. April 1970, pouring of bridge deck; and
7. July 1970, completion of embankment construction including all the fill at the east abutment of the test structure.

INSTRUMENTS AND MEASUREMENTS

Six of the piles, 3 vertical and 3 battered, in the test abutment (Fig. 4) were modified to permit measurements of their deflection under load. A 5-in. diameter steel pipe was fillet-welded to each pile through 3-in. slots cut at 1-ft intervals through the web at the neutral axis. The pipe was then cut between each fillet weld into 1-ft segments by means of a carborundum saw and an acetylene torch, so that each 1-ft segment was free to form a tangent to the slope of the deflected pile.

The openings in the pipes caused by slotting were filled with a mastic to prevent soil from entering during driving. The pipes terminated 5 ft above the H-pile tips to eliminate disturbance of the sand and gravel stratum into which the piles were driven. Disturbance of the varved clay, because of the increased cross section, was minimized by jetting with a 2-in. diameter jet pipe inside the 5-in. pipe, with the jetting discontinued when each pile had penetrated a few feet into the supporting sand and gravel stratum. Aluminum casings (3.18-in. outer diameter), supplied by Slope Inclinometer of Seattle, were installed inside the 5-in. pipes after the piles were driven. Ottawa sand filled the annular space between the casing and the pipe. Slope inclinometers (model 200 for

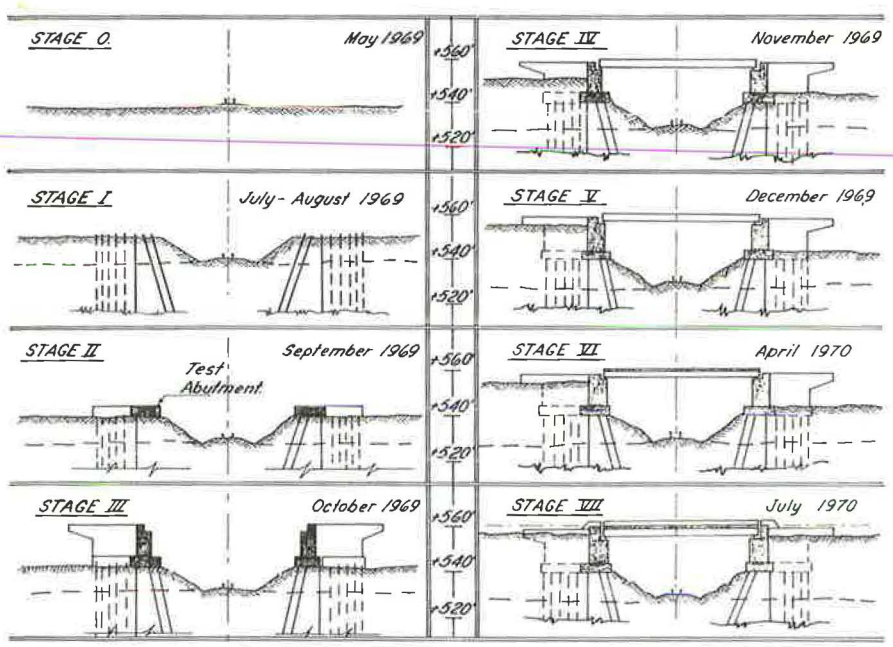

Figure 3. Construction stages.

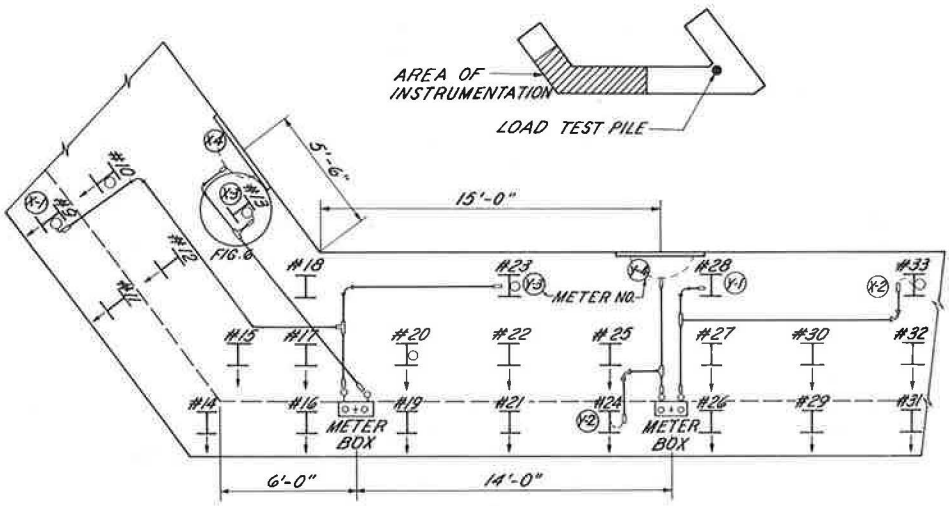

Figure 4. Plan of instrumentation layout.

the vertical piles, and model 225 for the battered piles) were then used to measure the deflection of the piles after they were driven and during their construction.

Each of the 6 piles in the test abutment (Fig. 4) were instrumented with 4 Carlson SA-10 strain meters, one at each edge of each flange. Two of these piles, 1 vertical and 1 battered, did not have Slope inclinometers. The purpose was to determine whether the jetting of the inclinometer-instrumented piles had diminished the pile support capacity of the in situ soils. All strain meters were installed prior to the placement of reinforcement steel.

The stress meter assemblies, consisting of 4 Carlson stress meters (Model PE-10) each, were installed at the back of the abutment and wing-wall pile cap (Fig. 4) to measure the lateral earth pressures. The 4 meters were held in position by a template fastened to the form while the pile cap was poured; and, after the forms were stripped, a 1-in. thick steel plate, measuring $2\frac{1}{2}$ by 4 ft, was placed flush against the surface of each group of 4 meters. Each plate was then suspended by wires fastened to bolts cast in the concrete cap. The plates were otherwise unfastened and free to swing against or away from the stress meters.

All cables from the Carlson stress and strain meters were run through Greenfield and $2\frac{1}{2}$-in. rigid metal conduit within the abutment and wing-wall footing and stem to protect the cables from damage during concreting operations. These cables were terminated in meter boxes, mounted on the face of the abutment, wherein the cables were fastened to Leeds and Northrup decade switches. The stress and strain meter measurements were made by connecting a Carlson testing meter assembly to the Leeds and Northrup switches.

Nine settlement platforms were installed behind the test abutment at approximately the original ground surface elevation, after topsoil and other organic matter were stripped. Settlements of the platforms were measured to 0.001 ft throughout the construction of the bridge by using 3 wire-leveling methods. Readings will be continued after the highway is open to traffic by means of protection boxes placed in the pavement and shoulders into which the settlement platform pipes have been extended.

In addition, several points on each west abutment at both the Lehigh and Hudson Railroad and Alphano Road were surveyed to observe settlements of the structures. Readings were begun on the test abutment immediately after it was constructed, while measurements to obtain correlative data were performed on the other abutments some time after they were constructed.

The horizontal distances between 2 opposing pairs of monuments (Fig. 2) embedded in the faces of the test abutment and the east abutment (eastbound) were measured by

triangulating with theodolites reading directly to 1 second. One reference line and then a second one was established along the railroad tracks (Fig. 1) from which the triangulation was performed.

It was observed that noticeable movement had occurred at the test abutment rockers a short time after the steel girders were placed. Subsequent measurements were performed on the rockers at the west abutments of the Lehigh and Hudson Railroad and Alphano Road structures to determine the magnitude of horizontal movement occurring at the rockers. Measurements consisted of determining the horizontal distance between the rocker key centerline and the vertical plane passing through the rocker pin centerline.

TEST RESULTS

To aid in the reduction of the myriad of field measurements, 3 computer programs were written for this research project: Slope inclinometer data, which output deflection versus depth; Carlson strain meter data, which output values of strain and corresponding stresses; and Carlson stress meter data, which output values of pressure acting on each meter and a coefficient of lateral earth pressure.

By using slope indicator measurements, the as-driven shapes of the 6 inclinometer-instrumented piles were computed and plotted. For the vertical piles, there was very little drift in the direction of their strong axes. However, there was considerable deviation from the vertical, i.e., up to 5ft in a 100-ft long pile, in the direction of weak axes of the piles. These deviations were similar to, and about the same order of magnitude as, those recorded by Hanna (5) for steel piles. In the batter piles, the same general trend to deviate from the design location was observed, but of smaller magnitude. The design batter of 1:3 was never achieved, probably because the piles tended to bend under their own weight, as noted by Bjerrum (6).

Measurements of the 6 piles were made at the various stages of construction described earlier, and the deflections were computed by using the as-driven shape as a "zero deflection" reference. Piles 20, 23, and 33 in the abutment indicated deflections occurring under increasing abutment and embankment loadings in the direction of the strong axes of the piles, away from the embankment. There was virtually no deflection under load in the direction of their weak axes. Piles 9, 10, and 13 in the wing wall indicated that deflections occurred about both strong and weak axes with the resultant of these deflections acting normal to the railroad. Figure 5 for pile 13 shows the deflections computed for the instrumented wing-wall piles. It was hoped that by measuring the deviations of the piles under load, from their as-driven shapes, deflection curves could be obtained from which the coefficient of lateral earth pressure, K, acting against the piles could be computed. Difficulties were encountered in selecting from these deflection curves the end conditions and the effective lengths of the equivalent beams of the piles on which such a coefficient would depend.

The strain meter measurements were used to compute the compressive and tensile stresses acting in the piles immediately below the point of embedment in the footing. These stresses indicated that bending occurred only about the strong axes of the H-piles in the abutment and about both axes of the H-piles in the wing wall. Figure 6 shows the stresses acting in pile 13, which is typical of the wing-wall piles. The bending moments of fixation, computed from the strain meter measurements, for the vertical piles averaged 41 kip-ft. The stresses induced by bending moments of similar magnitude will depend on the types and dimensions of the piles. However, it is evident that piles with low bending strength properties should be avoided.

Figure 7 shows the variation of the coefficient of lateral earth pressure with the construction stages. Before completion of state 4, the coefficient of lateral earth pressure computed from the readings of the abutment stress meter assembly was 0.32 and from those of the wing-wall assembly, 0.58. This high value was attributed to possibly abnormally high compactive effort adjacent to the wing-wall assembly. At the completion of stage 4 of construction, the K-value at both locations was 0.27. With no further increase in load for approximately 6 months, the coefficient of lateral earth pressure decreased to 0.13 and 0.22 for the abutment and wing-wall respectively.

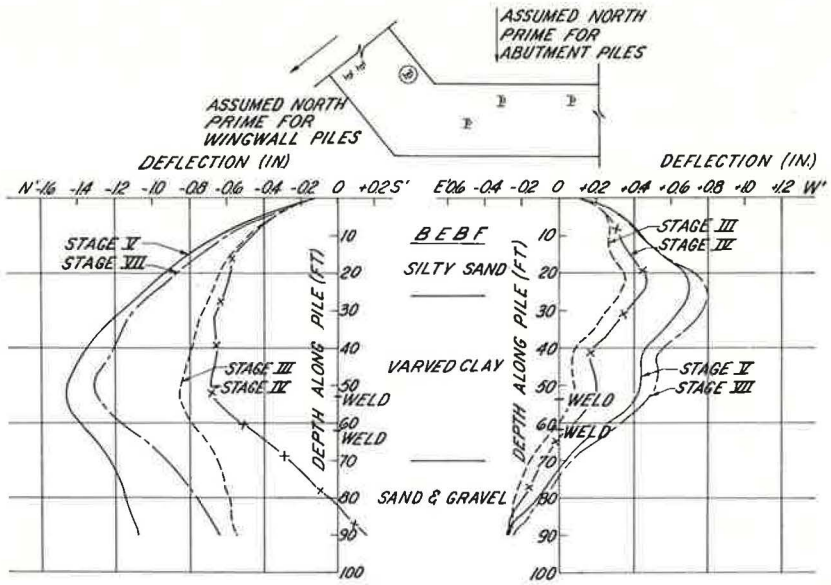

Figure 5. Deflections with time for vertical pile 13.

Increasing the embankment height to final subgrade in stage 7 resulted in further reductions in the K-value to 0.12 and 0.19 for the abutment and wing wall respectively. These latest reductions in K are quite small, probably because the varved clay consolidated under the weight of the embankment and abutment loads that remained relatively unchanged from November 1969 through April 1970 with a corresponding decrease in void ratio and increase in shear strength.

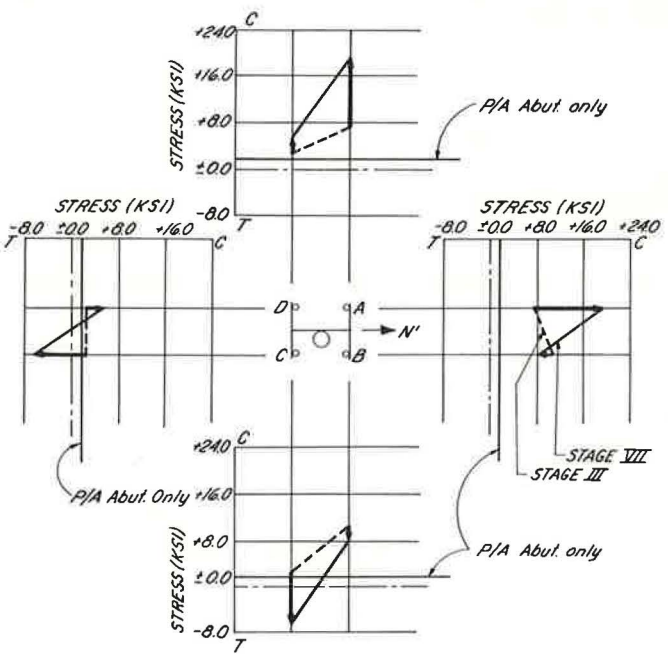

Figure 6. Bending stresses with time for vertical pile 13.

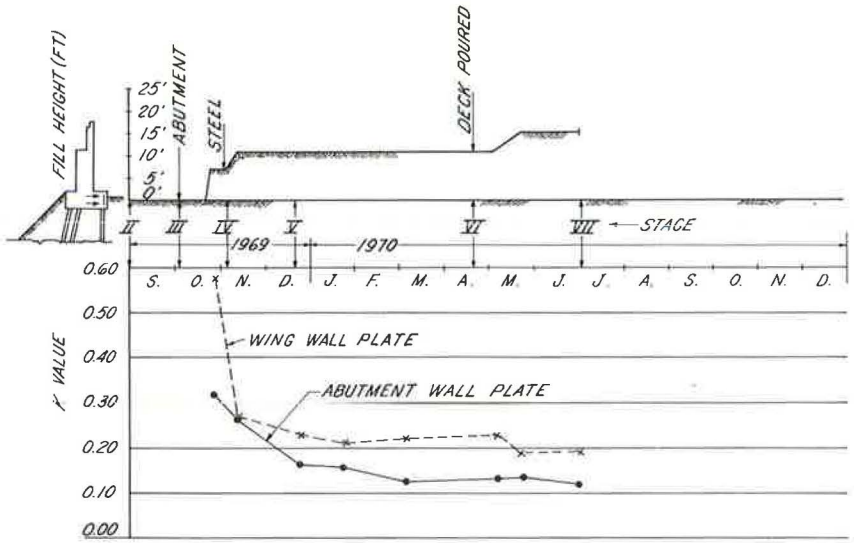

Figure 7. Coefficient of lateral earth pressure with time.

The settlement platforms behind the test abutment showed settlement of the original ground surface as indicated by the settlement curves shown in Figure 8. Several of the settlement platform pipes were accidentally disturbed, and this resulted in unreliable values for the total settlement although the trend of the settlement values remained valid.

Settlement readings on the top of the test abutment were much more conclusive. Plots of settlement for points 13 and 14 at the end of each wing wall at the test abutment, also shown in Figure 8, yielded curves corresponding to the settlement plots for the adjacent settlement platforms. Readings taken on the other abutments showed similar qualitative settlements.

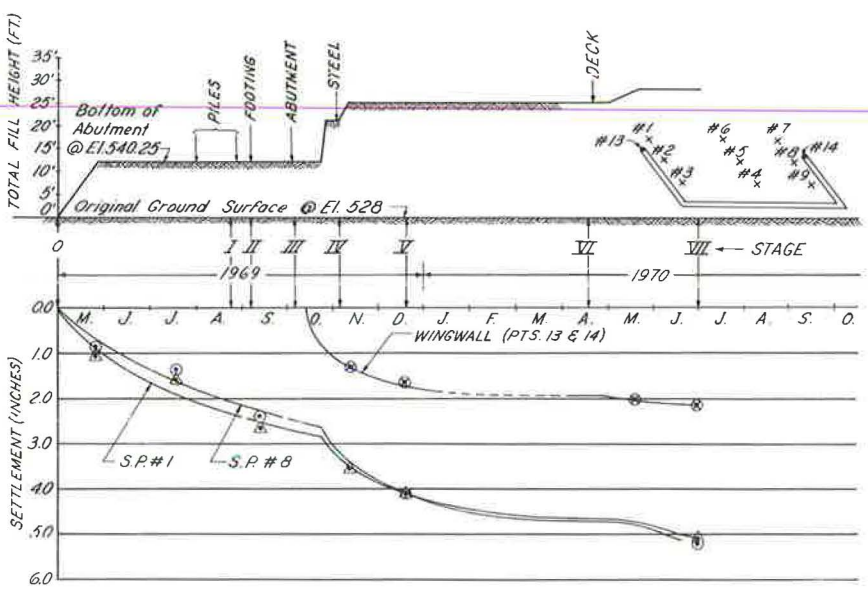

Figure 8. Settlements with time.

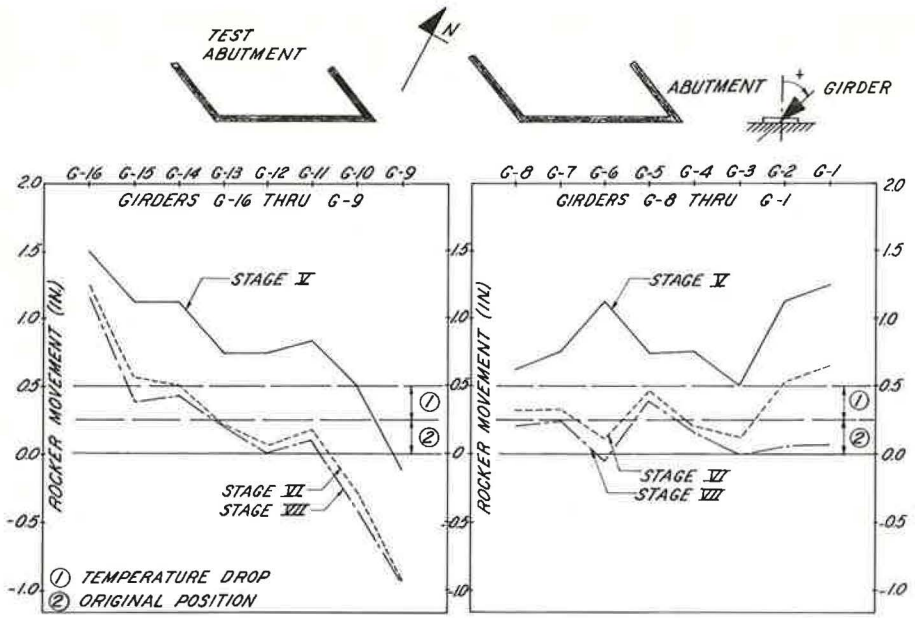

Figure 9. Rocker tilts with time.

Results of the triangulation between the abutments to determine the horizontal movement were disappointing. A small amount of tilting of the abutment back into the embankment was recorded before one of the reference line monuments used for these measurements was disturbed. Subsequently, 2 new reference lines were established with more monuments only to be destroyed by someone unfamiliar with the work.

Measurements of the expansion rockers of the west abutment at the Lehigh and Hudson Railroad are shown in Figure 9. Parts of the tilting shown is a result of contraction caused by thermal changes and the initial tilt of the rockers when set. The remainder of the tilting is attributed to movement of the abutments in both the eastbound and the westbound bridges. Because the abutments had fixed bearings, any movement at these abutments would be reflected as tilting at the expansion rockers of the west abutment. Examination of data shown in Figure 9 reveals that there was rotation of each abutment about a vertical axis. The portion of each abutment closer to the median, where there was an appreciable height of embankment, moved away from the embankment. The portion of each abutment closer to the outside embankment slope tilted back into the embankment. Movement at girder G16 (Fig. 10) at the test abutment was the maximum tilting observed.

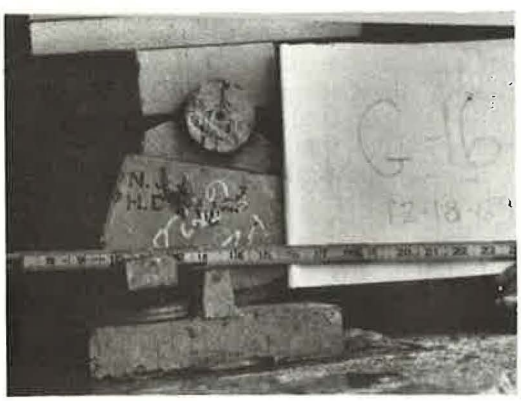

Figure 10. Rocker tilt at girder G16, December 1969.

DISCUSSION OF RESULTS

Results of Present Investigation

A decrease in lateral earth pressures against the abutment and wing wall was observed with a corresponding decrease in the lateral coefficient of earth pressure from 0.32 to 0.12 and 0.58 to 0.19 for the abutment and wing wall respectively. The decrease of these pressures was concurrent with the increase in settlement of the

backfill behind the abutment. In addition, this rotation of the abutment about a vertical axis caused the stress meters to move toward the embankment. If the abutment had not rotated in this manner, it is likely that a larger decrease in the coefficient of lateral earth pressure would have been observed.

The vertical H-piles under the heel of the abutment were subjected to bending stresses due to lateral pressures of the consolidating clay layer, the tilting of the abutment, and the rotation of the abutment about a vertical axis.

The dual effect of the decreased lateral pressure against the abutment and of the increased lateral pressure against the supporting piles could be visualized as a couple acting in a vertical plane, which induces a tilting of the abutment toward its backfill. This is confirmed by the excessive tilting of the rockers supporting the bridge girders and by the large relative settlements of the wing walls (Fig. 8 and 2, Figs. 27 and 28). The assumption is that the supporting piles at the end of the wing walls, which were not instrumented, have yielded, transferring their load to the wing-wall footings.

The beginning of the pronounced tilting of the abutment coincided in time with the construction stage when the shearing stresses within the underlying plastic clay layer, due to the weight of the backfill, started to induce localized plastic flow and deformation in the weaker zones of the clay. This apparently established a maximum limit value for the applied surface load equal to 3C (C = cohesion) to prevent backward tilting of similar abutments (2). Establishment of this upper limit is also supported by the fact that no excessive tilting of the rockers or of the abutments was detected at the adjoining bridge over Alphano Road where shearing stresses and shearing stress gradients in the underlying clay layer were smaller because of a lower, balanced, and more uniform height of embankment (2, Fig. 7).

A 5-month winter pause in the placing of the backfill behind the abutment induced a sufficient increase in the shearing strength of the clay due to its consolidation and accelerated by its varved nature so that no appreciable additional movements occurred when the filling was completed in the late spring of 1970. This emphasizes the practical importance of preloading as a design tool.

Recommendations for Future Investigations

The Carlson stress meter readings were found to be fully reliable. Provisions were made to facilitate readings of stresses due to lateral pressures on the abutment and wing wall after the project is opened to traffic. This would establish whether the decrease of the lateral pressures is permanent or will vary during the use of the bridge.

Readings on the Carlson strain meters, located at the top of the piles just below the pile caps, were reliable and consistent with the behavior of the abutment. For a more complete interpretation of the behavior of similar abutments in future investigations, strain-measuring devices should be installed along the pile length and stress-measuring devices should be installed at the lower surface of the pile cap.

Wilson inclinometers gave reasonable results that were in qualitative agreement with the strain meter readings on the H-piles. However, by comparison to the strain readings, the deflection readings were low, possibly because of the yielding and possible loss of the Ottawa sand filling the annular space between the inclinometer guide casing and the outer steel pipe. Use of miniature inclinometers and improved connections between the inclinometer casing and the pile are essential for future work.

Accurate triangulation of abutment displacements is also important in establishing the movement of the pile butts and, therefore, the true deflection curves.

CONCLUSIONS

The results obtained from these field measurements have established that abutments supported on piles driven through soft clay layers tilt toward the backfill when the shearing strength of these deposits is exceeded because of the superimposed embankment loads. An upper limit has apparently been established on the magnitude of the applied surface load (limit value of 3C) beyond which excessive abutment tilting will occur. The magnitude of the tilting has been found to be most sensitive to the shear strength of the deposit and loading rate and also dependent on the shear stress gradient and pile locations.

Preloading of soft foundation soils should always be considered, even for pile-supported abutments. The amount and time of surcharging will be governed by the consolidation and strength characteristics of the compressible layers.

Piles with adequate resistance to bending should be used to support abutments when compressible layers have not been previously stabilized. These piles should be of the nondisplacement type to minimize remolding of the clay and the resulting decrease of its shearing strength. Steel H-piles or pipe piles driven open-ended would meet this requirement.

Use of "spill through" types of abutments could be made in cases where the direction and magnitude of lateral forces acting against the abutment and wing walls are undetermined because of consolidation of the foundation soils.

ACKNOWLEDGMENT

The work presented in this paper was sponsored by the New Jersey Department of Transportation. The authors extend their sincere thanks and gratitude to Gregory P. Tschebotarioff for his constant guidance and support. Acknowledgment is also made to the personnel of King and Gavaris Consulting Engineers and to Anker Winther of the New Jersey Department of Transportation for their assistance throughout the course of this study. The contractor, S. J. Groves and Sons Company, and his superintendent, Robert McGilvra, must be complimented for their excellent cooperation and their ability to adapt to numerous field changes that became necessary during construction.

REFERENCES

1. Tschebotarioff, G. P. Chapter 5. In Retaining Structures in Foundation Engineering (Leonards, G. A., ed.), McGraw-Hill, New York, 1962.
2. Report to the New Jersey Department of Transportation: Movement Towards Its Backfill of Pile Supported Bridge Abutment. King and Gavaris Consulting Engineers, Aug. 1970.
3. Stermac, A. G., Derata, M., and Selby, K. G. Unusual Movements of Abutments Supported on End-Bearing Piles. Canadian Geotechnical Jour., Vol. 5, No. 2, May 1969.
4. Tschebotarioff, G. P. Bridge Abutments on Piles Driven Through Plastic Clay. Conf. on Design and Installation of Pile Foundations and Cellular Structures, Lehigh University, April 1970.
5. Hanna, T. H. Behavior of Long H-Section Piles During Driving and Under Load. Ontario Hydro Research Quarterly, First Quarter, 1966.
6. Bjerrum, L. Norwegian Experience With Steel Piles to Rock. Geotechnique, Vol. 7, 1957.

DISCUSSION

G. P. Tschebotarioff, Consulting Engineer, Lawrenceville, New Jersey

The authors are to be complimented for a very lucid presentation of a complex topic. Also, I would like to thank them for their gracious acknowledgement of my connection with this research project.

A precise determination of the actual lateral pressures against the piles under the abutment did not prove possible, but the order of dimension thereof seems to emerge fairly clearly and indicates to me the need for a downward revision of the values roughly "guesstimated" by me in 1962 (1, p. 492). No such measurements on piles had as yet been made then.

The purpose of this discussion is to indicate and to justify these revisions by the measurements reported in the paper.

In 1962 I had suggested assuming a triangular lateral loading of the pile along the depth of the clay layer with a maximum pressure p_H at the center of the layer.

$$p_H = 2bk\,(\gamma H) \tag{1}$$

where

b = width of pile;
(γH) = weight of fill behind abutment in respect to original ground; and
K = 0.4 = consolidated equilibrium lateral earth pressure coefficient.

The doubling of the width b in Eq. 1 was based on the results of model tests with sand (1, pp. 466 and 514). This does not now appear necessary in sensitive clays where some slight remolding is possible even around H-piles.

The results obtained at Allamuchy suggest the following changes to Eq. 1:

$$P_H = \beta bK\delta_z \tag{2}$$

where

β = stress concentration coefficient, taken as 1.00 for Allamuchy;
δ_z = vertical stress at point where p_H is determined;
b = width of pile; and
K = 0.4 = consolidated equilibrium lateral earth pressure coefficient.

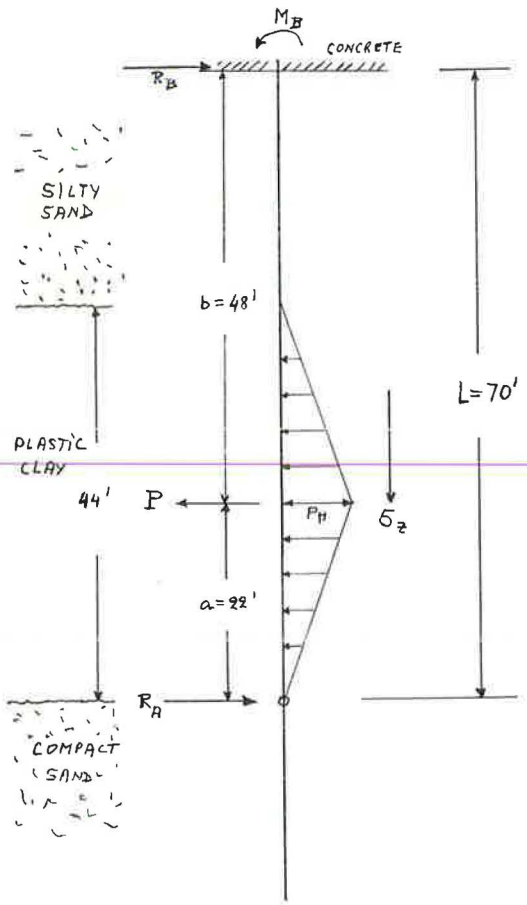

Figure 11. Dimensions for analysis of measurements at Allamuchy site.

Because at Allamuchy (γH) = 3.1 ksf and δ_z = 1.25 ksf, the use of Eq. 2 instead of Eq. 1 means an almost fivefold reduction in the numerical values of p_H.

Figure 11 shows the dimensions relevant to the following analysis of the Allamuchy measurements. If we replace the triangular loading by a concentrated force P and assume complete fixation of the pile in the concrete footing and a hinge at the upper surface of the compact sand layer under the clay, structural handbooks give the following values for the moment of fixation M_B at the upper support and for the field moment M_m:

$$M_B = -\frac{P\,a(L^2 - a^2)}{2\,L^2} \tag{3}$$

$$M_m = +(P\,a/2)(2 - 3a/L + a^3/L^3) \tag{4}$$

For the values, a = 22 ft and L = 70 ft shown in Figure 11, we obtain M_B = -9.35 P and M_m = +10.30 P = 1.16 M_B.

As stated in the paper, the bending moment of fixation for the vertical piles averaged 41 kip-ft. This value was computed from readings of Carlson strain meters, the centerline of which was 4.5 in. from the neutral axis of the 12-in. H-pile. The extreme fiber strain corresponding to the actual bending moment

would, therefore, be 6.0/4.5 = 1.33 times larger than the one recorded. Further, because the strain meters were located about 1.5 ft below the bottom of the footing, the bending moment of fixation would be at least 5 percent larger than the one at the location measured. This gives $M_B = 41 \times 1.33 \times 1.05 = -57.5$ kip-ft and $M_m = +57.5 \times 1.16 = +66.7$ kip-ft.

If we attempt to compute the bending moment M_m from the maximum 0.3-in. deflection along the 44-ft deep clay layer determined from inclinometer readings, we obtain a maximum value of $M_m = 12.1$ kip-ft, which is 4.75 times smaller than the average moment of fixation M_B of the pile at its upper end. This result cannot be reconciled at present with any logically conceivable pressure redistribution pattern, which would fit other data from this job, but may be attributed to some yielding at small deflections of the imperfectly compacted Ottawa sand that filled the space between the steel pipe welded to the H-pile and the aluminum guide casing for the inclinometers.

The following computations will, therefore, be based solely on the fixation moment $M_B = -57.5$ kip-ft determined from the Carlson strain meters because it cannot be too large and may even correspond to only partial fixation. The H-piles had only the customary 1.0-ft embedment in the 3,000-psi concrete of the footing. The compressive stresses in the concrete along the vertical faces of the H-pile flanges necessary to balance the bending moment $M_B = -57.5$ kip-ft will equal $f_c = 2{,}400$ psi at the edge or 80 percent of the 28-day compressive strength. Some yielding and plastic flow of the concrete may have, therefore, occurred.

We will use $M_B = -57.5$ kip-ft but, as a first approximation, compute from Eq. 3: $P = 57.5/9.35 = 6.15$ kips. Because an equivalent triangular load will produce a bending moment of fixation at least 10 percent smaller than the value obtained from Eq. 3 for a concentrated load, we find the ordinate p_H of the triangular load (Fig. 11) from $p_H = (6.15 \times 1.10 \times 2)/44 = 0.307$ kip = ft. Inserting this value, b= 1.0 and $\delta_z = 1.25$ ksf (2, Fig. 29) into Eq. 2 and solving for K, we obtain K = 0.245. In view of various uncertainties involved, it will nevertheless be prudent to continue using K = 0.40 in Eq. 2.

In this connection, one should note the evidence shown in Figure 8 that piles under the extreme tips of the wing walls started to buckle. An extreme fiber stress in bending of some 30,000 psi, when added to stresses produced by axial loading, should be sufficient to initiate buckling. The piles under the skewed wing walls project a width of 1.35 b on plane paralled to main abutment. If we distribute the lateral pressure on that width to the major and minor principal axes of a pile in proportion to their moments of inertia, we find that a value of K = 0.24 corresponds to an extreme corner stress of 38,000 psi and the triangular loading of Eq. 2. These piles at the ends of the wing walls are more exposed to possible stress concentrations than piles 13 and 9 on which measurements were made under the wing walls.

Of course, the possibility cannot be excluded that further measurements and studies may reveal a much more complex and hitherto unsuspected pattern of pile-soil interaction.

A. A. Seymour-Jones, Howard, Needles, Tammen and Bergendoff

The authors are to be complimented for having presented some very interesting information on a neglected subject. It is hoped that this paper will generate further studies of this problem because it can and has occurred in many areas where compressible foundation soils exist.

The writer agrees with the authors that the best prevention for this type of problem is preloading or surcharging the abutment areas. However, there have been cases where schedules or other factors do not permit adequate treatment of the foundation areas, so the engineer has to face this type of condition.

The writer has encountered 7 cases of similar abutment movements and obtained rough measurements of the movements involved. These data have provided a basis for evaluating similar problems and are given in Table 1.

The data given in Table 1 provide a basis for estimating possible abutment rotation for similar problems provided a reasonable estimate of the post construction settlement

TABLE 1

SUMMARY OF ABUTMENT MOVEMENTS

Structure	Foundation	Fill Settlement (in.)	Abutment Settlement (in.)	Abutment Tilting (in.)	Ratio of Abutment Tilting to Fill Settlement
1	Steel H-piles	16	Unknown	3	0.19
2	Steel H-piles	30	0	3	0.10
3	Soil bridge	24	24	4	0.17
4	Cast-in-place piles	12	3.5	2.5	0.19
5	Soil bridge	12	12	3	0.25
6	Steel H-piles	48	0	2	0.06
7	Steel H-piles	30	0	10	0.33
—[a]	Steel H-piles	5	0.4	0.5 to 1.5	0.10 to 0.30

[a]Described in paper.

magnitude can be made. Based on these data, the writer would recommend a ratio range between 0.25 and 0.33.

Problems associated with abutment tilting can be provided for by the following steps:

1. Instead of rockers, use sliding plate expansion shoes with sliding plates large enough to sustain the anticipated horizontal movements;
2. Make provisions to fill in the bridge deck expansion joint over the abutment by inserting either metal plate fillers or larger neoprene joint fillers;
3. Design piles for drag forces due to settlement; and
4. Use steel H-piles for the abutment foundation.

Unfortunately there is insufficient information to calculate the bending forces induced in the piles by the abutment rotation at this time. It is hoped that further research will provide a guide in the future. Because all the abutments (Table 1) founded on piles are performing satisfactorily, bend stresses in the piles may not be a major problem. Still it would be prudent to use steel H-piles in such cases because they are capable of taking large tensile stresses without failing.

The writer has had access to the report (2) referred to by the authors. Two facts noted are of interest. The driven piles deviated appreciably from a straight line. The measured stresses in the 6 instrumented piles varied considerably from the design stresses. It is the writer's conclusion that for these 2 reasons conservative design-allowable pile loads should be used for structures of this type.